UNIVERSITY OF ALBERTA

STRUCTURED SPLINES M0DELS: THEORY AND APPLICATION TO THE CLINICAL MANAGEMENT OF TORSO DEFORMITIES

by

PETER OKECHUKWU AJEMBA 

A thesis submitted to the Faculty of Graduate Studies and Research in partial fulfillment of the requirements of for the degree of DOCTOR OF PHILOSOPHY

DEPARTMENT OF ELECTRICAL AND COMPUTER ENGINEERING

EDMONTON, ALBERTA

FALL, 2007

Your file Votre référence
ISBN: 978-0-494-32908-5
Our file Notre référence
ISBN: 978-0-494-32908-5

Anything that would not sell, I do not want to invent.

Its sale is proof of its utility.

And its utility is proof of its success.

Thomas Alva Edison

(February 11, 1847 – October 18, 1931)

ABSTRACT

This thesis describes the research and development of a novel method for analyzing, quantifying and tracking the shape of three dimensional objects based on their curvature and symmetry. The method is called structured splines modelling and it brings together and expands on ideas from mathematical shape analysis, computer engineering and biomedical image analysis.

Shape description using structured splines models has the following properties: it is intuitive, based on features of an object that are most relevant to its visual perception; it is relatable, yields indices that can be understood in terms of the common description of shape such as bend, twist and tilt; it is practical, accepts range images of objects, a form of input that is available from most segmentation or image acquisition applications; and it is error-correcting, corrects such errors in the input data as holes and stray points. Structured splines modelling is the first shape analysis method to possess all of these properties.

We present the theory of the structured splines model and describe its application to quantifying and tracking torso deformity caused by scoliosis, a deformity of the spine that causes visible torso asymmetries. The application to scoliosis provides clinicians with information on the shape of the torso in an intuitive and useful form, thus aiding in deformity management. The application represents the first use of a shape-based index of asymmetry in the biomedical image analysis of torso deformity.

DEDICATION

To my Mum and Dad, Anne and Donatus Ajemba,

for your love and sacrifice.

ACKNOWLEDGMENTS

I would like to thank my supervisors, Dr. Nelson G. Durdle and Mr. V. James Raso, for their patience, guidance and support in the course of completing my PhD research work and thesis.

I would like to thank Doug Hill of the Rehabilitation Technology Department, for his technical support of the experiments I carried out at the Glenrose Rehabilitation Hospital, Edmonton, Alberta, Canada. I am grateful to Dr. Marc Moreau and Dr. James Mahood for supporting my recruitment and use of volunteers from their patient pools, and for the use of their clinic time to facilitate data collection. I would like to thank the many generations of summer students at the Rehabilitation Technology Department of the Glenrose Rehabilitation Hospital, whom I called on over the years to support my experiments as volunteers or technical hands.

I would like to thank the Alberta Informatics Centre for Research Excellence (iCORE), the Alberta Ingenuity, and the Canadian Institute of Health Research (CIHR) Bone and Joint Training Program for their very generous financial support over the years. I would also like to thank the Faculty of Graduate Studies and Research for awarding me the Andrew Stewart Memorial Prize for Excellence in Doctoral Research and other awards. My many sources of financial support made my PhD work much easier.

I would like to thank my siblings: Paul, Justina, Jane-Frances, Chukwudi, Linda and Michael, for their support and prayers. I am grateful to Nana Ofosua and my many friends for their support and help during the course of my PhD work.

TABLE OF CONTENTS

Appendix 2: Effect of posture and re-positioning on scoliosis imaging

Appendix 3: Additional background materials

LIST OF TABLES

LIST OF FIGURES

CHAPTER 1

INTRODUCTION

1.1 PURPOSE

This thesis describes the research and development of a method for analyzing, quantifying and tracking the shape of three dimensional (3-D) objects based on their curvature and symmetry. The method is called structured splines modelling and it brings together and expands on ideas from mathematical shape analysis, computer engineering and biomedical image analysis. Shape description using structured splines models has the following properties: 1) intuitiveness – it is based on features of an object that are most relevant to its visual perception; 2) relatability - it yields indices that can be understood in terms of the common description of shape such as bend, twist and tilt; 3) practicality – it accepts range images of objects, a form of input that is available from most segmentation or image acquisition applications; 4) error-correction – it corrects such errors in the input data as holes and stray points.

This thesis presents the theory of structured splines models and describes its application to quantifying and tracking torso deformity caused by scoliosis (see Section 2.3 for a description of scoliosis). The application to scoliosis provides clinicians with information on the shape of the torso in an intuitive and useful form, thus aiding in deformity management.

1.2 MOTIVATION

The management of scoliosis is traditionally based on the assessment of the internal deformity of the spine [1], [2]. Recently, there has been a move towards incorporating information about the shape of the torso in the routine care and management of scoliosis patients [3]. This is borne of the fact that most scoliosis

patients and their families are more concerned with the shape of the torso than the internal alignment of the spine and judge protocols for managing scoliosis based on their effect on torso shape [4], [5]. Also, patients typically visit scoliosis clinics for the first time because they are worried about their appearance [6]. From the clinician's point of view, change in torso shape may indicate changes in the spinal alignment.

Traditional methods for assessing torso shape are based on landmarks. As the torso is relatively smooth, it is difficult to precisely locate these landmarks in real time. Also, the large anthropometric variation in the population means that the relative locations of torso landmarks vary significantly amongst patients[1]. Finally, landmarks are particularly prone to the effects of posture variations, sway and breathing that usually occur during the acquisition of torso images. These effects are a function of being alive and cannot be completely eliminated. For instance, a slight lift of one shoulder would significantly change the locations of landmarks on the offending shoulder relative to other landmarks.

Other techniques such as *difference mapping* [7], for evaluating changes in torso shape by subtracting consecutive range images, have been proposed. However, *difference maps* have not fully matured as it is very difficult to precisely fit two surface maps of the back while coping with other sources of change such as growth, posture, sway and breathing.

These difficulties call for the use of shape analysis methods for characterizing and describing torso shape changes caused by scoliosis. However, to be useful, the method chosen needs to be intuitive so that it can be meaningful to the clinicians involved in the chain of care of scoliosis patients. It also needs to be practical so that it can be easily implemented and descriptive so that its output can better inform

[1] For a description of the anthropometric variation in children, see for instance, R. G. Synder *et al.*, *Anthropometry of infants, children, and youths to age 18 for product safety design SP-450*, Society for Automotive Engineers, Inc., Warrendale, PA, USA. 1977.

clinical decision making and be easy to explain to patients and their families. A survey of the literature shows that existing shape analysis methods do not possess one or more of these requirements. Thus, there is a need to develop a new method for assessing, quantifying and tracking three-dimensional (3-D) shape that would then serve as the framework for incorporating shape analysis in the assessment of torso deformity and the clinical management of scoliosis.

1.3 RESEARCH FRAMEWORK

A review of the literature (Chapter 2) highlights the gaps that exist in the knowledge related to our application. First, there is a need to develop a shape analysis method that satisfies the four criteria given in Section 1.1, that is: intuitiveness, practicality, relatability and error-correction. Of existing shape analysis methods, dominant point-based techniques (Section 2.2) are most promising as they are intuitive and practical but still need to be improved so that they can become relatable and error-correcting. Second, there is a need for shape-based analysis of torso shape. Existing methods for assessing torso shape are based on landmarks and suffer greatly from anthropometric variations in the population [8] and from variations in individuals [9] caused by growth and positioning during torso image acquisition. This thesis fills these two gaps.

First, an imaging system is developed for use in the acquisition (Chapter 7) and pre-processing (Chapter 8) of the torso topographic images of scoliosis and non-scoliosis patients. These images are used for model development and clinical validation. Second, three shape analysis methods are developed. The first is based on computing the *orthogonal maps* of the torso by performing a cylindrical to Cartesian coordinate transformation (Chapter 5). The second involves calculating points of high curvature on an object's surface (Chapter 6). The third derives the structured splines models of objects and is the most sophisticated and robust of the

three (Chapter 3). Third, three sets of deformation indices corresponding to each of the shape analysis methods described above are developed (Chapter 4). The shape analysis method and corresponding deformation indices are applied to the shape-based assessment of torso deformity in scoliosis. Finally, the overall system is evaluated using the developed curvature-based shape analysis method (Chapter 9).

1.4 OBJECTIVES AND SCOPE

The objectives of this thesis are two-fold.

1) To create a novel method for describing and assessing 3-D shape that is intuitive, descriptive and practical. This requires making use of mathematical features of objects that greatly influence the human perception of shape. The method should be applicable to the task of describing and assessing the torso deformity caused by scoliosis.

2) To create a tool for quantifying and tracking shape changes in 3-D objects. This requires developing a multi-dimensional shape score that is robust and intuitive. In addition, the shape score should be applicable to the quantification and tracking of the torso deformity caused by scoliosis. It should be translatable to the common description of torso deformity.

The scope of this thesis is limited to developing a curvature-based method for assessing shape in 3-D, developing a deformation index for quantifying shape and shape changes in 3-D objects and demonstrating the quantification and tracking of the torso deformity caused by scoliosis using the developed deformation index.

1.5 THESIS OUTLINE

Structured splines models are tools for assessing and describing 3-D shape. Their outputs can be processed to obtain a set of indices for quantifying and tracking

shape changes. This thesis presents the theory of structured-splines-modelling and demonstrates its application to managing scoliosis using range images of the torso.

Chapter 2 presents a review of the literature. Overviews of shape analysis and description, dominant points, scoliosis and range imaging systems are presented. Shape analysis techniques can be grouped into feature-based and content-based methods. Dominant points are a sub-set of feature-based methods that possess two of the four qualities we require for our application (See Section 1.1). Section 2.3 describes scoliosis and the torso deformity that results from it. The internal deformity caused by scoliosis is assessed using radiographs while its external deformity is assessed using range images of the torso. Section 2.4 describes range imaging systems and describes an example system.

The rest of the thesis can be divided into four parts: 1) the theory and validation of the structured splines model (Chapter 3) and application to quantifying torso deformity in scoliosis (Chapter 4); 2) *orthogonal maps* (Chapter 5) and *point-set data* (Chapter 6), two pertinent tools for shape analysis; 3) the torso analysis system comprised of image acquisition (Chapter 7) and pre-processing (Chapter 8); and 4) an evaluation of the entire system comprised of shape acquisition, pre-processing and modelling (Chapter 9).

Chapter 3 presents the theoretical framework of the structured splines models. The relationship between the Gaussian and *B*-spline scale spaces is described. As Gaussian scale-spaces have been used for multi-scale analysis of contours, their relationship to *B*-spline scale spaces makes the use of *B*-spline basis functions in multi-scale analysis of shape possible. This chapter marks the completion of our model development and index formulation.

Chapter 4 describes the application of structured splines models and their corresponding indices of torso deformity to quantifying and tracking torso shape in scoliosis. The chapter also presents the first shape-based classification system for

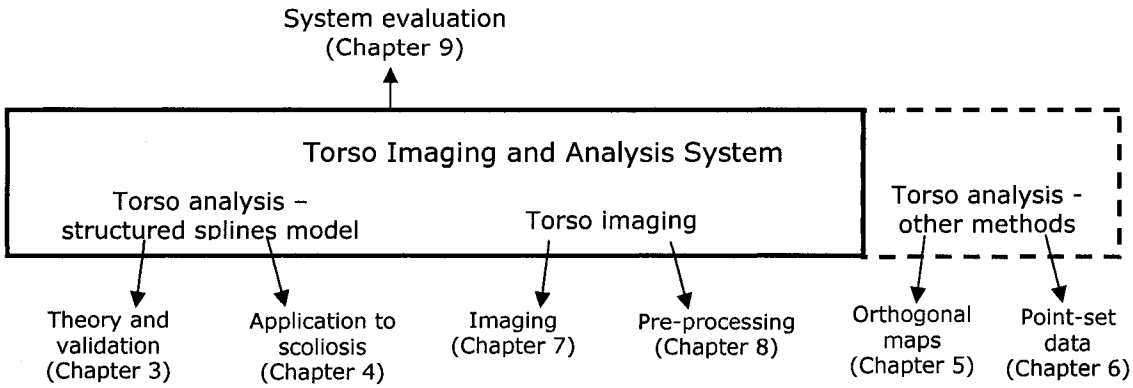

Fig. 1.1: An illustration of the relationship between the chapters.

torso deformity. A comparison between the developed shape-based indices and other clinical indices with regards to classifying scoliosis is performed.

Chapter 5 presents *orthogonal maps*, an alternative tool for shape analysis obtained by performing a cylindrical to Cartesian coordinate transformation of torso images. Chapter 6 presents *point-set data*, another tool for shape analysis that is derived from points of high curvature on an object's surface.

Chapter 7 describes our torso image acquisition system. Chapter 8 describes routines for transforming range images of the torso into a form suitable for use in a shape analysis application. The routines are used to fill holes, remove stray points and crop unwanted regions.

Chapter 9 presents the results of evaluating the entire system comprised of: 1) torso imaging; 2) pre-processing and reconstruction routines; and 3) structured splines models. The system response to errors due to sway and breathing is assessed. The variability of the shape-based and landmark-based indices of torso deformity and the reconstruction accuracy of the system are investigated. A justification for using full torso images rather than back torso images in the clinical monitoring of scoliosis is provided.

Chapter 10 presents conclusions and suggestions for future work.

REFERENCES

1. V. J. Raso, *et al.*, 'Trunk distortion in adolescent idiopathic scoliosis,' *Journal of Pediatric Orthopedics*, vol. 18, no. 2, pp 222-226, 1998.
2. J. R. Cobb, Outline for the study of scoliosis, instructional course lectures, The American academy of orthopedic surgeons 5, pp 261-275, 1948.
3. R. Levy, M. S. Goldberg, N. E. Mayo, J. A. Hanley and B. Poitras, 'Reducing the lifetime risk of cancer from spinal radiographs among people with adolescent idiopathic scoliosis,' *Spine*, vol. 21, pp 1540-1548, 1996.
4. I. A. F. Stokes, M. S. Moreland, 'Concordance of back surface asymmetry and spine shape in idiopathic scoliosis,' *Spine*, vol. 14, pp. 73-78, 1989.
5. T. N. Theologis, R. J. Jefferson, A. H. Simpson, A. R. Turner-Smith, and J. C. T. Fairbank, Quantifying the cosmetic defect of adolescent idiopathic scoliosis, Spine, 18, pp. 909–912, 1995.
6. R. A. Dickson, 'Spinal Deformity - Adolescent Idiopathic Scoliosis: Nonoperative Treatment,' *Spine*, vol. 24, no. 24, pp 2601-2606, 1999.
7. D. C. Berg, D. L. Hill, V. J. Raso, E. Lou, T. Church, M. J. Moreau, J. K. Mahood, 'Using three dimensional difference maps to assess changes in scoliotic deformities,' *Medical and Biological Engineering and Computing*, vol. 40, no. 3, May 2002.
8. P. O. Ajemba, N. G. Durdle, D. L. Hill, and V. J. Raso, 'Accuracy assessment of a complete human torso topographic analysis system for assessing trunk deformities,' To appear in *Computers in Biology and Medicine*, 2007.
9. P. O. Ajemba, N. G. Durdle, D. L. Hill, and V. J. Raso, 'Classifying torso deformity in scoliosis using orthogonal maps of the torso,' *Medical and Biological Engineering and Computing*, vol. 45, pp. 575-584, June 2007.

CHAPTER 2

LITERATURE REVIEW

2.1 SHAPE ANALYSIS AND DESCRIPTION

Shape description spans many fields. To mathematicians, a shape is typically an equivalence class under a group of transformations. In the context of visual analysis of shape required for our application, this definition is necessarily incomplete as it only tells us when two shapes are exactly the same. We need to be able to differentiate between degrees of similarity. From the point of view of statistics [1] [2], the definition of shape incorporates a definition of shape distance. However, there is usually an assumption that the correspondence between similar parts of the shapes being compared is known, but this is not often the case. Other approaches from statistics do not require that there be a correspondence between parts of objects being compared. For example, one could compare feature vectors containing descriptors such as areas, volumes or moments and discard shape information in the process. An example of a study of shape similarity in psychology is Goldmeier [3].

An extensive survey on shape matching in pattern recognition can be found in [4]. In general, there are two broad approaches to shape analysis: 1) feature-based methods, which use the spatial arrangements of extracted features such as edge elements or junctions in 2-D and surfaces in 3-D; and 2) content-based methods, which make more direct use of pixel brightness or the colour of the interior in 2-D and voxel brightness or colour in 3-D.

2.1.1 Feature-based methods

The simplest feature of a 2-D object is its silhouette while that of a 3-D object is its bounding surface. A lot of work has been done using boundaries of *silhouette*

images. As silhouettes do not have holes or internal markings, their boundaries can be conveniently represented by a single-closed curve which can be parameterized by its arclength. Pioneering work on the analysis of silhouettes include Fourier descriptors, for example by Zahn and Roskies [5]. The publication of Blum's medial axis transform led to attempts to capture the part structure of the shape in the graph structure of the skeleton [6]. The 1-D nature of silhouette curves led to dynamic programming approaches for shape analysis, for example using the *edit distance* between the curves [7]. The best approaches from a comprehensive comparison of different shape descriptors for silhouettes, done as part of the MPEG-7 standard activity, were those of Latecki *et al.* [8] and Mokhtarian *et al.* [9].

Silhouettes are 2-D objects which extend to surfaces in 3-D. However, they are limited descriptors of general 2-D objects as they ignore internal contours which could be very important (for example in logos). They are also difficult to extract from real images. Approaches that treat shape as a set of points in the 2-D image make use of both outlines and internal edges. These are more promising and easier to use as the extraction of general edge points can be achieved using a simple edge detector. Huttenlocher *et al.* developed methods in this category based on the Hausdorff distance [10] that can be extended to deal with partial matching and clutter. Methods based on Distance Transforms, such as [11] are similar in spirit and behavior in practice.

The work of Sclaroff and Pentland [12] is representative of the eigenvector- or modal-matching based approaches. In these approaches, points in the image are cast into a finite element spring-mass model and correspondences are found by comparing their modes of vibration. Another example is Chui and Rangarajan [13]

There have been several approaches to shape recognition based on spatial configurations of a small number of key points or landmarks. In geometric hashing [14], these configurations are used to vote for a model without directly solving for

correspondences. Amit *et al.* [15] train decision trees for recognition by learning discriminative spatial configurations of key points. Leung *et al.* [16], Schmid and Mohr [17], and Lowe [18] additionally use gray-level information at the key points to provide greater discrimination power. But not all objects have distinguishing key points (e.g. the circle), and using key points alone sacrifices the shape information available in smooth portions of object contours.

A class of point-based techniques obtains rich local descriptors of a representative sample of points that make up the interior and exterior edges of the image. Prominent examples include the shape context [19] and distance multiset [20]. The use of rich local descriptors that are globally distributed about the shape has been shown to be very effective, even for applications where the image is partially occluded or sparsely sampled [21]. A major challenge in using rich local descriptors of global shape is developing effective sampling strategies to maximize the information content of the sampled set with regards to the overall shape.

It should be noted that though most of these methods were developed for 2-D applications, they can be easily extended to 3-D (particularly the silhouette based approaches) by decomposing the 3-D object into a number of cross-sections. This is the approach we take in developing our model for 3-D shape analysis.

2.1.2 Content-based methods

Content-based (also called brightness or appearance-based) methods make direct use of the color values within the content of the pixels of an image in 2-D or its voxels in 3-D rather than just the information contained in the interior or exterior edges or the shape of the containing contour. There are two frameworks for the use of content-based methods. The first framework directly performs correspondence and alignment using the color information. An example of this approach is Yuille [22]. In [22], invariance to a number of transformations can be in-built in the model

used to assess the similarity of the shapes being compared. Handicaps of the method include the need for human-designed templates and sensitivity to initialization when searching with gradient descent. Another example of a direct use of color values is Lades *et al.*'s elastic graph matching technique [23]. Some approaches first attempt to warp one image into another using dense correspondence field before they compare the color values. Examples of this approach include [24] and [25].

The second framework involves attempting the classification of shape properties without first solving for correspondences. In this framework, a learning algorithm is developed with enough examples to determine the appropriate invariances. Good examples in the area of face recognition include using principal component analysis [26], [27] particularly in a probabilistic framework [28]. Examples of the application of discriminative classification methods in the content-based shape matching framework include the LeNet classifier [29], and the support vector based methods of [30].

2.1.3 Pertinent gaps in knowledge

Though a plethora of methods have been developed over the years, there is a dearth of methods that are: 1) intuitive – based on features of an object that are most relevant to its visual perception; 2) relatable - yield indices that can be understood in terms of the common description of shape such as bend, twist and tilt; 3) practical – accepts range images of objects, a form of input that is available from most segmentation or image acquisition applications; and 4) error-correcting – corrects such errors in the input data as holes and stray points.

2.2 DOMINANT POINTS

Dominant point detection methods are a subset of feature-based shape analysis methods. They are primarily 2-D and make use of silhouettes. They were inspired by

Attneave's observation that much of the information about the shape of a curve is concentrated at points of local maximal curvature [31] called its dominant points. In Euclidean space, the curvature of a continuous curve is defined as the rate of change of its slope with respect to its arc length. This cannot be applied to digital curves as digital curves lack an exact mathematical definition [32]. In general, there are two approaches to computing dominant points from digital data. The first is to directly estimate the curvature of the points of interest by utilizing information from nearest neighbors to the point referred to as the point's *region of support*. The second approach is to obtain a piecewise linear polygonal approximation of the curve subject to constraints on the goodness of fit, such that the dominant points would correspond to the vertices of the bounding polygon [33]. This approach is considered the dual notion of the first [34], thus we focus on the first approach.

Detection of dominant points on a digital curve by curvature usually follows two stages: 1) estimation of the curvature of each point; and 2) selection of the points with maximal local curvature as the dominant points. Curvature estimation can be achieved by determining a region of support and calculating the curvature based on some established formula. The region of support delimits a point's neighborhood and is usually symmetric about the point. Sequential [35], [36], [37] and recursive [34] one point at a time schemes have been used.

Teh and Chin [32] posited that precisely determining the region of support was more important than choosing the curvature estimation formula. They proposed a nonparametric method that determines the region of support from the perpendicular distance between a point and a succession of chords obtained from other points centered on the point of interest. Several curvature measures have been used to estimate the curvature of each point, such as *k-cosine*, *k-curvature*, and *1-curvature* [37]. The selection of the points with maximal local curvature is then a simple matter

of ranking the points according to their curvature and optimizing the number of points chosen and the reconstruction error obtained from them.

Some region of support methods operate by pre-processing the Freeman chain codes of the curve. Cronin [38] proposed a method based on concavity code constructed from the chain codes. Arrebola *et al.* [39] calculated curvature by comparing histograms of chain codes. Sanchiz *et al.* [40] used neural networks to detect dominant points from chain codes. Other machine learning based methods have included the use of fuzzy knowledge and an adaptive method for segmenting free-hand sketches [41] and corner detection in binary images using neural networks [42]. Lin *et al.* [43] proposed a multi-scale shape recognition method based on feature vectors consisting of multi-scale wavelets applied to a *Hopfield network*. Here, wavelet normalization was applied to make the method scale invariant and to reduce distortion resulting from normalizing the object contours.

In many implementations, it is crucial to optimize the number of dominant points and the resulting approximation error. Liatsis *et al.* [44] proposed methods that simultaneously achieved this based on genetic algorithms (GA). Other GA methods include Yin's [45] methods for determining the optimal polygons of a digital curve and Tsang's [46] method for searching for the best alignment between contours of near planar objects. Scale-space methods have been used for computing the dominant points of continuous curves. An early example is Mokhtarian and Mackworth's [47] curvature based shape representation scheme. Other methods include Yin's [48] ant colony search algorithms, Fayolle *et al.*'s [49] wavelet methods for grey level images and Wang *et al.*'s [50] *B*-spline wavelet based multi-scale curvature functions. The method we describe in this thesis makes use of the scale-space property of *B*-spline curves.

The theory of dominant points has inspired several applications. Boucheham *et al.* applied dominant point detection methods to ECG reconstruction and baseline error

correction [51]. Lin *et al.* [52] developed an automatic palm-print verification system that employs multi-resolution hierarchical decomposition. Park and Lee [53] applied dominant points to *B*-spline curve fitting and Ganguly [54] showed that the simple Arc tree and Equal error tree was improved by finding tree vertices at only dominant points. Gao [55] proposed an efficient method for Hausdorff distance-based face matching using dominant points and Fatemizadeh *et al.* [56] applied dominant points to automatic landmark extraction from Magnetic Resonance brain images.

Other applications have included robot automation [57], segmentation of free-hand sketches and detection of principal features of handwritten characters [58], detection of edges and junctions [59], analysis of chromosomes [60], and the detection of stroke of Chinese characters [61] and edges [62].

2.2.3 Pertinent gaps in knowledge

As they are based on curvature and can be applied to range images, dominant point-based methods satisfy two of the four desired attributes (Section 2.1.3): intuitiveness and practicality. There is a need to modify the computation of dominant points so that the output is error correcting and relatable. We propose a method for achieving this in Chapter 3.

2.3 SCOLIOSIS

2.3.1 What is scoliosis?

Scoliosis is the abnormal lateral curvature of the spine accompanied by rotation of individual vertebrae and visible torso asymmetries [63]. The rotation of the vertebrae causes the ribcage to distort and a hump to be produced in the back of the torso. Radiological assessment of the lateral curvature of scoliosis usually includes measurement of the Cobb angle [64] (Fig. 2.1) which is the angle subtended by the

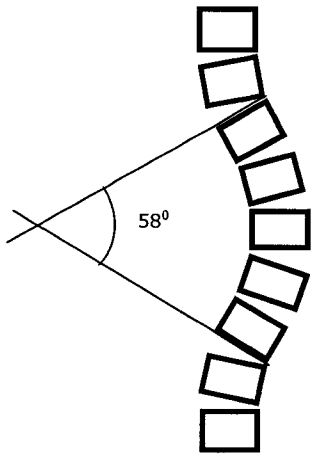

Fig. 2.1: The Cobb angle measurement of spinal deformity.

two normal lines to the points of maximum curvature in the spinal midline. Two to four percent of the population of North America has scoliosis of at least 10 degree Cobb angle [65]. Most of the people with significant curvature are girls [66] and most scoliosis develops during the adolescent years [67]. Some of the visible characteristics of scoliosis are: 1) uneven shoulder heights; 2) uneven scapula (shoulder blade) shape and prominence; 3) shifting of the trunk over the pelvis; 4) uneven hip shape and prominence; and 5) the head being off center over the pelvis. In addition, when the patient is examined from behind and asked to bend forward until the spine is horizontal, one side of the back usually appears higher than the other side (Fig. 2.2).

Despite more than a century of research, most cases of scoliosis are still of unknown etiology and termed *idiopathic* [63]. Consequently, there are no generally acceptable preventive measures for scoliosis. In adolescents, scoliosis can progress at an alarming rate and have severe effects on the cosmetic appearance of an individual [67]. In rare cases of severe scoliosis, organ development and pulmonary function can be affected [66]. However, many cases of late onset idiopathic scoliosis will have no attendant health risks associated with them [68].

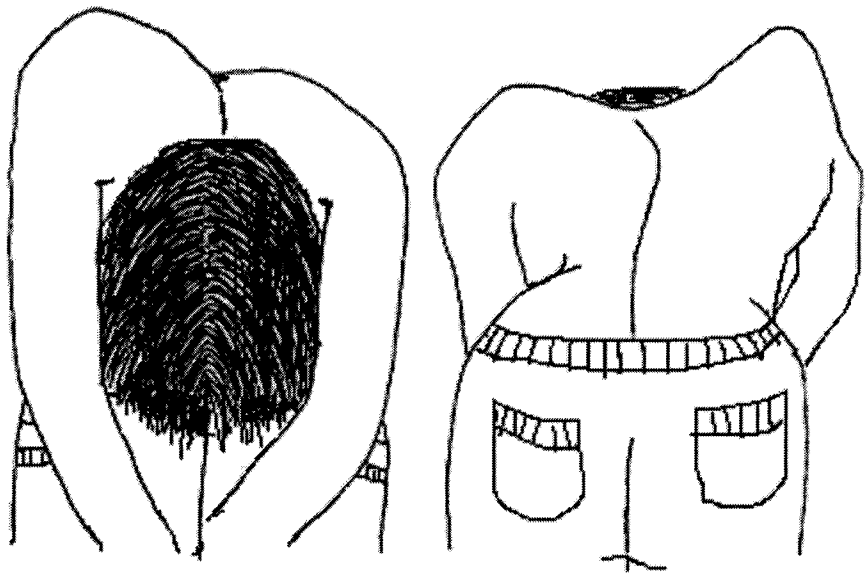

Fig. 2.2: Uneven shape of the back caused by scoliosis.

Scoliosis treatment is mostly influenced by the extent of the spinal curvature [69]. The general protocol is based on the Cobb angle [66]: 1) Small spinal curvatures (less than 20^0) require no treatment; 2) Medium spinal curvatures (between 20 and 50^0) are often braced (Fig. 2.3); and 3) Large spinal curvatures (more than 50^0) often require spinal fusion surgery (Fig. 2.4). Aside from improving the overall internal alignment of the trunk, two primary goals of treatment are to improve the external appearance of the torso and to halt the progression of the deformity.

2.3.2 Scoliosis monitoring

Scoliosis is traditionally monitored using posterior-anterior (back-to-front) and lateral (side) radiographs taken in the upright position. The rapid progression of scoliosis in many patients during the adolescent growth spurt prompted scoliosis clinics to start the frequent monitoring of patients. This raised fears about the cumulative effect of ionisation due to the increased frequency of radiography. Some authors attempted to link the increased use of radiographs to an increased risk of cancer [2]. Scoliosis

Fig. 2.3: The Boston brace used to manage moderate scoliosis.

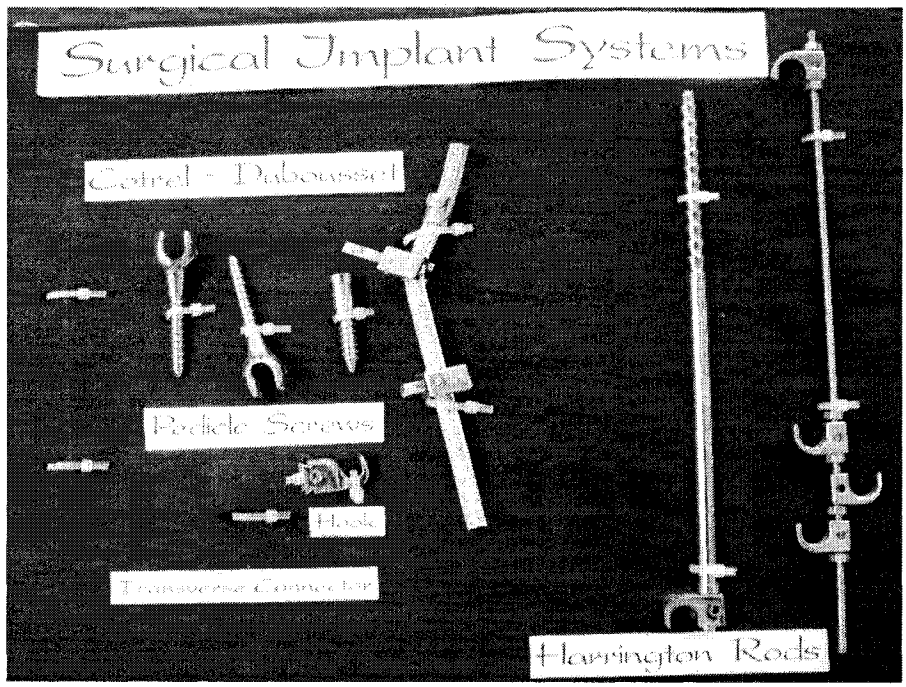

Fig. 2.4: Spinal fusion surgery often involves supporting the spine using metal rods and hooks.

clinics adopted minimal dose radiography to minimize this perceived risk of ionization. They also decreased their use of radiographs to about twice a year [70]. However, some clinicians believed that the decreased rate was inadequate to

monitor the rapidly evolving shape of the spine. This led to an increased effort to find alternative methods for assessing the internal and external effects of scoliosis and an increased interest in torso imaging systems and torso shape monitoring.

2.3.3 Use of torso surface images in scoliosis clinics

The management of scoliosis by torso shape predates radiography [71]. The use of plaster casts and torso models was the norm in the late nineteenth century [72]. The contemporary use of torso shape analysis was initially aimed at complementing radiographs, but accelerated due to fears of the ionization effects of radiation and the desire to develop methods for estimating spinal deformity from torso shape.

Over the years, several imaging techniques have been proposed for assessing scoliosis and monitoring its progression. Early techniques were limited to the back. These include: Moiré topography [73], Integrated Shape Imaging System (ISIS) scanning [74], Quantec system scanning [75], rasterstereography [74], [76], and laser scanning [77]. Indications that full torso images provide more information about the overall deformity of the torso than back torso images [78] prompted the development of several full torso imaging systems. These include Inspeck 3D digitizers (Inspeck Corporation, Montreal, Quebec, Canada) [70] and laser scanning systems proposed by Poncet *et al.* [79] and Ajemba *et al.* [80], [81]. Several measures of torso deformity were also developed. Most of these were based on torso landmarks or other parameters of the imaging systems and generally suffered due to the existence of severe anthropometric differences due to growth. See Jaremko *et al.* [78], [82] for a comprehensive list and description of landmark based indices of torso deformity.

Statistics, machine learning and artificial intelligence tools were applied to landmark-based indices [66], [78], [82], [83] to: 1) assess changes in torso shape and symmetry; 2) classify scoliosis; and 3) predict the internal alignment of the

spine from torso shape. These applications yielded mixed results partly due to the technical limitations of the torso imaging systems used [70] but mostly because torso shape is influenced by spine shape, rib shape, muscle alignment, body fat, and skin characteristics in a largely undefined and changing manner which varies from one person to another [71], [80], [81] and [82]. Some researchers have questioned the clinical usefulness of these applications and have called for a new role for torso imaging in scoliosis clinics [84].

2.3.4 A novel rationale for using torso surface images in the routine management of scoliosis

Studies show that most scoliosis patients and their families are primarily concerned about the external deformity of the torso with its attendant social and psychological issues than the abnormal alignment of the spine [68]. Patients also seek treatment primarily because they are not satisfied with their cosmetic appearance [68], [76] and judge protocols for managing scoliosis by their effectiveness at checking or correcting torso asymmetry [75]. In addition, torso shape changes usually imply changes in the internal alignment of the spine and rib-cage [78].

This implies that both the internal and external deformities associated with scoliosis are useful measures that should dictate its management and treatment [68]. As spinal deformity is not easily deciphered from torso deformity and torso shape cannot be predicted from spinal shape, abnormal torso and spinal shape should be viewed as related but separate manifestations of spinal deformity [85], [86], [87], [88], [89]. This is the novel rationale for the inclusion of torso surface imaging in the routine assessment of patients in a growing number of scoliosis clinics [90].

The ability to detect change and classify scoliosis with radiographs alone is limited as accuracy in measuring Cobb angles ($3\text{-}10^0$) spans the threshold of clinically

relevant change seen between typical clinic visits (5^0 over 6 months). Using additional measures of deformity such as torso shape will improve the predictive value of detecting clinically relevant change and clinical classifications. True change is most certain when both the internal and the external measures of the deformity reveal a change [90]. In this case the confidence in the predicted outcome or classification would be increased. On the other hand, careful consideration would be given to those cases where only the internal or external measures record a change or a different classification as this may reveal occult issues [88], [90].

2.3.5 Pertinent gaps in knowledge

Traditional methods for assessing torso shape are based on landmarks. As the torso is relatively smooth, it is difficult to precisely locate these landmarks in real time. Also, the large anthropometric variations in the population means that the relative locations of torso landmarks vary significantly amongst patients. Finally, landmarks are particularly prone to the effects of posture variations, sway and breathing that usually occur during the acquisition of torso images. These effects are a function of being alive and cannot be completely eliminated. These difficulties call for the use of shape analysis methods for characterizing and describing torso shape changes caused by scoliosis.

2.4 RANGE SCANNING SYSTEMS

Section 2.3 described the use of torso surface images for assessing and monitoring scoliosis. The process of acquiring images of surfaces such as the human torso using light sources such as lasers is called range scanning. In this section, we describe a typical range scanning system. We list other applications of range scanning systems and describe some of the problems associated with acquiring images of the torso using range scanning systems.

2.4.1 The operation of a typical range scanning system

The range scanning system we describe is based on the Minolta VIVID 700 laser digitizer. The digitizer uses *optical triangulation*. The fundamental principle is shown in Fig. 2.5A [91]. A narrow light beam shines on a spot on the surface of an object. If the surface is not totally matte, this beam is scattered in many directions, and a camera records an image of the lighted spot. The center pixel of this spot is found and a line of sight traced through the pixel until it intersects the illumination beam at a point on the surface. This yields a single range point. To obtain the coordinates of an entire surface, the laser beam is systematically swept all over the surface of the object using mirrors. In the VIVID 700 digitizer, the beam is fanned into a sheet of laser light as shown in Fig. 2.5B. This casts a stripe onto the surface of the object which is then captured using a conventional CCD camera. For each camera scan line of each stripe, the centre pixel is computed and a line of sight traced to intersect the corresponding portion of the laser beam. This yields a range profile of the object. The shape of an object can be obtained by sweeping the laser beam over its surface.

The Minolta VIVID 700 digitizer is portable and standalone and uses an eye-safe laser beam and a galvanometer-mirror to sweep the beam over the object at a resolution of 200 by 200 and 256 levels (8-bits) per point. Its digital camera has a resolution of 400 by 400 pixels. It has a SCSI interface and takes about 0.6 seconds to sweep the laser beam over the object and about 2 seconds for data transfer to its host computer. The cloud of range points obtained is triangulated and converted into a 3D surface. The digital camera captures the texture map independent of the cloud of points. The triangulated range data can be obtained in a variety of formats including ASCII and Wavefront. The texture map can be exported with the range data or stored as a separate TIFF or UNIX RGB file.

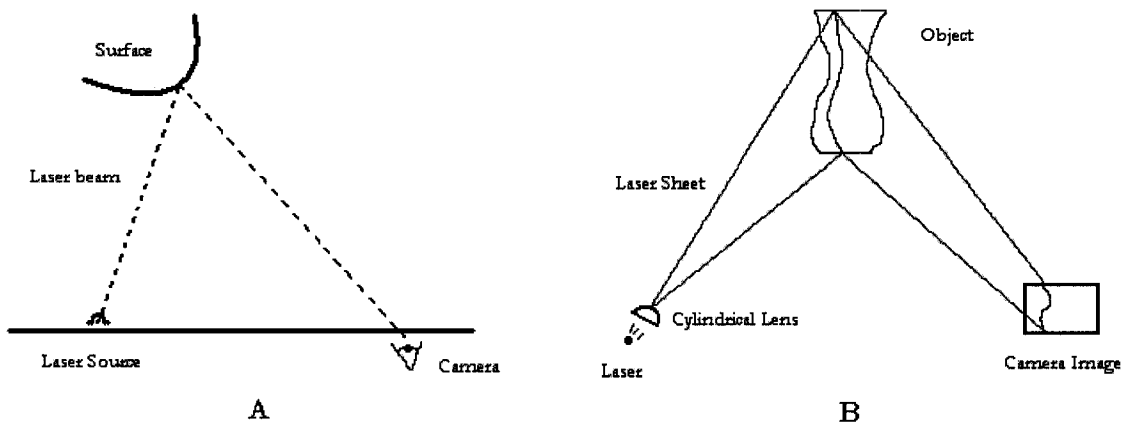

Fig. 2.5: Active triangulation principle.

2.4.2 Generating a complete model of the torso

To obtain a complete model of the human torso, the general procedure is to obtain several partial views of the surface from a number of angles in a way that covers the entire surface of the torso and then merge the partial views to form a complete torso surface. For the VIVID 700 digitizer, four (or six) partial views of the torso are used.

We carried out experiments to determine the optimum configuration for imaging stationary objects [81]. The experiments made use of ten scans of a calibration box obtained from four and six partial views. In each position, the box was 210 mm away from the digitizer. The results obtained using four and six partial views were indistinguishable but the six-partial-view configuration took 50% longer for image acquisition. To minimize the acquisition time and thereby reduce the effect of sway and breathing when scanning humans, the four-partial-view configuration was adopted. The four views were obtained by placing the digitizer in the four positions relative to the subjects shown in Fig. 2.6. In the single digitizer configuration, the subject was placed on a rotating positioning platform and rotated by 90^0 after each scan. Fig. 2.7 shows the single digitizer and a cast of the torso of a scoliosis patient.

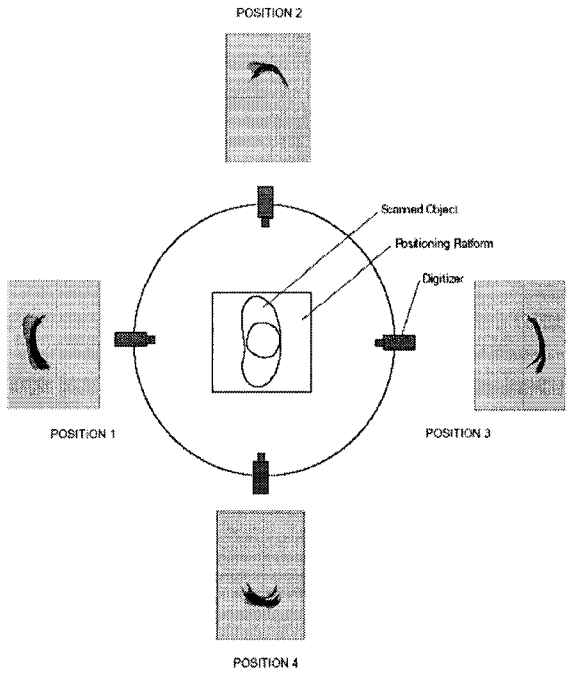

Fig. 2.6: The four positions of the digitizer.

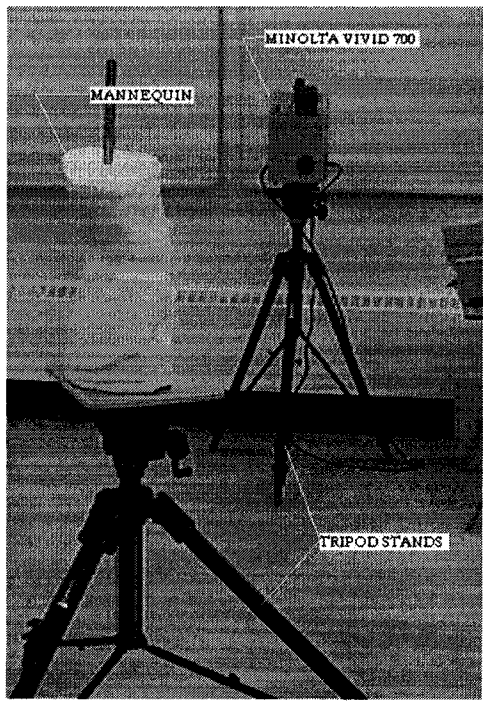

Fig. 2.7: A single Minolta digitizer and the mannequin.

Prior to merging, the partial views were aligned, transformed into a common coordinate system and registered. Merging consisted of determining the *best* surface in areas of overlap between the partial views using spline interpolation techniques [86]. Fig. 2.8 shows views of the rendered polygonal mesh of the cast from the alignment, registration and merging process. Fig. 2.8a-d shows the four views of the cast before alignment, registration and merging. Fig. 2.8e shows the views after alignment and registration and Fig. 2.8f shows the views after merging. A 3D texture map was obtained from each of the four views. For an average sized torso, the polygonal mesh obtained contained over 100 000 vertices. The data can be sub-sampled for easier manipulation by varying the reconstruction parameters.

2.4.3 Other uses of range scanning systems

Modern range scanning systems have found applications in such areas as robotics [92], image guided surgery [93], medical imaging [94], [95], electronic component testing [96] and computer graphics [97], [98]. Range scanning systems are used in medical imaging as an aid in planning reconstructive surgery [99], prosthetics manufacture and brace design. In computer graphics, range scans of objects are used to create their 3D animations [97].

Many range scanning systems capture the shape of objects by reflecting laser beams (or structured light) off the objects' surface to obtain the coordinates and other attributes of clouds of 3D points that describe a mesh representation of the object. The obtained mesh usually requires further processing before it can be used for most applications [100]. Capturing occlusion and hole-free surfaces remains a challenge due to errors in reflecting the laser beams from high-reflectance surfaces and the limitations of the reconstruction algorithms employed.

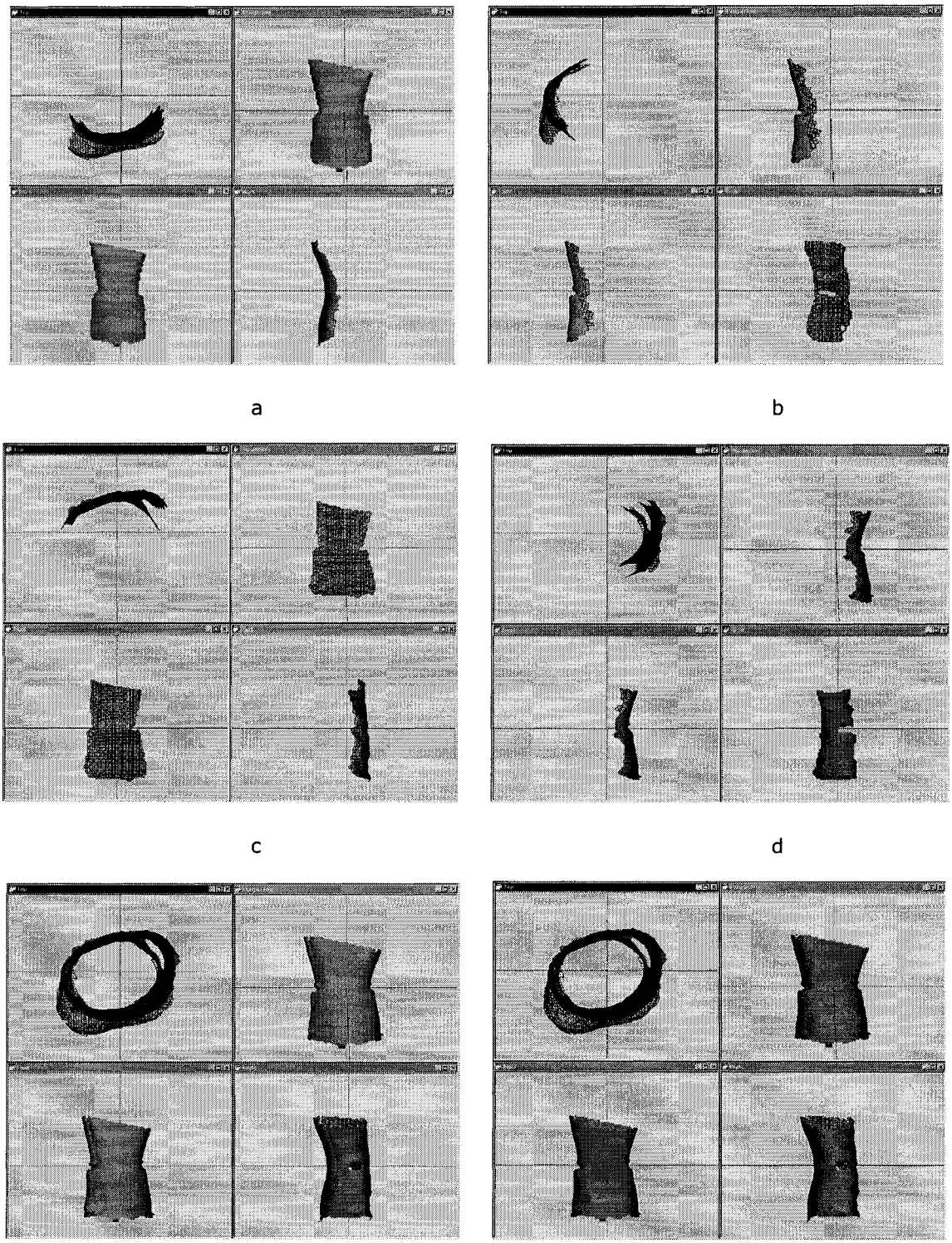

Fig. 2.8: The image merging process

2.4.4 Problems peculiar to torso imaging

Range scans of human torsos exhibit several problems and require an elaborate pre-processing stage before they can be used to assess torso deformities. First, stray data points from surrounding artefacts such as the positioning platform and garments that are not of interest can be arbitrarily positioned vis-à-vis the scanned object and have to be manually removed. Second, regions such as the head and neck and the shoulders and arms are often asymmetrically aligned and hence difficult to crop. Third, holes due to the occlusion of parts of the surface and grazing angles of incidence of the laser beam are often located in obscure regions like under the arms. Fourth, additional errors can be introduced during initial processing operations such as merging and smoothing.

The solutions to these problems are beyond the scope of this thesis. However, we correct for their effect using a suite of pre-processing procedures (Chapter 8).

REFERENCES

1. F. L. Bookstein, Morphometric Tools for Landmark Data: Geometry and Biology. Cambridge University Press, 1991.
2. D. Kendall, 'Shape manifolds, procrustean metrics and complex projective spaces,' *Bulletin of the London Mathematical Society*, vol. 16, pp 81-121, 1984.
3. E. Goldmeier, 'Similarity in visually perceived forms,' *Psychological issues*, vol. 8, no. 1, pp. 1-135, 1936/1972.
4. M. Hagedoorn, 'Pattern matching using similarity measures,' PhD thesis, Universiteit Utrecht, 2000.
5. C. Zahn and R. Roskies, 'Fourier descriptors for plane closed curve,' *IEEE Transactions on Computers*, vol. 21, no. 3, pp. 269-281, Mar. 1972.
6. D. Sharvit, J. Chan, H. Tek, and B. Kimia, 'Symmetry-based indexing of image databases,' *Journal of Visual Comm. and Image Representation*, vol. 9, no. 4, pp. 366-380, Dec 1998.
7. Y. Gdalyahu and D. Weinshall, 'Flexible syntactic matching of curves and its applications to automatic hierarchical classification of silhouettes,' *IEEE Transactions on Pattern Analysis and Machine Intelligence*, vol. 21, no. 12, pp. 1312-1328, Dec. 1999.
8. L. J. Latecki, R. Lakamper, and U. Eckhardt, 'Shape descriptors for non-rigid shapes with a

single closed contour,' *Proceedings of the IEEE Conference on Computer Vision and Pattern Recognition*, pp. 424-429, 2000.

9. F. Mokhtarian, S. Abbasi, and J. Kittler, 'Efficient and robust retrieval by shape content through curvature scale space,' Image Databases and Multi-Media Search, A. W. M. Smeulders and R. Jain, eds., pp. 51-58, *World Scientific*, 1997.
10. D. Huttenlocher, G. Kladerman, and W. Rucklidge, 'Comparing images using the Hausdorff distance,' *IEEE Transactions on Pattern Analysis and Machine Intelligence*, vol. 15, no. 9, pp. 850-863, Sept. 1993.
11. D. Gavrila and V. Philomin, 'Real-time object detection for smart vehicles,' *Proceedings of the Seventh International Conference on Computer Vision*, pp. 87-93, 1999.
12. S. Sclaroff and A. Pentland, 'Modal matching for correspondence and recognition,' *IEEE Transactions on Pattern Analysis and Machine Intelligence*, vol. 17, no. 6, pp. 545-561, June 1995.
13. H. Chui and A. Rangarajan, 'A new algorithm for non-rigid point matching,' *Proceedings of the IEEE conference on computer vision and pattern recognition*, p. 44-51, June 2000.
14. Y. Lamdan, J. Schwartz, and H. Wolfson, 'Affine invariant model-based object recognition,' *IEEE Transactions on Robotics and Automation*, vol. 6, pp. 578-589, 1990.
15. Y. Amit, D. Geman, and K. Wilder, 'Joint induction of shape features and tree classifiers,' *IEEE Transactions on Pattern Analysis and Machine Intelligence*, vol. 19, no. 11, pp. 1300-1305, Nov. 1997.
16. T. K. Leung, M. C. Burl, and P. Perona, 'Finding faces in cluttered scenes using random labelled graph matching,' *Proceedings of the fifth international conference on computer vision*, pp. 637-644, 1995.
17. C. Schmid and R. Mohr, 'Local grayvalue invariant for image retrieval,' *IEEE Transactions on Pattern Analysis and Machine Intelligence*, vol. 19, no. 5, pp. 530-535, May 1997.
18. D. G. Lowe, 'Object recognition from local scale-invariant features,' *Proceeding of the seventh international conference on computer vision*, pp. 1150-1157, Sept. 1999.
19. S. Belongie, J. Malik, and J. Puzicha, 'Shape matching and object recognition using shape contexts,' *IEEE Transactions on Pattern Analysis and Machine Intelligence*, vol. 24, no. 4, pp. 509–522, 2002.
20. C. Grigorescu, and N. Petkov, 'Distance Sets for Shape Filters and Shape Recognition,' *IEEE Transactions on Image Processing*, vol. 12, no. 10, pp. 1274-1286, October 2003.
21. A. Ghosh and N. Petkov, 'Robustness of Shape Descriptors to Incomplete Contour Representations,' *IEEE Transactions on Pattern Analysis and Machine Intelligence*, vol. 14, no. 11, 2005.
22. A. Yuille, 'Deformable templates for face recognition,' J. *Cognitiive Neuroscience*, vol. 3, no. 1, pp. 59-71, 1991.
23. M. Lades, C. Vorbuggen, J. Buhmann, *et al.*, 'Distortion invariant object recognition in the dynamic link architecture,' *IEEE Transactions on Computers*, vol. 42, no. 3, pp. 300-311,

Mar. 1993.

24. T. Vetter, M. J. Jones, and T. Poggio, 'A bootstrapping algorithm for learning linear models of object classes,' *Proceedings of the IEEE Conference on Computer Vision and Pattern Recognition*, pp. 40-46, 1997.
25. T. Cootes, D. Cooper, C. Taylor, and J. Graham, 'Active shape models-their training and application,' *Computer Vision and Image Understanding (CVIU)*, vol. 61, no. 1, pp. 38-59, Jan. 1995.
26. L. Sirovich and M. Kirby, 'Low dimensional procedure for the characterization of human face,' *Journal of the Optical Society of America-AI,* vol. 4, no. 3, pp. 519-524, 1987.
27. M. Turk and A. Pentland, 'Eigenfaces for recognition,' *Journal of Cognitive Neuroscience*, vol. 3, no. 1, pp. 71-96, 1991.
28. B. Moghaddam, T. Jebara, and A. Pentland, 'Bayesian face recognition,' *Pattern Recognition*, vol. 33, no. 11, pp. 1771-1782, Nov, 2000.
29. Y. LeCun, L. Bottou, Y. Bengio, and P. Haffner, 'Gradient-based learning applied to document recognition,' *Proceedings of the IEEE*, vol. 86, no. 11, pp. 2278-2324, Nov 1998.
30. M. Oren, C. Papageorgiou, P. Sinha, E. Osuna, and T. Poggio, 'Pedestrian detection using wavelet templates,' *Proceedings of the IEEE Conference on Computer Vision and Pattern Recognition*, pp. 193-199, June, 1997.
31. F. Attneave, 'Some Informational Aspects of Visual Perception,' *Psychology Review*, vol. 61, no. 3, pp. 183-193, 1954.
32. C. Teh and R. T. Chin, 'On the Detection of Dominant Points on Digital Curves,' *IEEE Transactions on Pattern Analysis and Machine Intelligence*, vol. 11, no. 8, pp. 859-872, 1989.
33. T. Pavlidis, 'Algorithms for shape analysis and waveforms,' *IEEE Transactions on Pattern Analysis and Machine Intelligence*, vol. PAMI-2, pp. 301-12, 1980.
34. P. Y. Yin, 'A discrete particle swarm algorithm for optimal polygonal approximation of digital curves,' *Journal of Visual Communication and Image Representation,* vol. 15, no. 2, pp. 241-260, 2004.
35. M. Marji, P. Siy, 'Polygonal representation of digital planar curves through dominant point detection - a nonparametric algorithm,' *Pattern Recognition,* vol. 37, no. 11, 2004.
36. D. S. Guru, R. Dinesh, 'Non-parametric adaptive region of support useful for corner detection: a novel approach, ' *Pattern Recognition,* vol. 37, no. 1, 2004.
37. B. Boucheham, Y. Ferdi, M. C. Batouche, 'Recursive versus sequential multiple error measures reduction: A curve simplification approach to ECG data compression,' *Computer Methods and Programs in Biomedicine, vol.* 81, no. 2, pp. 162-173, 2006.
38. T. M. Cronin, 'A boundary concavity code to support dominant point detection,' *Pattern Recognition Letters,* vol. 20, no. 6, pp. 617-634, 1999.
39. F. Arrebola, A. Bandera, P. Camacho, F. Sandoval, 'Corner detection by local histograms of

contour chain code,' *Electronic Letters,* vol. 33, no. 21, pp. 1769-1771, 1997.

40. J. M. Sanchiz, F. Pla, J. M. Inesta, 'Using neural networks to detect dominant points in chain-coded contours,' *International Journal of Pattern Recognition and Artificial Intelligence,* vol. 12, no. 5, pp. 661-675, 1998.
41. S. F. Qin, D. K. Wright, I. N. Jordanov, 'On-line segmentation of freehand sketches by knowledge-based nonlinear thresholding operations,' *Pattern Recognition*, vol. 34, no. 10, pp. 1885-93, 2001.
42. J. Basak, D. Mahata, 'A connectionist model for corner detection in binary and gray images,' *IEEE Transactions on Neural Networks,* vol. 11, no. 5, pp. 1124-1132, 2000.
43. W. H. Lin, J. S. Lee, C. H. Chen, Y. N. Shun, 'A new multiscale-based shape recognition method,' *Signal Processing,* vol. 65, no. 1, pp. 103-113, 1998.
44. P. Liatsis, C. Ooi, J. Y. Goulermas 'GA-based system for critical points detection,' *Electronic Letters*, vol. 42, no. 21, pp. 1207-1208, 2006.
45. P. Y. Yin, 'A new method for polygonal approximation using genetic algorithms,' *Pattern Recognition Letters,* vol. 19, no. 11, pp. 1017-1026, 1998.
46. P. W. M. Tsang, 'A genetic algorithm for aligning object shapes,' *Image and Vision Computing*, vol. 15, no. 11, 1997.
47. F. Mokhtarian and A. Mackworth, 'A Theory of Multiscale Curvature-Based Shape Representation for Planar Curves,' *IEEE Transactions on. Pattern Analysis and Machine Intelligence*, vol. 14, no. 8, pp. 789-805, 1992.
48. P. Y. Yin, 'Ant colony search algorithms for optimal polygonal approximation of plane curves,' *Pattern Recognition*, vol. 36, no. 8, pp. 1783-1797, 2003.
49. J. Fayolle, L. Riou, C. Ducottet, 'Robustness of a multiscale scheme of feature points detection,' *Pattern Recognition,* vol. 33, no. 9, pp. 1437-1453, 2000.
50. Y. P. Wang, S. L. Lee, K. Toraichi, 'Multiscale curvature-based shape representation using B-spline wavelets,' *IEEE Transactions on Image Processing,* vol. 8, no. 11, pp. 1586-1592, 1999.
51. B. Boucheham, Y. Ferdi, M. C. Batouche, 'Piecewise linear correction of ECG baseline wander: a curve simplification approach,' *Computer Methods and Programs in Biomedicine,* vol. 78, no. 1, pp. 1-10, 2005.
52. C. L. Lin, T. C. Chuang, K. C. Fan, 'Palmprint verification using hierarchical decomposition,' *Pattern Recognition,* vol. 38, no. 12, 2005.
53. H. Park, J. H. Lee, 'B-spline curve fitting using dominant points,' *Computational Science – ICCS 2006, PT 2, Proceedings, Lecture Notes in Computer Science*, vol. 3992, pp. 362-366, 2006.
54. P. Ganguly, 'Modified Arc tree based hierarchical representation of digital curve,' *Pattern Recognition Letters,* vol. 27, no. 6, 2006.
55. Y. Gao, 'Efficiently comparing face images using a modified Hausdorff distance,' *IEE Proceedings – Visual Image and Signal Processing, vol. 150, no. 6, pp.* 346-350, 2003.

56. E. Fatemizadeh, C. Lucas, H. Soltanian-Zadeh, 'Automatic landmark extraction from image data using modified growing neural gas network,' *IEEE Transactions on Information Technology in Biomedicine,* vol. 7, no. 2, pp. 77-85, 2003.
57. Y. Zhu, L. D. Seneviratne, 'On the recognition and location of partially occluded objects,' *Journal of Intelligent and Robotic Systems,* vol. 25, no. 2, pp. 133-151, 1999.
58. V. S. Chakravarthy, B. Kompella, 'The shape of handwritten characters,' *Pattern Recognition Letters*, vol. 24, no. 12, pp. 1901-1913, 2003.
59. D. T. Giang, R. Plamondon, C. J. Zhu, Y. Li, 'Detection of control points for warping map images,' *Intelligent Automation and Soft Computing,* vol. 7, no. 3, pp. 205-217, 2001.
60. G. Ritter, C. Schreib, 'Using dominant points and variants for profile extraction from chromosomes,' *Pattern Recognition,* vol. 34, no. 4, pp. 923-938, 2001.
61. B. Sarkar, S. Roy, D. Sakar, 'Hierarchical representation of digitized curves through dominant point detection,' *Pattern Recognition Letters,* vol. 24, no. 15, 2003.
62. W. Y. Wu, 'Two-dimensional object recognition through string matching,' *Imaging Science Journal*, vol. 49, no. 4, 213-221, 2001.
63. V. J. Raso, *et al.*, 'Trunk distortion in adolescent idiopathic scoliosis,' *Journal of Pediatric Orthopedics*, vol. 18, no. 2, pp 222-226, 1998.
64. J. R. Cobb, Outline for the study of scoliosis, instructional course lectures, The American academy of orthopedic surgeons 5, pp 261-275, 1948.
65. R. Levy, M. S. Goldberg, N. E. Mayo, J. A. Hanley and B. Poitras, 'Reducing the lifetime risk of cancer from spinal radiographs among people with adolescent idiopathic scoliosis,' *Spine*, vol. 21, pp 1540-1548, 1996.
66. I. A. F. Stokes, M. S. Moreland, 'Concordance of back surface asymmetry and spine shape in idiopathic scoliosis,' *Spine*, vol. 14, pp. 73-78, 1989.
67. T. N. Theologis, R. J. Jefferson, A. H. Simpson, A. R. Turner-Smith, and J. C. T. Fairbank, Quantifying the cosmetic defect of adolescent idiopathic scoliosis, *Spine*, 18, pp. 909–912, 1995.
68. R. A. Dickson, 'Spinal Deformity - Adolescent Idiopathic Scoliosis: Nonoperative Treatment,' *Spine*, vol. 24, no. 24, pp 2601-2606, 1999.
69. E. Hierholzer and W. Frobin, 'Rasterstereography measurement and curvature analysis of scoliosis surfaces,' in Moreland, M. S., Pope, M. H., and Armstrong, G. W. D. (Eds): 'Moire fringe topography and spinal deformity,' pp 267-276, Pergamon Press, 1981.
70. V. Pazos, F. Cheriet, L. Song, H. Labelle, J. Dansereau, 'Accuracy assessment of human trunk surface 3D reconstructions from an optical digitising system,' *Medical and Biological Engineering and Computing*, 43, pp. 11-15, 2005.
71. C. J. Goldberg, M. Kaliszer, D. P. Moore, E. E. Fogarty, F. E. Dowling, 'Surface topography, Cobb angles and cosmetic change in scoliosis,' *Spine*, vol. 26, pp E55-63.
72. M. A. Hoke, 'A study of a case of lateral curvature of the spine: report on an operation for the deformity,' *American Journal of Orthopaedic. Surgery*, vol. 1, pp 168-208, 1903.

73. M. S. Moreland, M. H. Pope, D. G. Wilder, I. A. Stokes and J. W. Frymoyer, 'Moire fringe topography of the human body,' *Medical Instrumentation*, vol. 15, pp 129-32, 1981.
74. T. N. Theologis, J. C. Fairbank, A. R. Turner-Smith, T. Pantazopoulos, 'Early Detection of Progression in AIS by Measurement of Changes in Back Shape With the Integrated Shape Imaging System Scanner,' *Spine*, vol. 22, no. 11, pp 1223-1227, 1997.
75. C. J. Goldberg, E. E. Fogarty, D. P. Moore, and F. E. Dowling, 'Scoliosis Imaging and the Problem of Postural Sway' *in Sevastik, J. A and Khaled, M. D. (Eds.) Research into spinal deformities 1: (IOS Press, Oxford)*, 1997.
76. L. Hackenberg, E. Hierholzer, W. Potzl, C. Gotze, and U. Liljenqvist, 'Raster-stereographic back shape analysis in idiopathic scoliosis after anterior correction and fusion,' *Clinical Biomechanics,* vol. 18, pp 1-8, 2003.
77. D. L. Hill, D. C. Berg, V. J. Raso, E. Lou, N. G. Durdle, J. K. Mahood, and M. J. Moreau, 'Evaluation of a laser scanner for surface topography' *in Peuchot, A. (Ed.) Research into spinal deformities 3 (IOS Press, Oxford),* 2003.
78. J. L. Jaremko, P. Poncet, J. Ronsky, J. Harder, J. Dansereau, H. Labelle and R. F. Zernicke, 'Estimation of spinal deformity in scoliosis from torso surface cross sections,' *Spine*, vol. 26, no. 14, pp 1583-1591, 2001.
79. P. Poncet, S. Delorme, J. L. Ronsky, J. Dansereau, G. Clynch, J. Harder, R. D. Dewar, H. Labelle, P. Gu, and R. F. Zernicke, 'Reconstruction of Laser-scanned 3D Torso Topography and Stereoradiographical Spine and Rib-cage Geometry in Scoliosis' *Computer Methods in Biomechanics and Biomedical Eng*, vol. 4, pp 59-75, 2000.
80. P. O. Ajemba, N. G. Durdle, D. L. Hill, and V. J. Raso, 'A Torso Imaging System for Quantifying the Deformity Associated with Scoliosis,' To appear in the *IEEE Transactions on Instrumentation and Measurement*, vol. 56, no. 5, October 2007.
81. P. O. Ajemba, N. G. Durdle, D. L. Hill, and V. J. Raso, 'A Torso Imaging System for Quantifying the Deformity Associated with Scoliosis,' *In Proceedings of the IEEE Instrumentation and Measurement Technology Conference*, Ottawa, 17–19 May, 2005
82. J. L. Jaremko, P. Poncet, J. Ronsky, J. Harder, J. Dansereau, H. Labelle and R. F. Zernicke, 'Indices of torso asymmetry related to spinal deformity in scoliosis,' *Clinical Biomechanics*, 17, pp. 559–568, 2002.
83. B. Drerup, E. Hierholzer, 'Assessment of scoliotic deformity from back shape asymmetry using an improved mathematical model,' *Journal of Biomechanics*, 11(7), pp 376-383, 1996.
84. I. A. F. Stokes, 'Point of View: Estimation of spinal deformity in scoliosis from torso surface cross sections,' *Spine*, vol. 26, no. 14, pp 1591, 2001.
85. P. O. Ajemba, N. G. Durdle, D. L. Hill, and V. J. Raso, 'Accuracy assessment of a complete human torso topographic analysis system for assessing trunk deformities,' To appear in *Computers in Biology and Medicine*, 2007.
86. P. O. Ajemba, N. G. Durdle, D. L. Hill, and V. J. Raso, 'Effect of Posture on a Full Torso

Imaging System for the Assessment of Scoliosis,' *Proceedings of the 2004 Conference of Intl Resch Society for Spinal Deformities*, Vancouver, Canada, June 10-12, 2004.

87. P. O. Ajemba, N. G. Durdle, D. L. Hill, and V. J. Raso, 'Re-positioning Effects on a Full Torso Imaging System for the Assessment of Scoliosis,' *Proceedings of the 2004 IEEE Canadian Conference on Elect and Comp Eng*, Niagara Falls, Canada, May 2-5, 2004.
88. P. O. Ajemba, A. Kumar, N. G. Durdle, and V. J. Raso, 'Quantifying torso deformity in scoliosis,' *Proceedings of the SPIE*, Vol. 6144, 614450, 2006.
89. P. O. Ajemba, N. G. Durdle, D. L. Hill, and V. J. Raso, 'Posture and re-positioning considerations of a complete torso topographic analysis system for assessing scoliosis,' *Proceedings of the SPIE*, Vol. 6056, 60560O, 2006.
90. P. O. Ajemba, N. G. Durdle, D. L. Hill, and V. J. Raso, 'Classifying torso deformity in scoliosis using orthogonal maps of the torso,' *Medical and Biological Engineering and Computing*, vol. 45, pp. 575-584, June 2007.
91. B. Curless, From Range Scans to 3D Models, Computer Graphics, 33 (4), pp 38, 1999.
92. A. Walthem, 'A new approach to global self-localization with laser range scans in unstructured environments,' *Proceedings of the 4th IEEE Intelligent Vehicle Symposium*, Vol. 1, pp 202-8, 2002
93. D. M. Cash, T. K. Sinha, W. C. Chapman, H. Terawaki, *et al.* 'Incorporation of a laser range scanner into image-guided liver surgery: surface acquisition, registration, and tracking,' *Medical Physics*, vol. 30, pp 1671-82, 2003.
94. M. I. Miga, T. K. Sinha, D. M. Cash, R. L. Galloway, R. J. Weil, 'Cortical Surface Registration for Image-Guided Neurosurgery Using Laser-Range Scanning,' *IEEE T. Medical Imaging*, vol. 22, no. 8, 2003.
95. L. P. Muren, R. Smaaland, O. Dahl, 'Organ motion, set-up variation and treatment margins in radical radiotherapy of urinary bladder cancer,' *Radiotheraphy and Oncology*, vol. 69, pp 291-304, 2003.
96. G. Ruifeng, S. Venkataraman, 'A new technique for scan chain failure diagnosis,' *Proceedings of 28th International Symposium for Testing and Failure Analysis*, pp 723-32, 2002.
97. B. Allen, B. Curless, Z. Popovic, 'Articulated body deformation from range scan data,' *ACM Transactions on Graphics*, vol. 21, pp 612-19, 2002.
98. Y. Ma, H. Zhang, S. Jiang, 'Realistic Modeling and Animation of Human Body Based on Scanned Data,' *Journal of Computing Science and Technology*, vol. 19, no. 4, pp 529-537, 2004.
99. A. Cataloglu, R. E. Clark, P. L. Gould, 'Stress analysis of aortic valve leaflets with smoothed geometrical data,' *Journal of Biomechanics*, vol. 10, pp 153-158, 1977.
100. P. V. Sankar, M. J. Silbermann, and L. A. Ferrari, 'Curve and Surface Generation and Refinement Based on a High Speed Derivative Algorithm,' *Graphical Models and Image Processing*, vol. 56, No. 1, pp 94-101, 1994.

CHAPTER 3

STRUCTURED SPLINES MODELS: THEORY AND VALIDATION [N]

3.1 INTRODUCTION

In this chapter, we consider the problem of quantifying the shape of a deformable 3-D object in order to compare its shape to those of similar objects and track its shape changes over time. This is an example of shape analysis of deformable objects, an important problem in computer vision and pattern recognition. A robust, accurate solution would facilitate applications such as disease prognosis from the analysis of human organ shape and tracking and measuring changes in 3-D objects from 4-D data. We require that our solution be intuitive and rely on perceptible surface features such as curvature and symmetry. To be practical, we also require our solution to be able to estimate 3-D shape from incomplete point sets (obtained from range scanning or segmentation) by first reconstructing the data.

3.1.1 Outline

We propose a three-step solution to this problem (Fig. 3.1). First, the 3-D object's surface is modelled as a structured sequence of cross-sections based on a geometric property of 3-D shapes called volume constancy. The sequence of cross-sections obtained this way is shown to be invariant to positioning and affine (orthographic and semi-perspective) transformations. Second, feature points that describe the local curvature of a cross-section are extracted from each of the structured cross-sections as perception of a shape is chiefly influenced by local curvature [1]. Third, the

[N] A version of this chapter has been submitted for publication. P. O. Ajemba, N. G. Durdle, and V. J. Raso, 'Quantifying torso deformity using dominant points obtained from structured splines models,' *IEEE Transactions on Image Processing*, 2007.

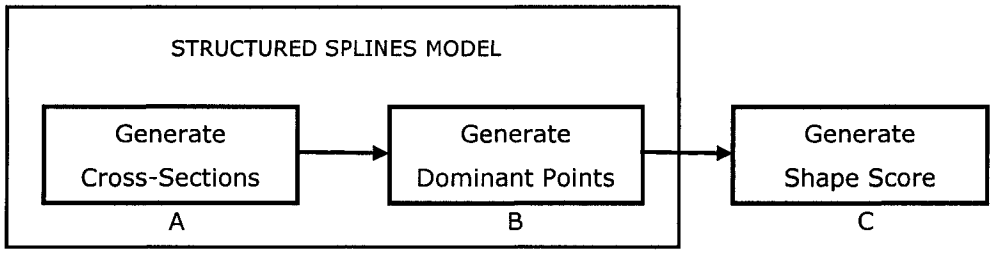

Fig. 3.1: Schematic diagram of the structured splines model.

aggregated set of points is used to develop a multi-axial shape vector which in turn is used to quantify and track the shape of the deformable 3-D object.

The main contributions of this chapter are: 1) a technique for obtaining structured sequences of cross-sections of deformable 3-D objects; 2) a minimum error estimation technique for interim shape matching during feature point selection based on the shape context technique [2]; 3) a multi-axial shape vector for quantifying shape that takes into account symmetries and near symmetries; and 4) a technique for classifying and tracking 3-D shape. In addition, this study builds in non-trivial ways on curvature based shape description to address the problem of 3-D shape quantification and tracking of deformable objects.

3.2 BACKGROUND AND RELATED WORK

Shape description and matching is a fast evolving field and reviewing it extensively is beyond the scope of this work. Good reviews of the field can be found in [3] and [4]. Existing methods can be classified into feature-based or content-based methods. Feature-based methods make use of information obtained from the edges of an image [5]. The edges of interest include silhouettes (or the exterior edges), but may also include interior edges like letterings [6]. Content-based methods make use of information in the interior of the image in addition to the edge information [7]. This includes pixel colours and areas in 2-D images, voxel colours and volumes in 3-D images, as well as the distribution of pixels and voxels. [8].

We are interested in 2-D boundary based methods (a sub-class of feature-based methods) as they can be extended to 3-D and used for our application.

Feature-based methods can be further classified into local, global and hybrid methods. Global methods take into account the overall shape of the object. An example is the medial axis transform [9] and moment-based techniques [10], [11]. Local methods focus on local properties of shapes such as curvature. They include Mokhtarian and Mackworth's curvature scale space methods [12] and spline based methods such as [13]. Hybrid methods combine both global and local characteristics of shapes. Examples of such techniques are rich descriptors like shape contexts [2] and distance multisets [14] which use global descriptors of local coordinates.

Attneave [1] observed that the edges of a curve are its most important visual components. As we require that our choice of shape descriptors be based on the human visual perception of shape, we limit our search to methods that utilize local shape features such as curvature. A subset of shape description methods are based on representing shape using points of local maximum curvature called dominant points [15]. A review of these methods is given in Chapter 2.

Finally, we require that the method chosen be able to determine 3-D shape from incomplete point sets obtained from range scanning or segmentation and include a data reconstruction routine. This suggests the use of a spline based technique for both surface reconstruction and dominant point detection. *B*-splines [16], [17] are the most basic of existing spline based methods and are used in this study.

3.3 PRELIMINARIES

3.3.1 *B*-spline basis functions and *B*-spline curves

B-spline curves are generated from piecewise polynomial functions called *B*-spline basis functions. They locally approximate a contour using a small number of

parameters called control points. We briefly describe the *B*-spline theory used in this chapter. A detailed treatment of the theory can be found in [18].

In 1915, Whittaker [19] proposed that given the values of a function f, corresponding to an infinite number of equidistant values of its arguments x_0, $x_0 + T$, $x_0 + 2T$, ... from which a table of interpolation can be constructed, there exists many functions which give rise to the same exact table, but only one has all *constituents* of period less than $2T$. He called it the *cardinal function* given as

$$C(x) = \sum_{k=-\infty}^{+\infty} f(x_0 + kT) \frac{\sin \frac{\pi}{T}(x - x_0 - kT)}{\frac{\pi}{T}(x - x_0 - kT)}. \qquad (1)$$

It reproduces its interpolating values as $C(x_0 + kT) = f(x_0 + kT)$ [20][2]. Schoenberg [16], [17] showed that a drawback of (1) is that the resulting functions do not necessarily yield smooth curves and cannot be used to generate osculatory curves.

Let

$$F(x) = \sum_n y_n L(x - n), \qquad (2)$$

where

$$L(x) = \frac{\sin \pi x}{\pi x} = \frac{1}{2\pi} \int_{-\pi}^{\pi} e^{ixu} du. \qquad (3)$$

---

[2] The *sampling theorem* proposed by Shannon [21] (researchers such as Kotel'nikov, Raabe and Someya have also been credited with this discovery [20]) follows from (1). Let F be a function that contains no frequencies higher than W cps. The *sampling theorem* deals with the reconstruction of the function using a pulse of type $\sin(2\pi Wx)/2\pi Wx \ldots$ where s_k is the k th sample. In this case, the function is given by the expression

$$F(x) = \sum_{k=-\infty}^{+\infty} s_k \frac{\sin \pi(2Wx - k)}{\pi(2Wx - k)}. \qquad (4)$$

Note that (4) corresponds to (1) when $x_0 = 0$ and $T = 1/2W$.

Then (2) is an interpolation formula if $F(n) = y_n$, for all n, and in this case if and only if $L(x)$ is such that $L(0) = 1$, but $L(i) = 0$ for all other integers $i \neq 0$. This is called a *cardinal series representation*. Note that the data is limited to one interpolating function per value. Now, (2) would be smoothing if $L(x) = L(-x)$ and for $|x| > p$, $L(x) = 0$, for some abscissa value p. The sequence in (2) can then be written as

$$F(x) = \sum_{r=-\infty}^{\infty} y_r L(x - r), \tag{5}$$

where (5) is finite as $L(p) = L(-p) = 0$. This is an example of a linear transformation or *time invariant filtering* in signal processing, with L the impulse response function. We next determine the condition under which F is smoothing. Using the properties of Fourier transforms and convolutions, from [18], (5) reads

$$\Im[F](\omega) = \Im[y](\omega)\Im[L](\omega), \tag{6}$$

where $\Im[\cdot]$ is the Fourier transform operator. Thus, in (6), $\Im[L]$ is the frequency response of the system. A smoothing filter is essentially a low pass filter, so $\Im[L](\omega)$ should be small or zero for large ω. We define the B-*spline basis function* of order k (and degree $k-1$) as the inverse Fourier transform of the product of k sinc functions, that is

$$M_k(x) = \frac{1}{2\pi} \int_{-\infty}^{\infty} \left(\frac{\sin(\omega/2)}{(\omega/2)} \right)^k e^{i\omega x} d\omega, \tag{7}$$

for k = 1, 2, ..., then

$$\Im[M_k](\omega) = \left(\frac{\sin(\omega/2)}{(\omega/2)} \right)^k.$$

Schoenberg [16] showed that (7) was equivalent to

$$M_k(x) = \frac{1}{(k-1)!} \delta^k x_+^{k-1}, \tag{8}$$

Where δ^k is the k th order central difference of a unit step [16], [18] and

$$x_+^{k-1} = \begin{cases} x^{k-1} & x \geq 0 \\ 0 & x < 0 \end{cases}.$$

From (3) and (7), the zeroth order *B*-spline basis function M_0 is the impulse function. The k th order continuous *B*-spline basis function is obtained from $k+1$ convolutions of M_0. That is

$$M_k(x) = M_0 * M_{k-1}(x) = M_0 * M_0 * \cdots * M_0(x). \qquad (9)$$

Note that $M_1(x) = M_0 * M_0(x)$, and M_k in (9) is equivalent to k convolutions of M_1. It follows that a *B*-spline basis function of order k represents the probability density function of the sum of k independent random variables with uniform distribution in the interval [-1/2, 1/2].

The discrete *B*-spline basis function of order k at scale level m is given as [12]

$$\mathrm{A}_m^k = \mathrm{A}_m^0 * \mathrm{A}_m^{k-1} = \mathrm{A}_m^0 * \mathrm{A}_m^0 * \cdots * \mathrm{A}_m^0. \qquad (10)$$

In (10), $\mathrm{A}_m^0 = 1/m \cdot [1,1,\cdots,1]$ is a normalized sampled pulse of width m.

The discrete sampled *B*-spline basis function of order k at resolution m is given as $a_m^k(t)$. It is obtained by directly sampling the k th-order continuous *B*-spline basis function at the scale m, as follows:

$$a_m^k(t) = \frac{1}{m} M_k\left(\frac{t}{m}\right), \ \forall t \in \mathrm{Z}. \qquad (11)$$

When $m=1$, the discrete sampled *B*-spline basis of order k is denoted as $a^k(t) = M_k(t)$. The inverse of the operator a^k in (11) is defined using the impulse response function $\mathrm{Im}(\cdot)$ as

$$(a^k)^{-1} * a^k(t) = \mathrm{Im}(t).$$

Computing *B*-spline basis functions from (7) and (8) is tedious. In this chapter, we use a numerical implementation [18].

Given two sequences of real numbers $U=\{u_i\}_{i=0}^{s}$ and $M=\{m_i\}_{i=0}^{s}$ called a breakpoint sequence and a multiplicity vector respectively, we define a non-decreasing sequence of real numbers $T=\{t_j\}$ called a knot vector, such that $m_i=card\{j:t_j=u_i\}$. Let T be given as $t_0\le t_1\le\cdots\le t_N$. For $n=0,\ldots,N$, and $i=0,\ldots,N-n$, the ith *B*-spline basis function of order k is defined for $k=1$ as:

$$M_{i,0}(t)=\begin{cases}1 & t_i\le t<t_{i+1}\\ 0 & otherwise\end{cases}. \qquad (12a)$$

For $k>1$, it is defined as:

$$M_{i,k}(t)=\begin{cases}\dfrac{(t-t_i)}{t_{i+k}-t_i}M_{i,k-1}(t)+\dfrac{(t_{i+1+k}-t)}{t_{i+1+k}-t_{i+1}}M_{i+1,k-1}(t), & t_i<t_{i+1+k}\\ 0 & otherwise\end{cases}. \qquad (12b)$$

Finally, let $P=\{p_i\}_{i=0}^{N}$ be a sequence of control points. A *B*-spline curve based on a set of *B*-spline basis functions $M_{i,n}(t)$, of order k, is defined for $k\ge 1$, using (12a) and (12b) as:

$$S_k(t)=\sum_{i=-\infty}^{\infty}p_i\cdot M_{i,k}(t-i)=\sum_{i=0}^{N}p_i\cdot M_{i,k}(t-i). \qquad (13)$$

3.3.2 Volume decomposition

Given our task of determining the dominant points of a 3-D object (i.e., a volume) we are faced with 3 options. First, model the volume as a surface, using polynomial interpolants. The dominant points can be obtained from the control points of the interpolated surface. Second, decompose the volume into a structured sequence of h 2-D cross-sections and then model the cross-sections using polynomial interpolants. The dominant points in this case can also be obtained from the control points of the sequence of h interpolated curves. Third, directly estimate the dominant points from the surface points using range data compression.

The first option produces an unstructured sequence of dominant points as the point locations are totally unconstrained. Though this may be useful for applications in computer graphics, it is undesirable in our case as our shape quantification routine requires our dominant points to have a quasi-structure as we hope to utilize them in deriving our deformation indices. The third option fails to make use of any curvature information, a desirable feature of our application.

We choose to go with the second option and use *B*-spline basis functions as our polynomial interpolants. Advantages of this choice include: 1) the existence of a quasi-structure on the dominant points obtained; 2) the local correction for holes, ambiguities and errors in the surface; 3) the possibility of very efficient surface recovery from the cross-sections obtained; and 4) the low computational cost incurred compared to the other options.

3.4 STRUCTURED SPLINES MODELS

3.4.1 From 3-D objects to 3-D cross-sections

In concrete terms, the problem we seek to solve is this: Given an object O made up of a collection of say $M \times N$ points, we want to extract a structured sequence of $h \times c$ points that are the dominant points of O's surface. Concisely,

$$O_{M\times N} \rightarrow O_{h,c}(t). \tag{14}$$

Wh$O_{M\times N} \rightarrow O_{h,c}(t)$ red sequence of points $O_{h,c}$ is given by:

$$O_{h,c}(t) = \bigcup_{j=0}^{h-1} S_k(t) = \bigcup_{j=0}^{h-1} \sum_{i=0}^{c-1} p_i \cdot M_{i,k}(t-i). \tag{15}$$

To create the theoretical framework for this process, we start by exploring the properties of a fundamental invariant of 3-D objects: volume constancy. This refers to a closed 3-D object retaining its volume in the presence of affine transformation.

Definition 1: For a simple closed 3-D surface (or object) O with a start point T and an end point E, a *regular set of cross-sections* is one that divides O into a number of equal volume segments independent of position, orientation and scale.

The planes of a regular set of cross-sections need not be parallel to each other but cannot intersect within the volume of the surface.

Definition 2: For a simple closed 3D surface O with a start point T and an end point E, its *centroid line* originates at T and ends at E and joins the centroids of the cross-sections of an infinite-sized regular set of cross-sections of O.

Corollary 1: For $h > 3$, a regular set of h cross-sections of a simple closed surface is unique and invariant to positioning and affine transformations.

Proof: Follows from Definitions 1 and 2. ■

Lemma 2: Let an affine transform $\Gamma_{A\to B}$ be applied to a simple closed surface O_A to obtain another simple closed surface O_B. Let L_A and L_B be the centroid lines of O_A and O_B respectively. Applying $\Gamma_{A\to B}$ to L_A yields L_B.

Proof: Let O_A be a simple closed surface with a start point T_A and an end point E_A. The surface of O_A can be decomposed into an infinite number of surface lines originating from T_A and ending at E_A. These surface lines would fall about L_A. Let O_B be the result of applying a transform $\Gamma_{A\to B}$ to O_A. O_B could also be similarly decomposed about its centroids line L_B. As geometric transforms are onto, each component surface line of O_A will be unique and correspond to a component surface line of O_B. If we apply a contraction operation on O_A and O_B centered around their respective centroids, and repeat the process of decomposing the resultant surfaces into lines and then mapping the lines of O_A into those of O_B, in the limit, both O_A and O_B would consist of their centroids which would map to each other ■

From Lemma 2, the shape similarity of centroid lines is equivalent to the shape similarity of the corresponding 3-D objects.

The formal definition of the structured splines model of a 3-D object is as follows:

Definition 3: Let each of the h regular cross-sections of a simple closed 3-D object O that consists of a cloud of $M \times N$ points be modeled by h interpolating curves S_k with c dominant points and *B*-spline basis functions $\alpha_{i,n} \in C^0$. The $h \times c$ matrix M formed by the structured sequence of dominant points is the structured splines model of O of order $h \times c \times k$.

Theorem 3: An $h \times c \times k$ order structured splines model of a simple closed 3-D object O is unique and captures the shape of the surface for $h, c = 3, \ldots, \infty$.

Proof: Follows from Corollary 1 and Definition 3. ■

Lemma 2 and Theorem 3 imply that structured splines models of 3-D objects are unique signature of the objects' shape. Thus, the shapes of different 3-D objects can be compared by comparing their structured splines models.

3.4.2 From 3-D cross-sections to dominant points

Our goal is to fit a set of m ($m > n+1$) ordered data points P, that lie on a curve S, with a real-valued *B*-spline, where

$$P = (p_1, p_2, \ldots, p_m) = \{[x_1, y_1, z_1]^T, [x_2, y_2, z_2]^T, \ldots, [x_m, y_m, z_m]^T\},$$

and $[\cdot]^T$ is the transpose operator. There are two methods to achieve this. The first method is to utilize P as the sequence of control points of the *B*-spline curve. As in (13), $M_k(x)$ could be used. In the limiting case, $k = 0$ and the points are not joined at all by $M_0(x)$. In this chapter, we obtain our ground truth curve using $k = 4$, thus, the points are joined by cubic polynomials.

The second method is to find a *B*-spline curve that fits the data points such that the *error* measured between the data points and their corresponding points on the *B*-spline curve is less than an error tolerance value ε_T. Ideally, let c be the number of control points of the approximating *B*-spline. Then, $c << m$, though $1 \leq c < m$ could be acceptable. The second method does not require many initialization parameters, achieves a data compression ratio of m/c and is noise resistant [13].

From sampling theory, let S_k be an interpolated version of a given a curve f. Let S_k be obtained using interpolating functions $M_{i,k} \in C^0$ and i control points. We can infer that

$$\lim_{i \to \infty} \| S_k - f \|_{k^\infty} = 0. \qquad (16)$$

In other words, there exists an interpolated version of f that will be an exact match for some number of control points i and some degree of the interpolated function k, as both terms increase infinitely. The limit in (16) is not very useful as we need bounded values for i and k.

Theorem 4: Let S_k and f be as given in (16). For *B*-spline basis functions $M_{i,k} \in C^0$ and some $c \in \mathrm{Z}$, there exists a set of points $D = \{d_i\}_{i=0}^{c}$ for which

$$\lim_{i \to c} \| S_k - f \|_{k^\infty} = 0. \qquad (17)$$

Proof: Mokhtarian and Mackworth [12] showed that the Gaussian can be used to obtain a scale space representation of a curve at varying resolutions (that is, number of inflection points[3]). They termed this the Gaussian scale space representation of the curve.

A scale space representation for *B*-spline curves was developed by Wang *et al.* [13]. Let $D = \{d_i\}_{i=0}^{c}$ be the input to S_k. From (13), a parameterization of f using

[3] Dominant points can be defined as points of inflection. This is the dual of their definition as points of local maximum curvature. We use the latter definition in this chapter.

$M_{i,0}$ is:

$$S_0(t) = \sum_i s_0(i) \cdot M_{i,0}^l(t-i). \quad (18)$$

where $s_0(t) = [x(t,0), y(t,0), z(t,0)]^T$ in (18). The approximation coefficient vector $s_0(i)$ is:

$$s_0(i) = (a^l)^{-1} * D(i). \quad (19)$$

Note that in (18), the discrete points D are not yet interpolated. They are just the original sampling points, as often used in Gaussian smoothing. The evolution of the curve at different resolution levels x is achieved by convolving the curve with a dilated *B*-spline basis function,

$$S(t,x) = S_0 * M_k^x(t) \quad (20)$$

where $M_k^x(t) = (1/x) \cdot M_k(t/x)$ denotes the kth-order *B*-spline at resolution x.

This scale space representation of *B*-spline curves so far is quite similar to the Gaussian scale space. By the central limit theorem, the *B*-spline basis function approximates the Gaussian as $k \to \infty$. Thus, as with the case of the Gaussian scale space, the evolution obtained from (18), (19) and (20) ensures that the curve S_k matches f exactly for some k value. ■

In practise, we do not have the liberty to use any arbitrary value for k. We seek a form of (17) where the order of k is fixed. In this chapter, we use $k = 4$. The resulting equation is

$$\lim_{i \to c} \| S_k - f \|_{k^4} \leq \varepsilon_T. \quad (21)$$

The term ε_T in (21) is the resultant matching error from limiting k to 4. As ε_T varies with the number of dominant points, the shape of S_k is not preserved at any step. Increasing c, though computationally more costly, does not necessarily guarantee that $\varepsilon_T = 0$.

Corollary 5: In (17), the dominant points $D = \{d_i\}_{i=0}^{c}$ uniquely define the shape of S_k.

Proof: This follows from Theorem 4 and the discussion above. ■

Next, we examine the uniqueness and shape representation ability of D.

Lemma 6: Let P_x be the centroid of $D = \{d_i\}_{i=0}^{c}$, and G be the centroid of f. As $c \to \infty$, $P_x \to G$ and traces a path unique to the shape of f.

Proof: i) As $c \to \infty$, $P_x \to G$: From Theorem 1, $D = \{d_i\}_{i=0}^{c}$ exists for each c. As the control points of a spline curve are not self-coincident, as $c \to \infty$ D will approximate f and $P_x \to G$.

ii) As $c \to \infty$, the path of P_x is unique to the shape of f: From Corollary 5, for every set of *B*-spline basis functions $M_{i,r}$, and $c > 3$, f is approximated by a unique interpolating spline curve S_r. Let f_A and f_B be two ground truth curves with identical shapes. From Corollary 5, the dominant points of their interpolants will be identical at every resolution c. As centroids are completely determined by point distributions, the centroids of the dominant point distributions of f_A and f_B will be identical. If f_A and f_B are not identical, then, there will exist at least one resolution c, for which the centroids of the dominant point distributions differ. This implies that the centroids of the dominant point distributions of f_A and f_B will follow identical paths as $c \to \infty$ if and only if f_A and f_B have identical shapes. ■

Lemma 6 implies that the path of the centroids of the dominant point distributions of a curve for varying c, is a unique shape signature for the curve.

3.4.3 From dominant points to shape description indices

The result of obtaining the structured splines model of a 3-D object is a cloud of dominant points having a quasi-structure. The relative distribution of the points at each cross-section is a function of the degree of asymmetry at that cross-section. The task is to extract information related to shape (and perhaps symmetry) from the dominant point distribution obtained. Let l be the number of planes of symmetry (or near symmetry) present in the object. The object is decomposed into 2^l sectors along the planes of symmetry if l is even, and into 2^{l+1} sectors along the planes of symmetry and along planes orthogonal to the planes of symmetry if l is odd[4]. Fig. 3.2 shows examples for objects with one and two planes of symmetry. In this study, we determine symmetry using the method of [22].

A. Absolute origin and absolute length

No deformation indices can be calculated for objects for which $l=0$ or $l\to\infty$. If $l>1$ and countable, then the planes of symmetry of the figure would intersect to form a point or line. If the intersection is a point, we term the point the *absolute origin* of the object. If the intersection is a line, the *absolute origin* is the mid-point of the part of the line that is confined within the object. If $l=1$, then the *absolute origin* of the object is the mid-point (usually the centroid of area) of the portion of the plane of symmetry that lies within the object. The *absolute length* of a point is the point's distance from the *absolute origin*.

B. Corresponding segments

Corresponding segments are pairs of segments that are mirror images of each other.

[4] For objects with $l=0$ or $l\to\infty$ (such as circular cylinders or spheres), no decomposition is necessary as they exhibit no computable shape deformation.

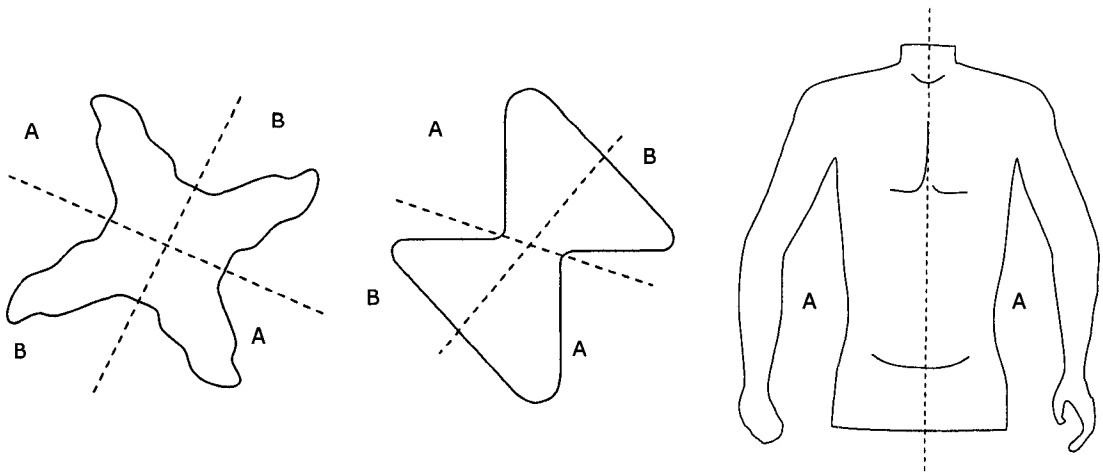

Fig. 3.2: Decomposing an object into symmetric components along its planes of symmetry (or partial symmetry) for the analysis of the distribution of its dominant points.

An object with l axes of symmetry usually has l pairs of corresponding segments. After decomposition along the principal axes, the corresponding segments are numbered as in Fig. 3.2. The dominant point distributions in the segments are aggregated and their centroids computed. The shape of the object can be inferred from the set of *absolute lengths* of the centroids of its segments.

C. Deformation indices

If $l>0$ and countable, then let $G^i=(g_x^i,g_y^i,g_z^i)^T$ and $H^i=(h_x^i,h_y^i,h_z^i)^T$ be the absolute lengths of the centroids of the ith corresponding segments, where $i=\{1, 2, \ldots, l\}$. We define the normalized bend index Ψ_B as:

$$\Psi_B=\frac{1}{\kappa_B}\cdot\sum_i\sqrt{J^z}=\frac{1}{\kappa_B}\cdot\sum_i\sqrt{(g_z^i-h_z^i)^2}\ . \qquad (22)$$

Where the normalization factor κ_B in (22)

$$\kappa_B=l\cdot\max[\max(g_z^i\mid i=1,\ldots,l),\max(h_z^i\mid i=1,\ldots,l)]$$

is the product of the number of corresponding segments by the longest absolute length of a centroid, and $J^z=(g_z^i-h_z^i)^2$. g_z^i and h_z^i are the z components of G^i and H^i respectively.

The equations for the normalized twist and tilt indices, Ψ_T and Ψ_A, are:

$$\Psi_T = \frac{1}{\kappa_T} \cdot \sum_i \sqrt{J^y} = \frac{1}{\kappa_T} \cdot \sum_i \sqrt{(g_y^i - h_y^i)^2}\,, \tag{23}$$

and

$$\Psi_A = \frac{1}{\kappa_A} \cdot \sum_w \sqrt{J^x} = \frac{1}{\kappa_A} \cdot \sum_w \sqrt{(g_x^i - h_x^i)^2}\,. \tag{24}$$

Similarly, κ_T and κ_A in (23) and (24) are defined respectively as:

$$\kappa_T = l \cdot \max[\max(g_y^i \mid i = 1,\ldots,l), \max(h_y^i \mid i = 1,\ldots,l)],$$

$$\kappa_A = l \cdot \max[\max(g_x^i \mid i = 1,\ldots,l), \max(h_x^i \mid i = 1,\ldots,l)].$$

Note that Ψ_B, Ψ_T and Ψ_A are the average rotations of the object in the *x-y*, *x-z* and *y-z* planes respectively.

D. Tracking shape changes

Shape is a relative property of an object. Thus, we can only track shape changes relative to a template shape. This is still the case in situations in which we are not consciously aware of our template[5]. Fig. 3.3 illustrates this.

Given a template object, change in shape is measured relative to the starting shape as a signed difference in *twist*, *bend* and *tilt* indices between the object in consideration and the template object.

3.5 IMPLEMENTATION

In this Section, we describe our particular implementation of the structured splines model. We describe our choice of optimal parameters, shape matching error estimation and method of speeding up the execution of the algorithm.

[5] The most widely used template is the circle in 2-D and the sphere in 3-D. Most shape description methods based on relative length, moments of areas or other symmetry-affected property of objects make this implicit assumption.

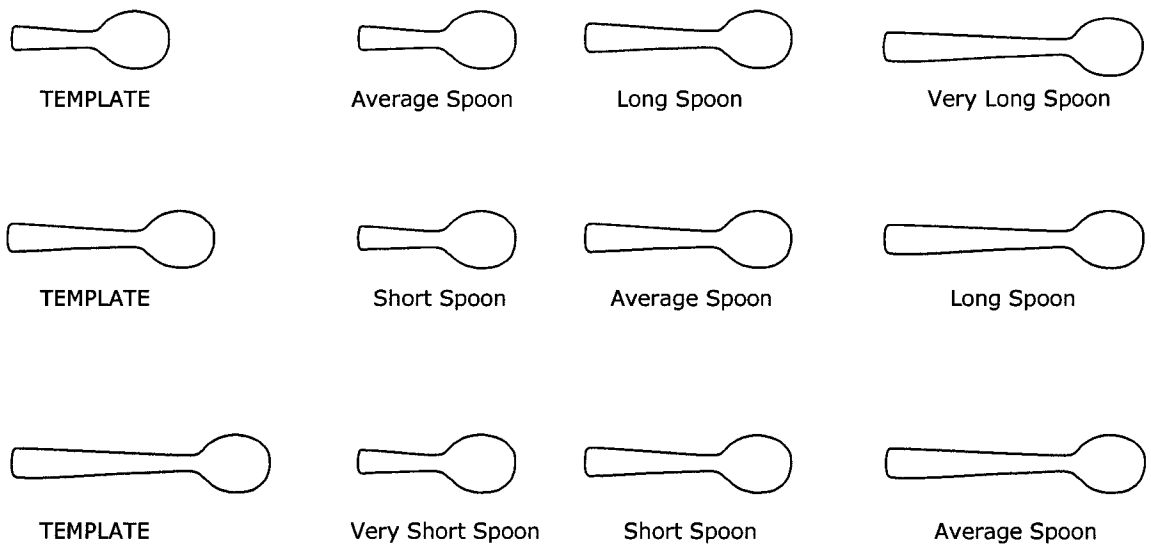

Fig. 3.3: Relative descriptions of spoons. The description of an object is context dependent.

3.5.1 Optimal choice of parameters

The structured splines model is made up a sequence of spline curves that model a structured sequence of cross-sections of the object. For our implementation, we use *B*-spline basis functions and *B*-spline curves. This choice is influenced by the following properties: 1) *B*-spline curves are characterized by their control points, which are a natural set of dominant points; 2) They show invariance under affine transformations; 3) They globally describe the entire curve and yet have local flexibility (depending on the degree) without having to partition the curve into segments.

The choice of parameters such as the order of *B*-spline k, and the number of dominant points to be fitted to the curve points c, was based on the model described in [12]. Fig. 3.4 shows plots of c and k versus normalized shape matching error (Section 3.5.2) and normalized execution time for ten cross-sections of a test object.

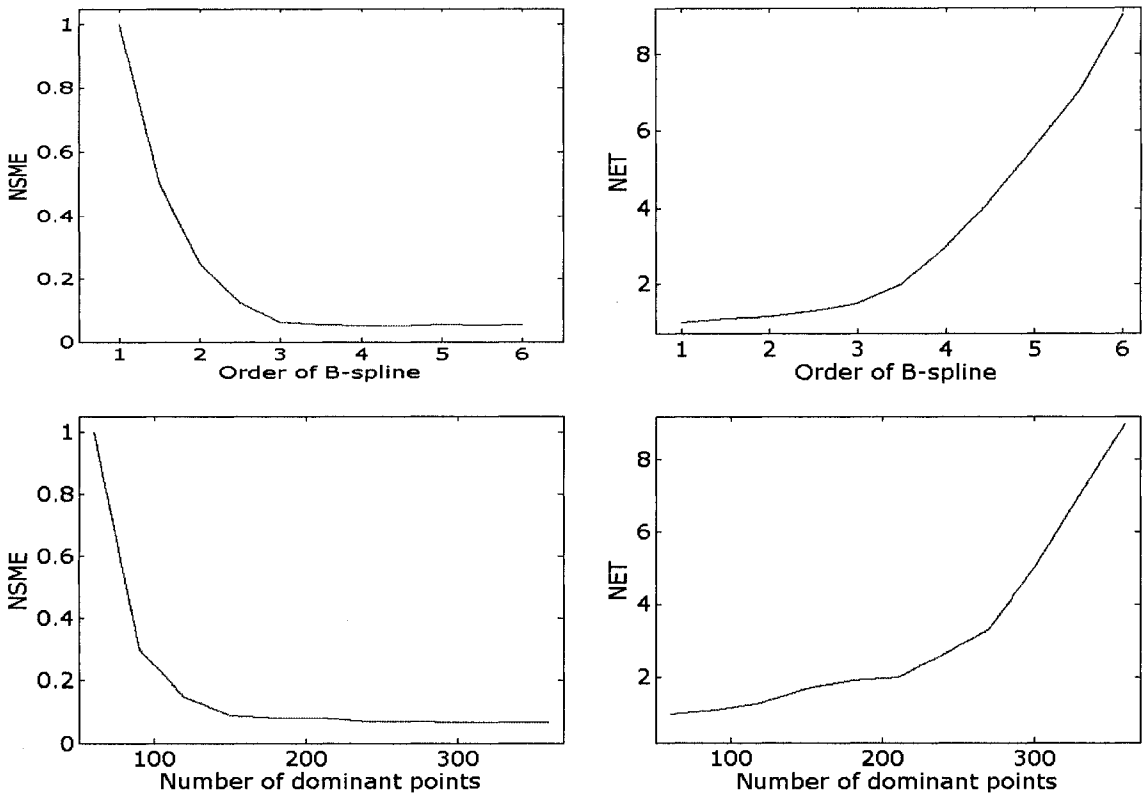

Fig. 3.4: Plots of number of control points and order of *B*-spline versus normalized shape matching error (NSME) and normalized execution time (NET). NSME and NET are normalized with respect to their first values.

3.5.2 Shape matching error estimation

We develop a shape matching error estimation method, based on the shape context [10], for evaluating the fidelity of the match between the interpolated curve S_k and the ground truth curve f. The shape context of a point of p belonging to the contour of an object is a bivariate histogram in a log-polar coordinate system showing the distribution of contour points in the surroundings of p. Let O be an object represented by a set of contour points, $O \equiv \{p_1 \ldots p_N\}$. The shape context of a point $p \in O$ is a vector formally defined as:

$$H_S^O(p) = (h_1(p), h_2(p), \ldots, h_S(p)),$$

where

$$h_s(p) = card\{q \neq p \mid q \in O, (q-p) \in bin(s)\}$$

is the number of contour points in the sth bin $bin(s)$ and S is the total number of histogram bins which divide the image plane into S partitions in a log-polar coordinate system with p as the origin. In this study, we use five intervals for the log distance y and 12 intervals for the polar angle θ, so that S = 60. The maximal diameter[6] of the cross-section serves as the upper bound of the radial distance y on which the shape context is computed, and thus is consistent for all our tests. We randomly select c points in f (out of the possible m) and all the points in S_k and calculate their shape contexts. The shape of f and S_k (λ_f^{SC} and $\lambda_{S_k}^{SC}$) are described respectively, using their sets of shape contexts as:

$$\lambda_f^{SC} \equiv \{H_S^O(p) \mid p \in f\},$$

$$\lambda_{S_k}^{SC} \equiv \{H_S^O(q) \mid q \in S_k\}.$$

As an equal number c, of points is chosen from both curves, the cost of matching a point $p \in f$ to $q \in S_k$ is:

$$\pi_{i,j}^{SC} \equiv \frac{1}{2}\sum_{s=1}^{S}\frac{[h_s(p_i) - h_s(q_j)]^2}{h_s(p_i) + h_s(q_j)}. \qquad (25)$$

A $c \times c$ cost matrix of point-wise dissimilarities is constructed according to (25). The dissimilarity between the shapes representations λ_f^{SC} and $\lambda_{S_k}^{SC}$ of the objects is computed as:

$$\varepsilon^{SC}(\lambda_f^{SC}, \lambda_{S_k}^{SC}) \equiv \frac{1}{c} \cdot \sum_{i=1}^{c} \min\{\pi_{i,j}^{SC} \mid j = 1, \ldots, c\}. \qquad (26)$$

[6] The maximal diameter of an object is the greatest distance between two points in its convex hull.

The metric in (26) is the mean of the minimum costs of matching all pairs of points in the bipartite match of S_k to f. Furthermore, if an ideal approximating curve is obtained, $\varepsilon^{SC} \leq \varepsilon_T$.

3.5.3 Algorithmic speed-Ups

The determination of the interpolated curve S_L involves an iterative procedure of order

$$^{m}\Pi_c = \frac{m!}{c!(m-c)!}.$$

Since each step involves point selection and shape matching error calculation, the computational cost easily escalates making algorithmic speed-ups a necessity. One speed up option limits the candidate points for dominant point selection to points of local maximum curvature. Of the m points on the ground truth curve, if y points are deemed points of high curvature, then the performance improvement is given as

$$I_m(y,c) = \frac{m!}{y!} \cdot \frac{(y-c)!}{(m-c)!}.$$

3.6 RESULTS

3.6.1 Deformable elliptical frustums

We created a deformable model of an elliptical frustum with rotations of 0 – 90^0 in increments of 5^0 in the x-z and x-y planes. Fig. 3.5 shows three elliptical frustum models. For each model, a 4×8×3 structured splines model was created for each frustum. Fig. 3.6 shows the structured splines model of the frustums in Fig. 3.5. Table 3.1 shows the changes in the twist, bend and tilt values obtained from five 180×180×3 structured splines models of the truncated frustums. Each model is used in turn as the template for the other models. This gives a quantitative example

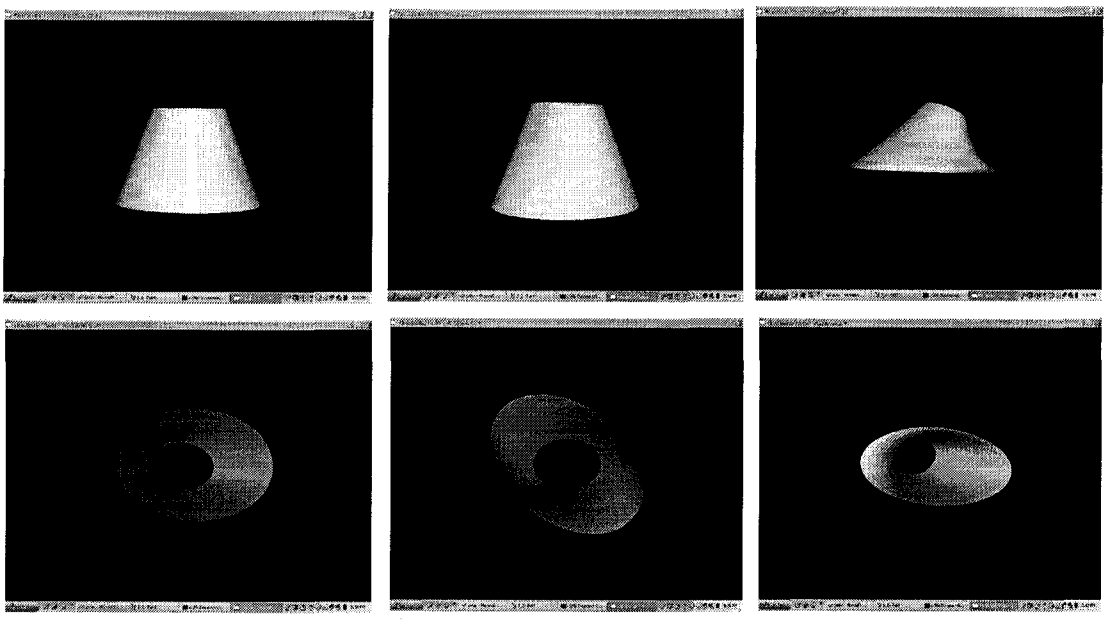

A B C

Fig. 3.5: Three frustums used to illustrate the descriptive power of shape contexts. A has no x-z or x-y rotations, B has 30^0 x-z rotation but no x-y rotation, while C has 30^0 x-z rotation and 30^0 x-y rotation.

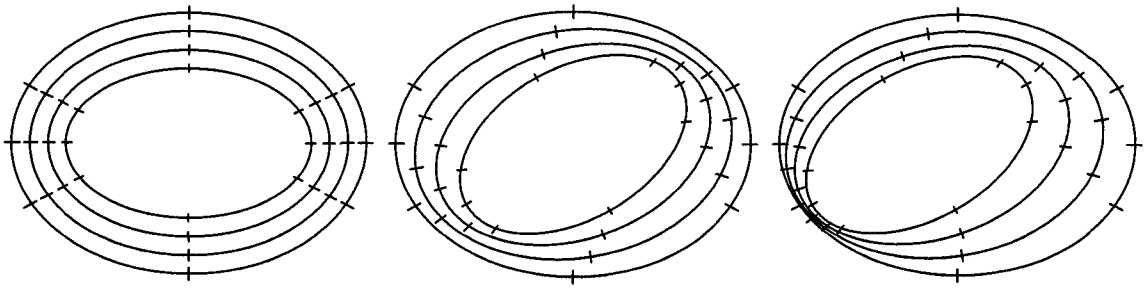

A B C

Fig. 3.6: Top-view of a 4×8×3 structured splines models of the frustums. Though a rough model is shown, the differences (transformations applied to the frustums) are very apparent.

of the idea of that shape description is relative.

3.6.2 Range images of the human torso

To demonstrate a practical application of structured splines modelling, we model range images of the back surface of patients who have scoliosis, a deformity of the

Table 3.1: Comparison of the percent change in (*twist*, *bend*, *tilt*) values obtained for six frustums. Each frustum was used alternately as the template object for comparison.

	Model 1	Model 2	Model 3	Model 4	Model 5	Model 6
Model 1	00,00,00					
Model 2	15,00,07	00,00,00				
Model 3	00,15,07	15,15,15	00,00,00			
Model 4	15,15,15	00,15,07	15,00,07	00,00,00		
Model 5	30,15,22	15,15,15	30,00,15	15,00,07	00,00,00	
Model 6	15,30,22	00,30,15	15,15,15	00,15,07	15,15,15	00,00,00

Model 1: x-z = 0^0; x-y = 0^0. Model 2: x-z = 30^0; x-y = 0^0. Model 3: x-z = 0^0; x-y = 30^0.

Model 4: x-z = 30^0; x-y = 30^0. Model 5: x-z = 60^0; x-y = 30^0. Model 6: x-z = 30^0; x-y = 60^0.

spine that causes visible torso asymmetry [23]. Scoliosis affects up to four percent of adolescents in North America, but only a small fraction of those affected will need clinical treatment or monitoring [24]. Range images of the torso are used in monitoring the effect of scoliosis on the shape of the torso. Fig. 3.7 shows back torso pictures of three scoliosis patients who have a prominent *twist* or *bend* deformity. Fig. 3.8 shows a cascaded top view of the 4×4×3 structured splines models of the range scans corresponding to the back torso pictures of Fig. 3.7.

A visual representation of the obtained indices can be captured using a *status diagram* (Fig. 3.9). To improve the descriptiveness of the status diagram, the back image is first divided into two halves along its symmetry line. Each half is further divided into three sections. The centroids of the dominant points in each section is computed and plotted to give a visual representation of the back torso deformity.

3.7 CONCLUSIONS

This chapter considered the problem of quantifying the shape of a deformable 3-D object with a view to tracking its shape changes over time and comparing its shape to that of similar objects. An intuitive solution that relied on perceptible surface

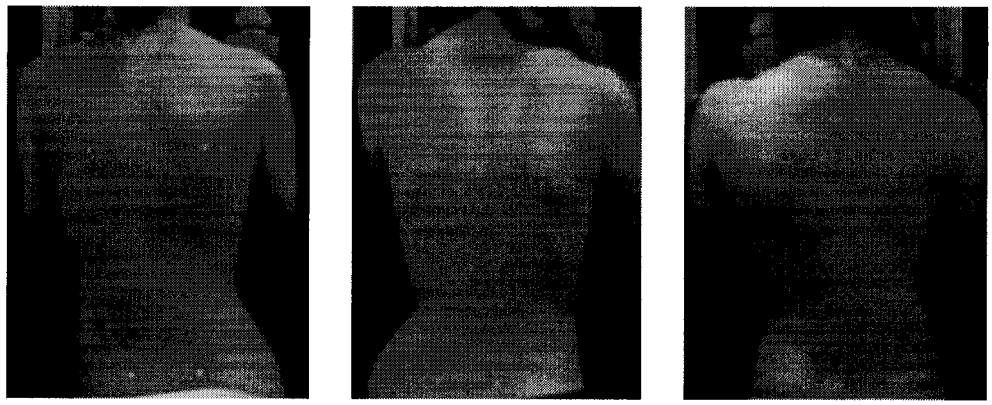

A B C

Fig. 3.7: Back torso images of scoliosis patients who have prominent deformation components. A: Left Tilt; B: Right Tilt; and C: Left Twist.

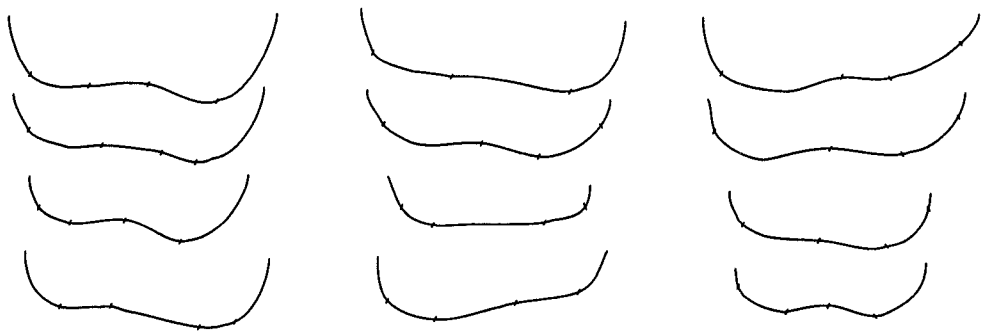

A B C

Fig. 3.8: Cascaded top-view of the 4×8×3 structured splines models of the range images of the back whose pictures are shown in Fig. 3.7. The differences between the three structured splines models are also apparent at this low resolution.

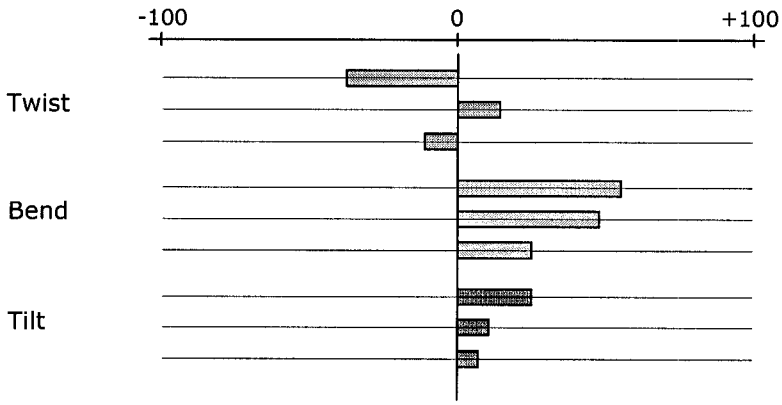

Fig. 3.9: A nine bar-status diagram of the back torso of a scoliosis patient. The bar lengths correspond to absolute index values of the deformity indices while the placements of the bars relative to the center line indicate the index sign. Right is positive and left is negative.

features, curvature and symmetry, was proposed for the problem. The solution involved structured splines modelling of the deformable 3-D object. It involved three stages: First, the 3-D object's surface was modelled as a structured sequence of cross-sections and the sequence thus obtained was shown to be invariant to positioning and affine transformations; Second, feature points (dominant points) that describe local curvature of the deformable object were extracted from each of the structured cross-sections obtained in the first stage; Third, the aggregated set of dominant points obtained is used to develop a multi-axial shape vector (comprising of *twist*, *bend* and *tilt* components) which in turn is used to quantify and track the shape of the deformable 3-D objects.

The use of dominant points of a structured sequence of *B*-spline curves ensured a rich representation as most of the information present in a shape is concentrated at the dominant points [1]. Though dominant points have been used for several applications, they have not been used to quantify the shape of 3-D objects.

The main contributions of this chapter were a technique for obtaining a structured sequence of cross-sections of deformable 3-D objects, a minimum error estimation technique for interim shape matching during feature point selection, based on the shape context technique [2], a multi-axial shape vector for quantifying shape taking into account symmetries and near symmetries and a technique for classifying and tracking 3-D shape. In addition, this study built on curvature based shape description, in non-trivial ways, to address the problem of 3-D shape quantification and tracking of deformable objects.

REFERENCES

1. F. Attneave, 'Some Informational Aspects of Visual Perception,' *Psychology Review*, vol. 61, no. 3, pp. 183-193, 1954.
2. S. Belongie, J. Malik, and J. Puzicha, 'Shape matching and object recognition using shape contexts,' *IEEE Transactions on Pattern Analysis and Machine Intelligence*, vol. 24, no. 4,

pp. 509–22, 2002.

3. S. Loncaric, 'A survey of shape analysis techniques,' *Pattern Recognition*, vol. 31, no. 8, pp. 983–1001, 1998.
4. M. Hagedoorn, 'Pattern Matching Using Similarity Measures,' PhD thesis, Universiteit Utrecht, 2000.
5. T. M. Cronin, 'A boundary concavity code to support dominant point detection,' *Pattern Recognition Letters,* vol. 20, no. 6, pp. 617-634, 1999.
6. F. S. Cohen and J. Wang, 'Part I: Modeling image curves using invariant 3-D object curve models – a path to 3-D recognition and shape estimation from image contours,' *IEEE Transactions on Pattern Analysis and Machine Intelligence*, vol. 16, no. 1, pp. 1-12, 1994.
7. Y. Zhu, L. D. Seneviratne, 'On the recognition and location of partially occluded objects,' *Journal of Intelligent & Robotic Systems,* vol. 25, no. 2, pp. 133-151, 1999.
8. A. Goshtaby, 'Description and Discrimination of Planar Shapes Using Shape Matrix,' *IEEE Transactions on Pattern Analysis and Machine Intelligence*, vol. 7, pp. 738-743, Nov. 1985.
9. H. Blum, 'A Transformation for Extracting New Descriptors of Shape,' *Models for the Perception of Speech and Visual Forms*, *Whaten-Dunn, ed.* pp. 362-380, MIT Press, 1967.
10. S.O. Belkasim, M. Shridhar, and M Ahmadi, 'Pattern Recognition with Moment Invariants: A Comparative Study and New Results,' *Pattern Recognition*, vol. 24, pp. 1117-1138, 1991.
11. R.J. Prokop and A.P. Reeves, 'A Survey of Moment-Based Techniques for Unoccluded Object Representation and Recognition,' *CVGIP: Graphical Models and Image Processing*, vol. 54, pp. 438-460, 1992.
12. F. Mokhtarian and A. Mackworth, 'A Theory of Multiscale Curvature-Based Shape Representation for Planar Curves,' *IEEE Transactions on Pattern Analysis and Machine Intelligence*, vol. 14, no. 8, pp. 789-805, 1992.
13. Y. P. Wang, S. L. Lee, K. Toraichi, 'Multiscale curvature-based shape representation using B-spline wavelets,' *IEEE Transactions on Image Processing,* vol. 8, no. 11, pp. 1586-1592, 1999.
14. C. Grigorescu, and N. Petkov, 'Distance Sets for Shape Filters and Shape Recognition,' *IEEE Transactions on Image Processing*, vol. 12, no. 10, pp. 1274-1286, October 2003.
15. C. Teh and R. T. Chin, 'On the Detection of Dominant Points on Digital Curves,' *IEEE Transactions on Pattern Analysis and Machine Intelligence*, vol. 11, no. 8, pp. 859-872, 1989.
16. I. J. Schoenberg, 'Contributions to the problem of approximation of equidistant data by analytic functions. Part A–on the problem of smoothing or graduation. A first class of analytic approximation formulae,' *Quarterly Applied Mathematics*, vol. IV, no. 1, pp. 45-99, 1946.
17. I. J. Schoenberg, 'Contributions to the problem of approximation of equidistant data by

analytic functions. Part B–on the problem of osculatory interpolation. A second class of analytic approximation formulae,' *Quarterly Applied Mathematics*, vol. IV, no. 2, pp. 112-141, 1946.

18. E. Cohen, R. F. Riesenfeld, G. Elber, *Geometric Modeling with Splines: An Introduction*, A K Peters, Natick, Massachusetts, 2001.
19. E. T. Whittaker, 'On the functions which are represented by the expansions of interpolation-theory,' in *Proceedings of the Royal Society of Edinburgh*, vol. 35, pp. 181-194, 1915.
20. E. Meijering, 'A chronology of interpolation: from ancient astronomy to modern signal and image processing,' *Proceedings of the IEEE*, vol. 90, no. 3, 2002.
21. C. E. Shannon, 'A mathematical theory of communication,' *Bell System Technology Journal*, vol. 27, pp. 379-423, 1948.
22. G. Marola, 'On the detection of axes of symmetry of symmetric and almost symmetric planar images,' *IEEE Transactions on Pattern Analysis and Machine Intelligence*, vol. 11, no. 1, 1989.
23. V. J. Raso, E. Lou, D. L. Hill, J. K. Mahood, M. J. Moreau, N. G. Durdle, 'Trunk distortion in adolescent idiopathic scoliosis,' *Journal of Pediatric Orthopedics*, vol. 18, no. 3, pp. 22-26, 1998.
24. P. O. Ajemba, N. G. Durdle, D. L. Hill, and V. J. Raso, 'A torso imaging system for quantifying the deformity associated with scoliosis,' *IEEE Transactions on Instrumentation and Measurements,* vol. 56, no. 5, October 2007.

CHAPTER 4

STRUCTURED SPLINES MODELS: APPLICATION TO QUANTIFYING TORSO DEFORMITY IN SCOLIOSIS [N]

4.1 INTRODUCTION

This chapter proposes a solution to the problem of quantifying torso deformity in scoliosis and tracking changes in torso shape over time. This is an example of the broader class of problems in computer vision and shape analysis that deals with deformable 3-D shape description and matching. We approach the problem from the point of view of scoliosis, a deformity of the spine that results in visible torso deformity. Readers are referred to Chapter 2 for a discourse on scoliosis. Fig. 4.1 shows back torso pictures of a patient with progressive scoliosis taken in six-month intervals. We require our solution to torso deformity classification and tracking to make use of range scans of the torso (the most common form of acquisition [1]), be intuitive to medical practitioners involved in the chain of care of the scoliosis patients and be based on deformity features like curvature and symmetry.

4.1.1 Overview

Our previous work [2] proposed the use of dominant points obtained from structured splines models of deformable 3-D objects for quantifying their shape and symmetry. In this chapter, we apply the method to the human torso for the assessment, quantification and tracking of torso deformity. Three indices of torso shape deformity were developed. The indices were *twist*, *bend* and *tilt* corresponding to the average

[N] A version of this chapter has been submitted for publication. P. O. Ajemba, N. G. Durdle, and V. J. Raso, 'Quantifying and tracking torso deformity using dominant points of structured splines models,' *IEEE Transactions on Medical Imaging*, 2007.

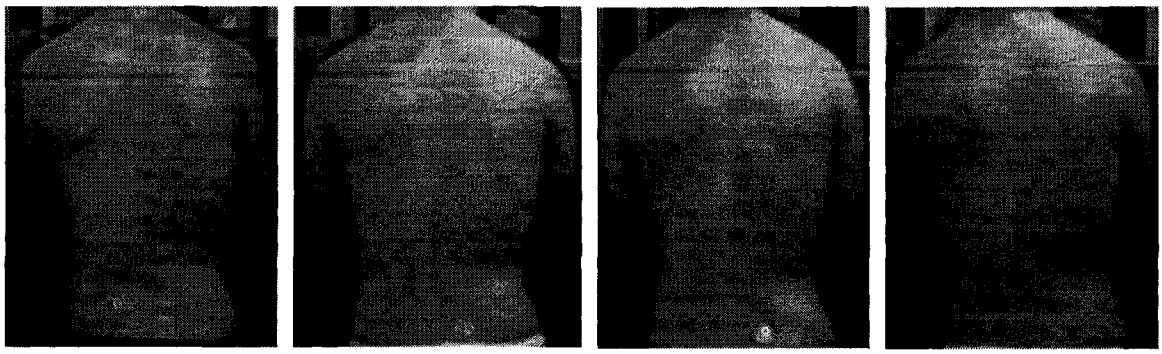

Fig. 4.1: Back surface images of a scoliosis patient taken at six-month intervals.

torso rotation in the coronal (top), lateral (side), and posterior-anterior (front-back) views respectively. We present a classification system based on the said indices and a torso deformity tracking system for scoliosis management. We also present improvements to the techniques for obtaining structured splines models and the indices of torso shape deformity from torso images. Finally, this work builds on the theory of dominant points of structured splines models to address the problem of assessing, classifying and tracking scoliosis deformity.

4.2 STRUCTURED SPLINES MODELS

4.2.1 Model description

In concrete terms: Given a 3-D object O made up of a collection of say $M \times N$ points, our task is to extract a structured sequence of $h \times c$ 3-D points that are the dominant points of the object's surface. That is,

$$O_{M \times N} \rightarrow O_{h,c}(t). \qquad (1)$$

First we decompose the object into a structured sequence of cross-sections using a technique based on volume constancy, an invariant of closed 3-D objects[1]. Next, we

[1] Volume constancy means that sectioning an object into a number of equal volume segments with respect to two or more fixed points on its surface results in a consistent set of cross-sections.

obtain the dominant points of each cross-section using *B*-spline basis functions and aggregate them to create the structured splines model of O.

A. Volume decomposition

The following definition sets up our volume decomposition technique.

Definition 1: For a simple closed 3-D surface O with a start point T and an end point E, a *regular set of cross-sections* is one whose members divide O into a number of equal volume segments that are invariant to orientation and scale.

The planes of a regular set of cross-sections need not be parallel to each other but cannot intersect within the volume of the surface. In addition, the regular set of cross-sections is unique and invariant to affine transformations [2]. Our first step then reduces to obtaining a regular set of cross-sections from the 3-D object. This requires computing a centroid line for the object.

Definition 2: For a simple closed 3-D surface O with a start point T and an end point E, a *centroid line* originates at T and ends at E and joins the centroids of the cross-sections of an infinite-sized regular set of cross-sections of O.

B. Cross-section modelling

Let two sets of real numbers called a breakpoint vector set and a multiplicity vector set be given respectively as $U = \{u_i\}_{i=0}^{s}$ and $M = \{m_i\}_{i=0}^{s}$. We define a set of numbers called a knot vector set as $T = \{t_j\}$, where $m_i = card\{j : t_j = u_i\}$, such that $t_0 \le t_1 \le \cdots \le t_N$. For $k = 0,\ldots,N$, and $i = 0,\ldots,N-k$. The ith *B*-spline basis function of order k is defined for $k = 0$ as:

$$\alpha_{i,0}(t) = \begin{cases} 1 & t_i \le t < t_{i+1} \\ 0 & otherwise \end{cases}, \qquad (2a)$$

and for $k>0$ as:

$$\alpha_{i,k}(t)=\begin{cases}\dfrac{(t-t_i)}{t_{i+k}-t_i}\alpha_{i,k-1}(t)+\dfrac{(t_{i+1+k}-t)}{t_{i+1+k}-t_{i+1}}\alpha_{i+1,k-1}(t), & t_i<t_{i+1+k}\\ 0 & otherwise\end{cases}. \quad (2b)$$

Let $P=\{p_i\}_{i=0}^{N}$ be a sequence of 3-D points. A *B*-spline curve based on the *B*-spline basis functions (2a) and (2b) is defined as:

$$S_k(t)=\sum_{i=-\infty}^{\infty}p_i\cdot\alpha_{i,k}(t-i)=\sum_{i=0}^{N}p_i\cdot\alpha_{i,k}(t-i). \quad (3)$$

It can be shown [2] that for a curve f and $c\in Z$, $c\geq 3$, there exists a set of points $D=\{d_i\}_{i=0}^{c}$ which when interpolated using (2a) or (2b) (as in (3)) yields an interpolant S_k of f for which in the ideal case[2]

$$\lim_{i\to c}\| S_k-f\|_{k^\infty}=0. \quad (4)$$

The set of points D are called the dominant points of f. D uniquely defines the shape of f.

C. Structured splines models

The structured splines model of O is the set of dominant points of the structured sequence of curves given by:

$$O_{h,c}(t)=\bigcup_{j=0}^{h-1}S_L(t)=\bigcup_{j=0}^{h-1}\sum_{i=0}^{c-1}p_i\cdot\alpha_{i,k}(t-i). \quad (5)$$

For a given start point T and end point E, the structured splines model of O is formally defined as follows:

Definition 3: Let each of the h regular cross-sections of a simple closed 3-D object O consisting of a cloud of $M\times N$ points be modeled by h interpolating

[2] In actual cases, a small matching error threshold ε_T is expected rather than zero.

curves S_k using *B*-spline basis functions $\alpha_{i,k} \in C^0$ and c dominant points per cross-section. The $h \times c$ matrix formed by the structured sequence of dominant points is the structured splines model of O of order $h \times c \times k$.

This definition implies that an $h \times c \times k$ order structured splines model of a simple closed 3-D object O is unique and captures the shape of the surface for $h, c = 3, \ldots, \infty$. Thus, the shapes of different 3-D objects can be compared by comparing their structured splines models.

4.2.2 Selection of parameters

The choice of parameters, such as the order of the spline k and the number of control points to be fitted to the curve points c, was based on a selection routine described in [3]. Fig. 4.2 shows plots of c and k versus normalized shape matching error and normalized execution time for ten evenly spaced cross-sections of an average *normal* torso[3] without scoliosis.

4.2.3 Shape matching error estimation

There are a plethora of variables associated with *B*-spline modelling. During model development, it is useful to continuously assess the match between the interpolated curve S_k to f. Our error estimation method is based on the shape context [4]. We use five intervals for the log-distance r and twelve intervals for the polar angle θ. The maximal diameter[4] of the cross-section serves as the upper bound of the radial distance r on which the shape context is computed, and thus is consistent for all our tests. We blindly select c out of m points in f and all the points in S_k and

[3] The average *normal* torso was obtained by averaging the 3-D torso images of ten volunteers who had no scoliosis and whose average demographics matched the average of our scoliosis dataset.

[4] The maximal diameter of an object is the greatest distance between two points in its convex hull.

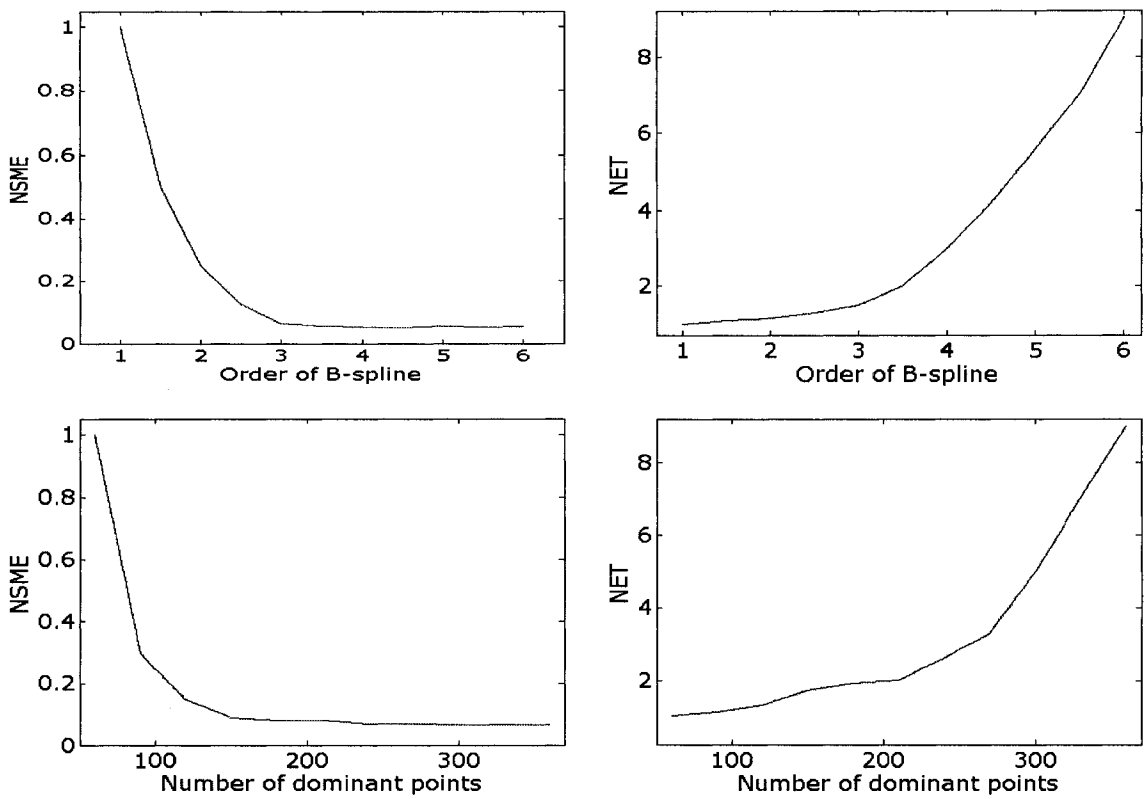

Fig. 4.2: Plots of the number of control points and the order of *B*-spline versus the normalized shape matching error (NSME) and the normalized execution time (NET). The NSME and the NET are normalized with respect to their first values.

calculate their shape contexts. The shape of f and S_k (λ_f^{SC} and $\lambda_{S_k}^{SC}$) are described respectively, using their sets of shape contexts as:

$$\lambda_f^{SC} \equiv \{H_S^O(p) \mid p \in f\},$$

$$\lambda_{S_k}^{SC} \equiv \{H_S^O(q) \mid q \in S_k\}.$$

As an equal number c, of points is chosen from both curves, the cost of matching a point $p \in f$ to $q \in S_k$ is:

$$\pi_{i,j}^{SC} \equiv \frac{1}{2}\sum_{s=1}^{S}\frac{[h_s(p_i)-h_s(q_j)]^2}{h_s(p_i)+h_s(q_j)}. \qquad (6)$$

A $c \times c$ cost matrix of point-wise dissimilarities is constructed using (6). The dissimilarity between the shape representations (λ_f^{SC} and $\lambda_{S_k}^{SC}$) of the objects is computed as:

$$\varepsilon^{SC}(\lambda_f^{SC}, \lambda_{S_k}^{SC}) \equiv \frac{1}{c} \cdot \sum_{i=1}^{c} \min\{\pi_{i,j}^{SC} \mid j = 1, \ldots, c\} . \qquad (7)$$

The metric in (7) is the mean of the minimum costs of matching all pairs of points in the bipartite match of S_k to f. Furthermore, if an ideal approximating curve is obtained, then $\varepsilon^{SC} \leq \varepsilon_T$.

4.2.4 Computational improvement

Let m be the original number of points. For a $h \times c \times k$ structured splines model, the determination of all the c dominant points on the h interpolated curves $\{S_k^i\}_{i=0}^{h}$ involves an iterative procedure of the order

$${}^{m}\Pi_{h,c} = h \cdot \frac{m!}{c!(m-c)!} .$$

Algorithmic speed ups are necessary as each step also involves shape matching error calculation. A number of speed-up options for computational improvement are possible. In this section, we present three of the more robust options.

A. Location-based limiting

This is the simplest method we describe. It entails limiting the pool of candidate points for dominant point selection to points that lie in some pre-defined locale of the curve. Of the m points on f, let y be the number of points selected. The performance improvement is given as

$$I_m \approx \frac{m}{y}.$$

A simple implementation of this is to select every two or three points and discard the rest. That would yield performance improvement values of 2 and 3 respectively. A random selection of points can also be used.

B. Curvature-based limiting

This entails limiting the pool of candidate points for dominant point selection to points of local maximal curvature. To determine these, the curvature of each point is determined from points around it using curvature estimation methods such as 1-curvature [12]. Of the m points on f, if y points are deemed points of local maximal curvature, then the performance improvement obtained is given as

$$I_m \approx \frac{m!}{y!} \cdot \frac{(y-c)!}{(m-c)!}.$$

C. Block-based limiting

This entails limiting the computational complexity of the search by first dividing the available point set into *blocks* of smaller sized sets before applying a secondary limiting operation. Position and curvature-based limiting operations can be used as the secondary operation. Let the m points on f be divided into w partitions ($m \oplus w = 0$, where $\oplus$ is the modulo operation). Each partition would then yield c/w dominant points ($c \oplus w = 0$). The performance improvement achieved is

$$I_m = \frac{m!}{c!} \cdot \frac{(c/w)!}{(m/w)!} \cdot \frac{((m-c)/w)!}{w(m-c)!} \cdot I_S. \qquad (8)$$

Where I_S is the improvement obtained from the secondary method.

4.3 DEFORMATION INDICES

4.3.1 Deformation parameters

Torso deformity due to scoliosis is complex and wide ranging, and can be decomposed into three orthogonal components; *bend*, *twist* and *tilt*. *Bend* is a measure of torso rotation in the lateral (side) view. *Twist* is a measure of torso axial rotation in the coronal (top) view, while *tilt* is a measure of torso rotation in the posterior-anterior (back-front) view. Fig. 4.3 shows the pictures of the back of volunteers whose torso deformity has a prominent twist or bend component. Fig. 4.4 shows a cascaded top view of the 4×4×3 structured splines models of the range scans corresponding to the back torso pictures of Fig. 4.3.

Tilt deformity may result in an uneven hip height, shoulder tilt and waist crease. It also results in a misalignment of the center of the neck with the middle of the waist. *Twist* deformity usually results in prominent and uneven collarbones and a relative shift in the locations of the shoulders and hips. *Bend* usually results in a forward or backward stoop. These three components form an orthogonal basis vector in 3-axis deformity space but do not necessarily correspond to specific aspects of spinal deformity as torso deformity is related but separate from spinal deformity [5], [6].

The result of structured splines modelling is a collection of dominant points having a quasi-structure. The distribution of the points at each cross-section depends on the torso asymmetry present at that cross-section. The task is to extract information related to shape and symmetry from the dominant point distribution obtained. The human torso ideally has one plane of (near) symmetry as shown in Fig. 4.5.

To aggregate the dominant points, we divide the torso into quadrants in the coronal plane view: Front Right, Front Left, Back Right and Back Left (Fig. 4.5). Full torso images contain all four quadrants whereas back torso images contain only the back quadrants. As torso deformity is mostly due to an absence of symmetry, we

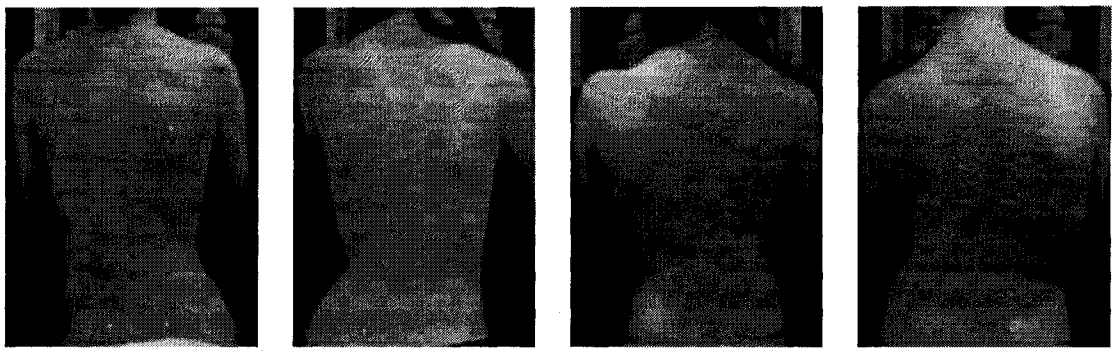

A B C D

Fig. 4.3: Back torso images of scoliosis patients who have prominent deformation components. A: Left Tilt; B: Right Tilt; C: Left Twist; and D: Right Twist.

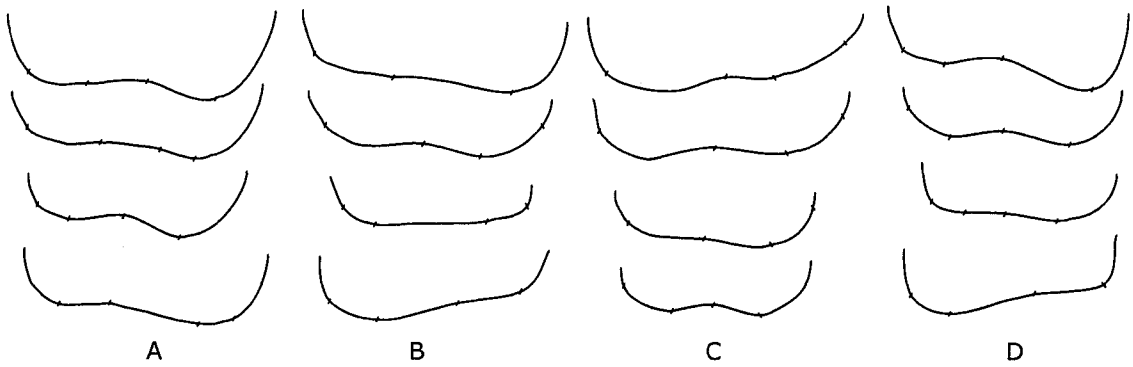

A B C D

Fig. 4.4: Cascaded top-view of the 4×8×3 structured splines models of the back surfaces shown in Fig. 6.3. The differences in shape are apparent at this low resolution.

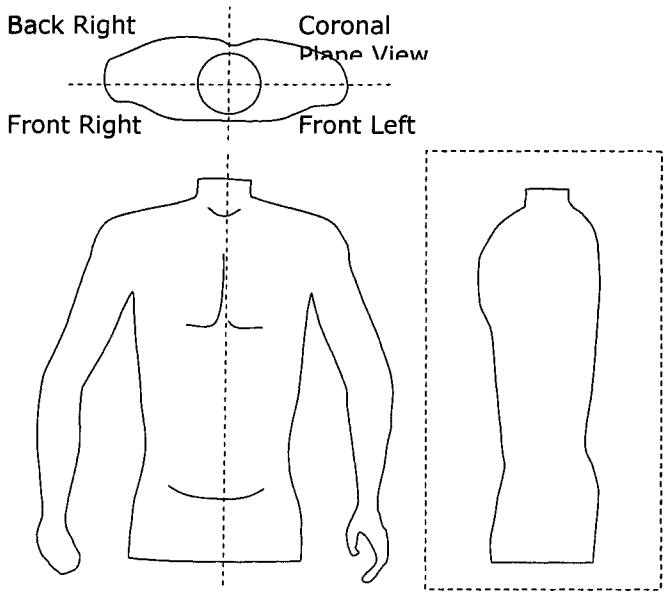

Fig. 4.5: The plane of symmetry of the torso with the plane of symmetry in dashed lines.

estimate the deformation indices from the relative locations of the centroids of the dominant point distributions in each quadrant. We then compare the corresponding x, y and z components of the centroids of the left and right quadrants at the back and the corresponding quadrants at the front if they are available.

4.3.2 Dominant point aggregation

We utilized four options for aggregating the dominant point distribution: 1) Dividing each torso quadrant into a number of horizontal segments and then aggregating the dominant points that fall within each segment; 2) Clustering the entire distribution of dominant points using k-means classifiers; 3) Dividing the dominant points equally into a number of horizontal sections of the quadrants before clustering; and 4) Dividing the quadrants into horizontal segments before computing the dominant points, leading to different criteria for dominant point selection for each segment. Table 4.1 summarizes the properties of the four methods.

Let w be the number of sections that each quadrant is divided into. This yields an overall number of $4w$ sections for a full torso scan, and $2w$ for a back torso scan. To determine the optimal value of w, we calculate the percentage improvement in shape discrimination and the normalized increase in computational cost[5] for values of $w>1$. The results obtained (Fig. 4.6) show that $w=3$ is optimal.

4.3.3 Index calculation

The *absolute origin* of an object is the mid-point (usually the centroid of area) of the portion of the plane of symmetry that lies within the object. The *absolute length* of a point is the point's distance from the *absolute origin*.

[5] The shape discrimination at a is the absolute difference between the shape index values (see next section) at $w=a$ and the shape index values at $w=1$. The normalized increase in computational cost (execution time) at a is the ratio of the computational cost at $w=a$ to the computational cost at $w=1$.

Table 4.1: Attribute of dominant point aggregation methods

Attribute*	Method 1	Method 2	Method 3	Method 4
Number of dominant points	Variable	Variable	Fixed	Fixed
Location of sections	Fixed	Variable	Variable	Fixed
Bounds for dominant points	Global	Global	Global	Local

*Method 1: Dividing each torso quadrant into a number of horizontal segments before aggregating the dominant points in each segment. Method 2: Clustering the distribution using k-means. 3: Dividing the dominant points equally into a number of horizontal quadrants before clustering; and 4: Dividing the quadrants into horizontal segments before computing the dominant points..

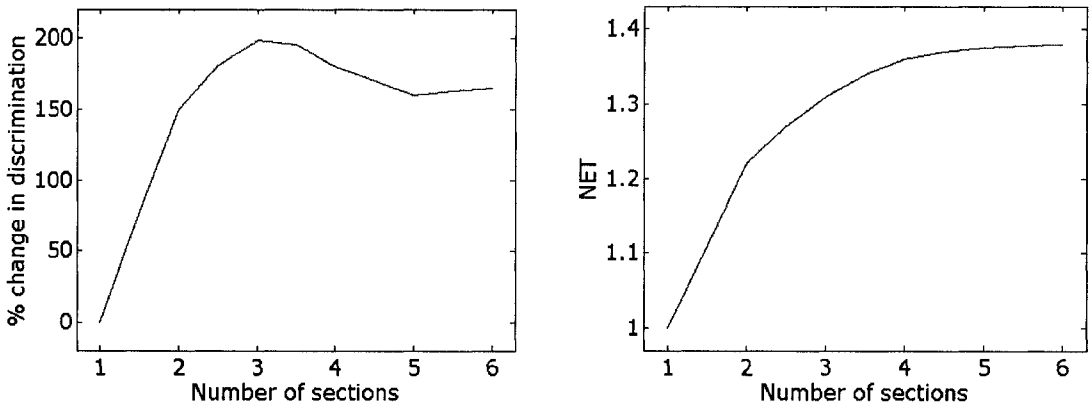

Fig. 4.6: Plots of number of sections w versus % change in index of shape discrimination and normalized execution time (NET) for $n=3$, $c=180$ and $h=180$.

Let $G^i=(g_x^i,g_y^i,g_z^i)^T$ and $H^i=(h_x^i,h_y^i,h_z^i)^T$ be the absolute lengths of the centroids of the ith left and right segments respectively, where $i=\{1,\ 2,\ \ldots,w\}$. We define the normalized bend index Ψ_B as:

$$\Psi_B=\frac{1}{\kappa_B}\cdot\sum_i\sqrt{J^z}=\frac{1}{\kappa_B}\cdot\sum_i\sqrt{(g_z^i-h_z^i)^2}\ . \qquad (9)$$

Where the normalization factor κ_B in (9)

$$\kappa_B=w\cdot\max[\max(g_z^i\mid i=1,\ldots,w),\max(h_z^i\mid i=1,\ldots,w)]$$

is the product of the number of corresponding segments by the longest absolute

length of a centroid. The corresponding equations for the normalized twist index Ψ_T and the normalized tilt index Ψ_A are:

$$\Psi_T = \frac{1}{\kappa_T} \cdot \sum_i \sqrt{J^y} = \frac{1}{\kappa_T} \cdot \sum_i \sqrt{(g_y^i - h_y^i)^2}\,, \tag{10}$$

and

$$\Psi_A = \frac{1}{\kappa_A} \cdot \sum_w \sqrt{J^x} = \frac{1}{\kappa_A} \cdot \sum_w \sqrt{(g_x^i - h_x^i)^2}\,. \tag{11}$$

Similarly, κ_T and κ_A in (10) and (11) are defined respectively as:

$$\kappa_T = w \cdot \max[\max(g_y^i \mid i = 1,\ldots,w), \max(h_y^i \mid i = 1,\ldots,w)]\,,$$

$$\kappa_A = w \cdot \max[\max(g_x^i \mid i = 1,\ldots,w), \max(h_x^i \mid i = 1,\ldots,w)]\,.$$

Note that Ψ_B, Ψ_T and Ψ_A are the average rotations of the object in the *x-y*, *x-z* and *y-z* planes respectively.

Alternate formulations for J^z, J^y and J^x are:

1) Mean absolute difference: $J^z = \mid g_z^i - h_z^i \mid$, $J^y = \mid g_y^i - h_y^i \mid$ and $J^x = \mid g_x^i - h_x^i \mid$, and

2) Mean cube difference: $J^z = (g_z^i - h_z^i)^3$, $J^y = (g_y^i - h_y^i)^3$ and $J^x = (g_x^i - h_x^i)^3$.

4.4 CLASSIFICATION AND TRACKING OF TORSO DEFORMITY

4.4.1 Deformation classes

We grouped torso deformity caused by scoliosis into nine classes based on the signs of the deformity indices (Table 4.2). Class zero corresponds to no deformity. For our purposes, unless a patient shows a zero deformity score in all three categories, zero is considered a positive number. For instance, a patient with positive *twist* and *bend* scores and a zero *tilt* score will be placed in class one. Fig. 4.7 shows examples of each class.

Table 4.2: Categorization of torso deformity based on *twist*, *bend* and *tilt* indices

Class	*Bend*	*Tilt*	*Twist*
Zero	Zero	Zero	Zero
One	Positive	Positive	Positive
Two	Positive	Positive	Negative
Three	Positive	Negative	Positive
Four	Positive	Negative	Negative
Five	Negative	Positive	Positive
Six	Negative	Positive	Negative
Seven	Negative	Negative	Positive
Eight	Negative	Negative	Negative

Class Zero corresponds to no deformity. Positive deformity is rotation to the right or front; Negative deformity is rotation to the left or back.

4.4.2 Status diagrams

Status diagrams help to visualize the *twist*, *bend* and *tilt* scores and present a snap shot of the deformity scenario. To enhance their utility, the front and back are separated. Horizontal torso segments are represented by separate bars (Fig. 4.8).

4.4.3 Status charts

These are derived from the status diagrams and show the deformity profile of the scoliosis patient over several clinical visits. Fig. 4.9 shows the status chart of a scoliosis patient. In addition to the deformity indices, status charts also record *significant* change in index values and class changes. The status diagram in Fig. 4.8 is the October 2004 entry in the status chart of Fig. 4.9. The clinician using the system defines what constitutes a *significant* change in index values. In our case, a significant change in index values was a change of up to 10 points. The occurrence of a significant change may prompt a more detailed look at the patient's file.

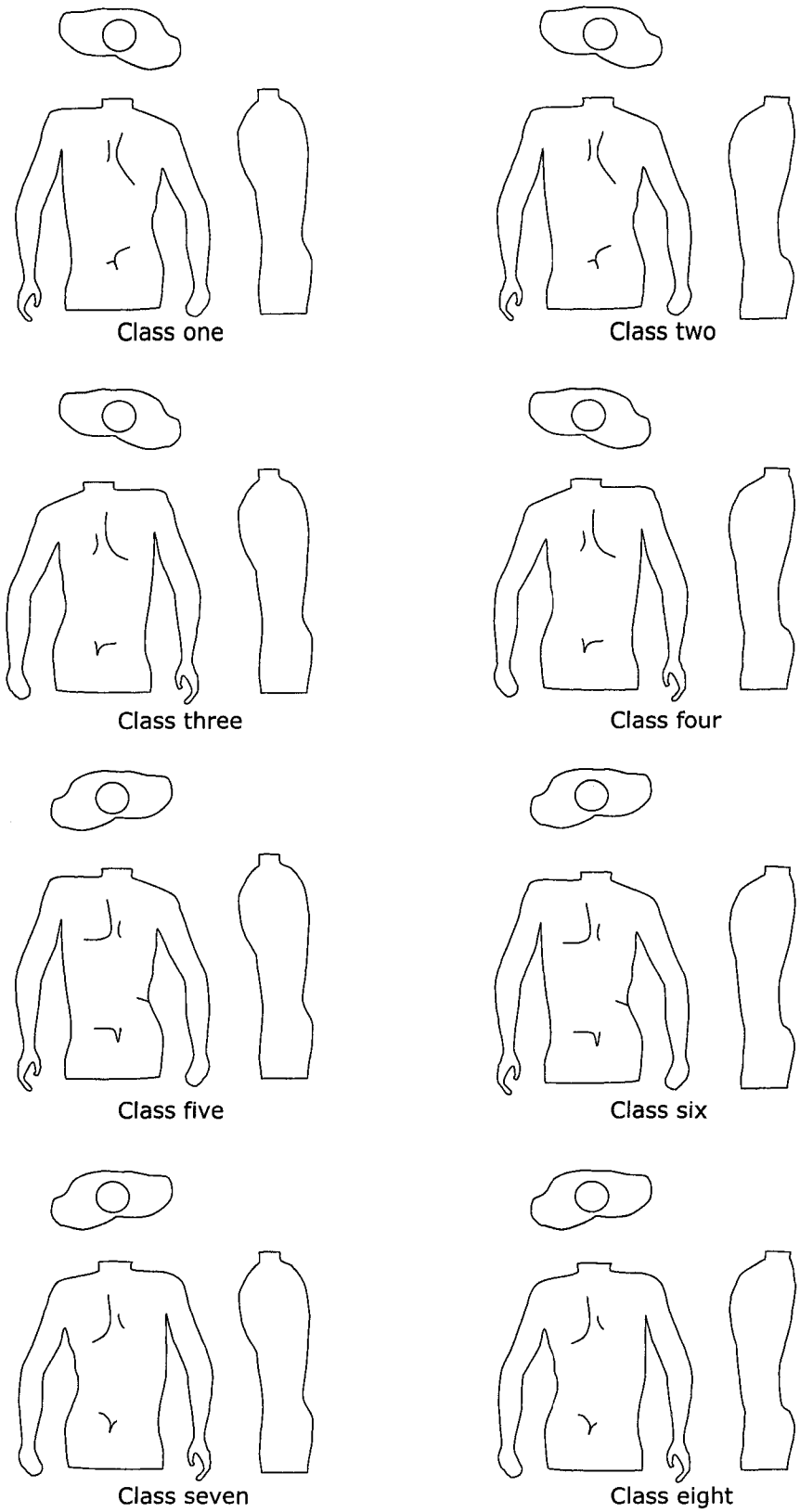

Fig. 4.7: Example classifications of torso deformity based on *twist*, *bend* and *tilt* indices.

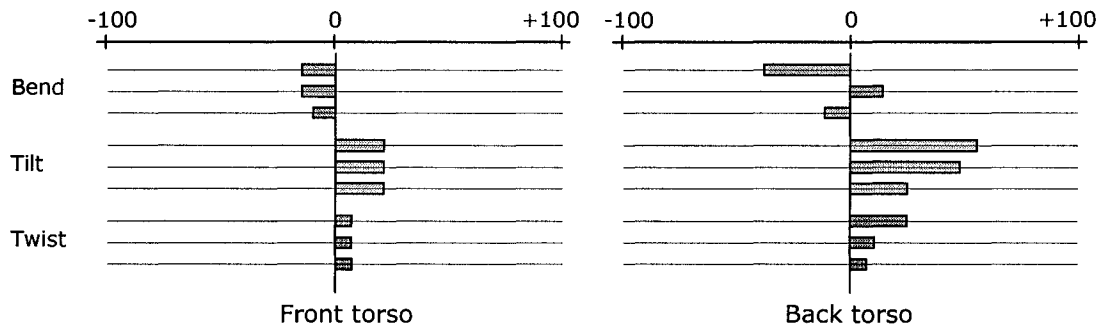

Fig. 4.8: A three section-status diagram of a scoliosis patient with a class five external deformity. The bar lengths correspond to absolute index values. The placement of the bars relative to the center line corresponds to the index sign. Right is positive and left is negative.

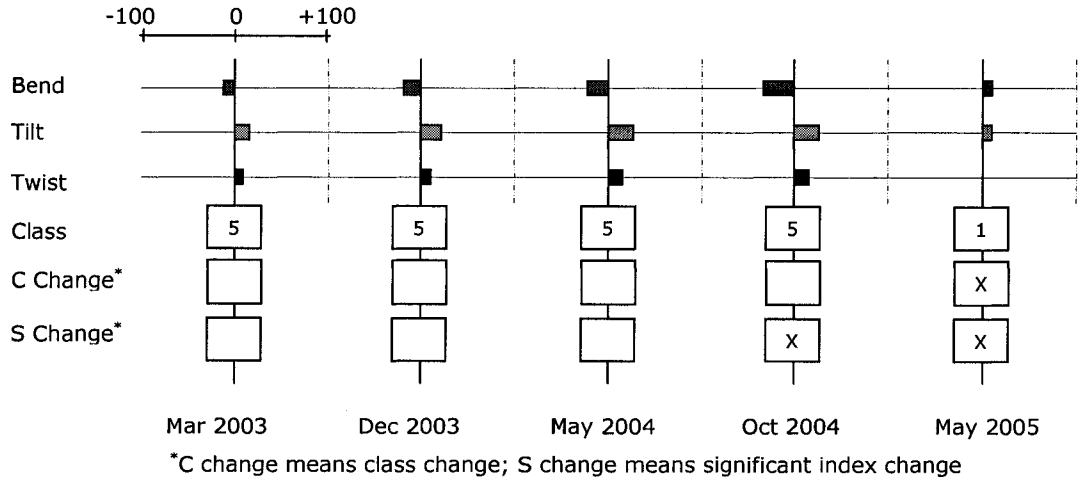

Fig. 4.9: The status chart of a scoliosis patient obtained over five clinic visits. Back pictures obtained during the first four visits are shown in Fig. 4.1. A significant change in index values is noticed at the October 2004 visit. The patient had spinal fusion surgery after October 2004. The resulting significant change in index and class values is noticed at the May 2005 visit.

4.5 IMPLEMENTATION

Torso surface images and clinical records of patients from the database of the scoliosis clinic at the Glenrose Rehabilitation Hospital, Edmonton, Canada, were examined to select patients for the study. The following inclusion criteria were used: 1) a diagnosis of idiopathic scoliosis; 2) age at first clinical visit of at least 8 years;

and 3) availability of one or more back torso or full torso images showing visible torso deformity. Patients admitted to the scoliosis clinic were generally deemed to have progressive scoliosis. The images were acquired as described in [1], [5]. The data collection procedures and experimental protocols were approved by the University health research ethics panel.

Three separate analyses were performed: 1) an analysis of the entire dataset to ascertain the gamut of the torso deformity indices and develop linear deformity scales; 2) an analysis of a subset of the dataset to correlate the deformity indices with existing clinical parameters; and 3) an analysis of the full torso images of four patients (three girls and one boy) to investigate the possibility of tracking the progression of scoliosis using the system.

In this section, we demonstrate the implementation of our system using the results of the third analysis (Table 4.3). The results of the first two analyses are presented in the next section. It took about 20 minutes to process an image on a Pentium IV PC running at 1.8 GHz. A $180\times180\times3$ structured splines model was used to obtain the dominant points.

4.5.1 Calculation of dominant points and indices of torso deformity

Fig. 4.10 shows front and back views of the full torso images of the four patients. Each quadrant was divided into three sectors for a total of 12 sectors. Fig. 4.10 also shows the centroids of the sectors superimposed on the images. Table 4.4 shows the deformation index values obtained for the four torso images used for this analysis.

4.5.2 Quantifying and tracking torso deformity

To illustrate the use of the system for quantifying and tracking torso deformity, status charts were created for each of the four patients (Fig. 4.11). The chart for the chosen patients showed at least one significant change or class change. The numbers

Table 4.3: Clinical description of the patient used to illustrate the system

Patient	Sex	Age	Cobb Angle	Height	Weight	DC	TT	CS
One	F	16.1	40	163	54	25	18	3.7
Two	F	15.1	50	157	53	33	11	1.4
Three	M	16.9	50	167	62	17	19	2.7
Four	F	15.4	45	169	60	17	19	2.5

Cobb angle, decompensation (DC) and trunk twist are given in degrees. Height is in cm. Weight is in kilograms. Cosmetic score (CS) ranges from 0 to 10 in increasing order of deformity. TT is trunk twist.

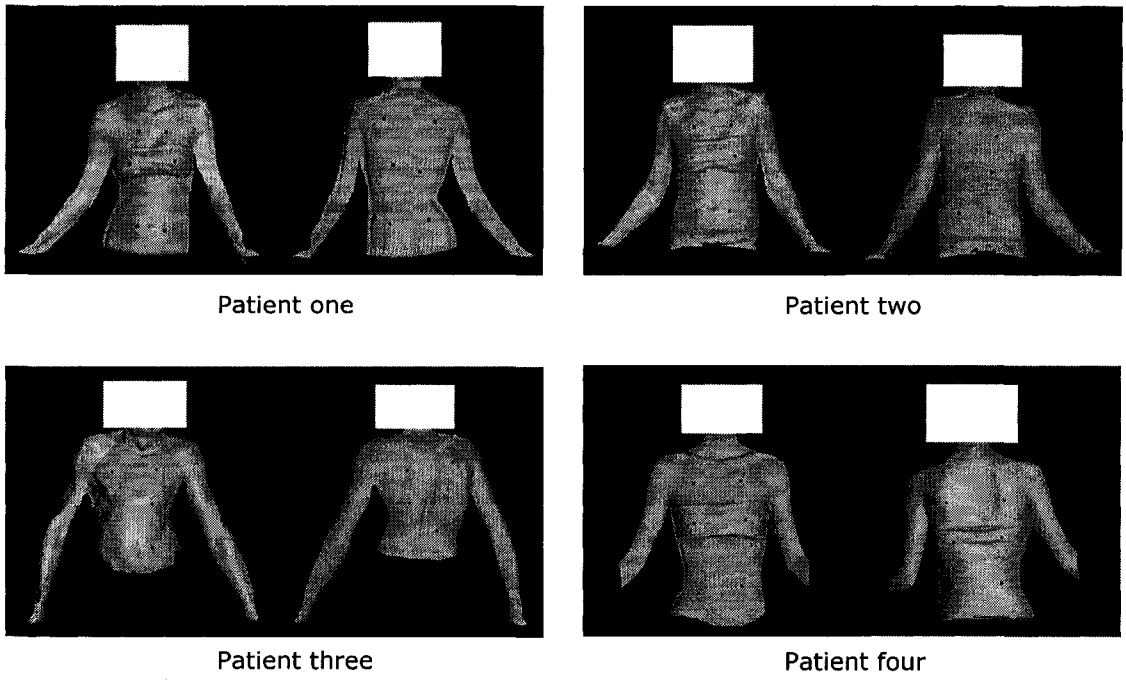

Fig. 4.10: Front and back views of patients used to illustrate the system. The centroids of the left and right horizontal sections of the front and back are superimposed on the images.

on Table 4.5 corresponds to the fourth entry in charts of Fig. 4.11.

4.6 VALIDATION AND RESULTS

This section presents the results of the analysis of the entire dataset to ascertain the gamut of the torso deformity indices and develop linear deformity scales and the analysis of a subset of the dataset to correlate the deformity indices with existing clinical parameters.

Table 4.4: Deformation index values of the patients used to illustrate the system.

Patient	Bend Ψ_B	Tilt Ψ_A	Twist Ψ_T	Class
One	24	42	36	1
Two	-19	27	16	5
Three	32	-60	-43	4
Four	25	-45	37	3

4.6.1 Ascertaining the gamut of scoliosis deformity indices

This involved 604 back torso images obtained from 203 patients and 43 full torso images obtained from 43 patients (out of the 203). This included back torso images from 10 boys and full torso images from two boys (out of the 10). The mean age was 14.2 ± 2.5 and 12.6 ± 2.7 years for the girls and boys. A $180 \times 180 \times 3$ model was used to obtain the dominant points from full torso scans and a $180 \times 90 \times 3$ model used for back torso images. The dominant points were aggregated using six sections for the back torso images, and 12 sections for the full torso images (that is, $w = 3$).

Table 4.5 shows the results. A conversion scheme was obtained for each deformity index by mapping the minimum and maximum values obtained to a 100-pt deformity scale. For example, a bend of 45mm[6] converted to a deformity score of 48 bend points, while a tilt of 45mm yielded a score of 39 tilt points. The lengths, widths and heights of the torso images were normalized to account for shape differences due to morphology and gender by selecting an equal number of points per cross-section (480 for full torso scans and 240 for back torso scans). The upper, lower, left and right extremities were cropped. An advantage of using spline interpolation was that holes created during the image acquisition stage were easily corrected for during dominant point detection.

[6] Note that as twist, bend and tilt indices are measures of the relative distribution of dominant points, they are originally measured in mm and then normalized into deformity scores.

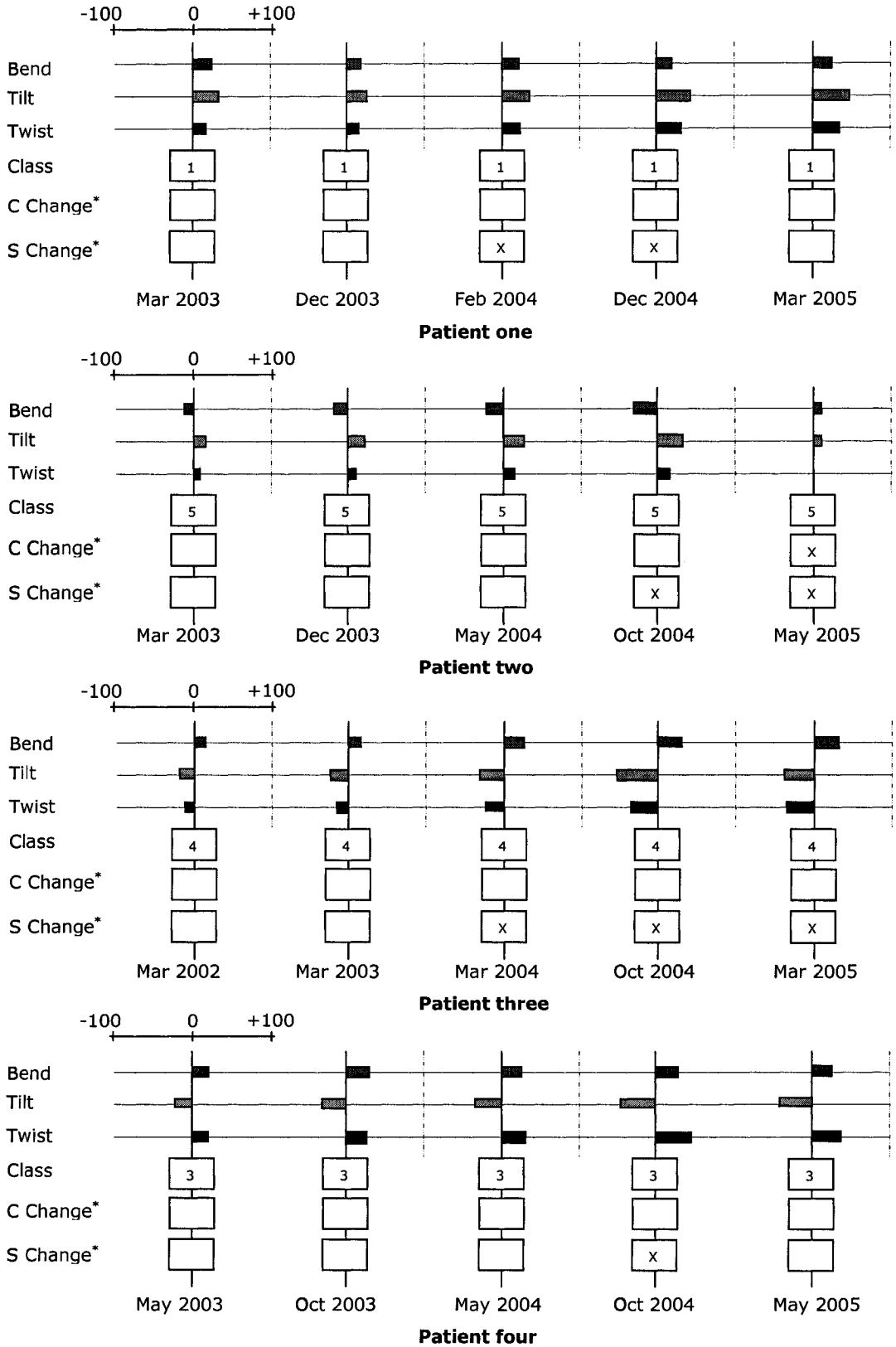

*C change records changes in class; S change records significant changes in index values

Fig. 4.11: The status chart of the four scoliosis patients.

Table 4.5: Statistical distribution of deformation indices in the validation dataset.

Type	# of images	# of patients	Bend Ψ_B		Tilt Ψ_A		Twist Ψ_T	
			Mean/SD	Range	Mean/SD	Range	Mean/SD	Range
Back	604	203	35.6/14.2	6-94	41.3/26.0	5-120	25.0/11.4	6-58
Full	43	43	45.5/8.3	9-72	36.9/17.4	8-68	28.5/10.9	14-48

SD = Standard Deviation. Table shows absolute values of twist, bend and asymmetry in mm.

Table 4.6: Statistical distribution of clinical parameters (mean/ SD) in the validation dataset.

	Cobb Angle	Height	Weight	DC	TT	Cosmetic Score
Girls	38.5/17.3	157.9/9.4	51.1/13.7	13.9/12.4	13.1/6.6	2.42/1.18
Boys	24.3/12.1	148.2/9.5	52.3/12.8	8.6/5.4	10.2/5.3	1.77/1.12

Cobb angle, decompensation (DC) and trunk twist are given in degrees. Height is in cm. Weight is in kilograms. Cosmetic score ranges between 0 and 10 in increasing order of deformity.

Table 4.7: Statistical distribution of normalized deformation indices in the secondary dataset.

Type	# of images	# of patients	Bend Ψ_B		Tilt Ψ_A		Twist Ψ_T	
			Mean/SD	Range	Mean/SD	Range	Mean/SD	Range
Back	205	40	31.4/9.8	4-90	31.6/18.3	8-98	32.6/19.7	4-100
Full	5	5	30.8/4.2	15-59	33.4/3.7	26-41	29.8/11.4	12-73

SD = Standard Deviation. Table shows absolute values of twist, bend and tilt in deformation points.

4.6.2 Comparison to existing clinical classification

Two hundred and five back images of 40 patients and five full torso images of five patients were used to compare the novel indices to existing clinical classification. The patients chosen for this analysis had a follow-up period of at least three years from their first clinical visit. They also had up to five back torso or full torso images in the database and clinical information obtained on the day each of the images were taken. Table 4.6 shows the clinical parameters utilized for this analysis. Table 4.7 shows the range of indices of deformation obtained for the images used in the

analysis. The deformation indices obtained are given in deformation points.

To obtain an equivalent classification to the existing clinical classification, a K-means classifier method was used to cluster the dominant point-based shape deformation indices into three clusters in 3-D shape descriptor space. The axes of the space corresponded to twist, bend and tilt. The clusters were termed *mild*, *moderate* and *severe*, based on the average of the norm of the shape indices in each cluster (that is, the cluster with the smallest average corresponded to *mild* while that with the largest average corresponded to *severe*). Table 4.8 shows some results.

The classification obtained was compared to two other classifications based on: 1) External deformity as measure by the cosmetic score[7] [37]; and 2) Internal deformity as measured by the Cobb angle, decompensation and trunk twist. The classifications were performed by a clinician who was not involved in developing the method. Table 4.9 shows the results of applying correlation analysis to the clinical and structured splines-based classifications. The novel classification significantly correlated with the external deformity classification based on the Cosmetic score (as expected) but not with the internal deformity classification. The classifications obtained did not change when Gaussian noise (with mean and standard deviation equal to the reconstruction accuracy of the imaging system used [1]) was added to the input images.

A clinician needs to make several decisions when treating a scoliosis patient. Two important decisions are: 1) Is immediate and/or serious intervention required? 2) Is further treatment and/or follow-up? To assess the ability of the novel classification scheme to furnish the answer to these queries, the *mild* and *moderate* categories were compared to the *severe* category to answer the first question. The *mild* category was compared to the *moderate* and *severe* categories to answer the second

[7] The cosmetic score is the ratio of waist diameter to the hip diameter relative to the locations of the wait and hip centers.

question. Results of these comparisons for each of the clinical classifications are shown in Table 4.10. The proposed classification system achieved the highest level of accuracy when compared to the external deformity classification.

Table 4.8: Six example classifications of back torso images of scoliosis patients.

	First	Second	Third	Fourth	Fifth	Sixth
Twist (pt)	15	12	34	62	30	77
Bend (pt)	26	18	50	56	100	98
Asymmetry (pt)	12	8	26	21	100	36
Norm (pt)	32	23	66	86	145	130
Classification	Mild	Mild	Moderate	Moderate	Severe	Severe

pt = deformity points.

Table 4.9: Result of applying correlation analysis (r^2) to the classifications obtained

	Internal Deformity	External Deformity	Dominant Point
Internal Deformity$^+$	1		
External Deformity	0.64	1	
Dominant Point	0.67	0.93*	1

*Statistically significant correlation ($p<0.05$). $^+$This was assessed from the Cobb angle.

Table 4.10: Results of comparing the classifications obtained using dominant point-based indices to clinical classification based on internal deformity and external deformity

	Mi and Mo VS Se		Mi VS Mo and Se	
	Internal Deformity	External Deformity	Internal Deformity	External Deformity
Accuracy (%)	84.3	96.7	87.1	94.8
False negative	22	2	11	3
False positive	11	5	16	8
Sensitivity	0.85	0.99	0.83	0.95
Specificity	0.82	0.93	0.89	0.95
Positive predictive value (PPV)	0.92	0.97	0.77	0.88
Negative predictive value (NPV)	0.69	0.97	0.92	0.98

Mi = Mild; Mo = Moderate; Se = Severe.

4.6.3 Distribution of the deformation classes

We investigated the distribution of the deformation classes in our dataset of 604 back torso images and 43 full torso images. Fig. 4.12 shows the distribution of the eight classes. Classes one and two had the highest percentage of members and classes six and seven had the lowest percentage of members. Overall, the majority of the torso scans in the datasets had a positive (right) bend.

4.7 CONCLUSIONS

This chapter considered the problem of quantifying the shape of a human torso with a view to tracking its changes over time and comparing it to the shape of other torsos. This was applied to the problem of quantifying and tracking the torso deformity caused by scoliosis. A three step approach was taken: sectioning the torso into a structured sequence of 2-D cross-sections; computing the dominant points of the cross-sections and interpolating to fill holes using *B*-spline curves; and obtaining a three-axial shape vector, comprising of *twist, bend* and *tilt* indices by aggregating the dominant points of the cross-sections. As most of the information present in a shape is concentrated at the dominant points [6], their use for our purposes ensured that the resulting classification of the torso is intuitive and based on the principal manifestations deformity: curvature and asymmetry.

Full torso images and back scan images were used to evaluate the effectiveness of the deformation indices obtained. A disadvantage of the system is that the indices obtained cannot be more accurate than the full torso or back torso images. As torso imaging is plagued by errors caused by positioning and motion (such as postural sway and breathing), these errors trickle down to the indices obtained. Thus, the inaccuracies of the imaging system used to obtain the torso images play an important role in the accuracy of the overall torso quantification. Though the indices

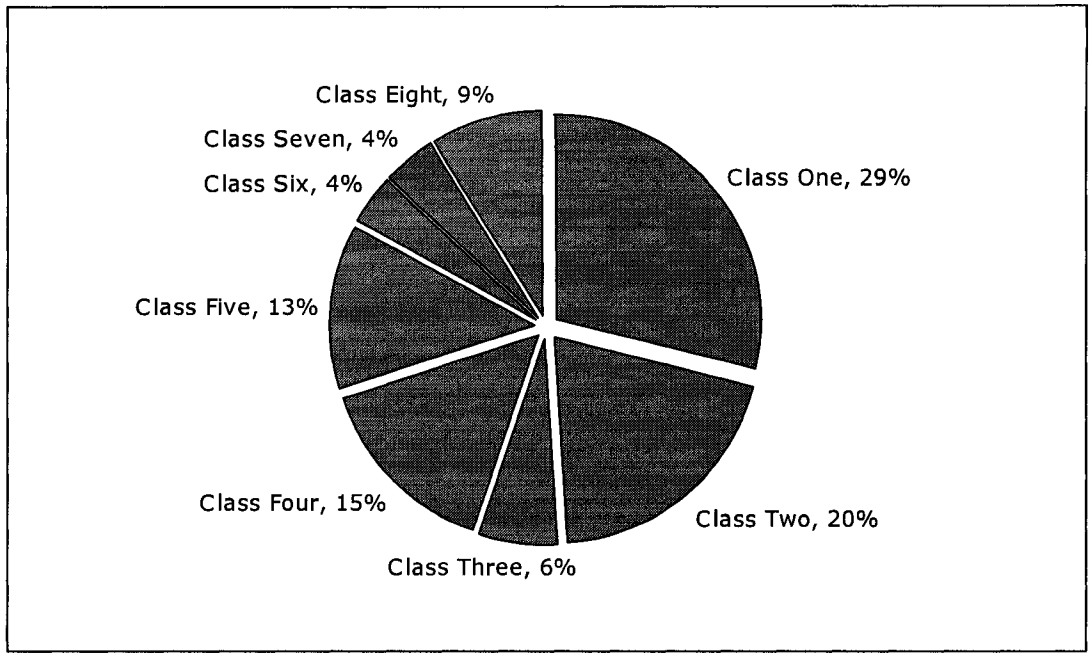

Fig. 4.12: Distribution of the full torso and back shape images by their class of deformity.

are orthogonal and form a basis vector in three-axis shape deformity space, individual components are affected differently by these errors.

Results show that the indices significantly correlated with the clinical assessment of the external deformity, but not with the assessment of the internal deformity. This was expected as the internal and external deformities are related but separate manifestations of scoliosis [8], [9]. An effect of scoliosis on the torso is an uneven prominence of back feature such as scapula and waist creases. In patients with high body mass index, the added body fat reduces these manifestations and results in an understatement of the underlying spinal deformity.

The indices achieved a classification accuracy of up 90% when the clinical assessment of the external deformity is considered as the gold standard. Accuracy in clinically relevant super-classifications (Table 4.10) ranged from 84 to 96%. The indices are not affected by age, gender and morphology as the process of computing the dominant points corrects for them. This is useful as shape changes are a

perennial problem in scoliosis monitoring because most scoliosis patients are in their adolescent growth-spurt period and show marked changes between clinical visits.

The system outperforms existing systems [6] and provides a more descriptive view of the torso shape. It is suitable for use in the fast-paced clinical environment as it only takes about 20 minutes to obtain the indices. Future work explores application of the system to tracking scoliosis and predicting its progression.

REFERENCES

1. P. O. Ajemba, N. G. Durdle, D. L. Hill, and V. J. Raso, 'A torso imaging system for quantifying the deformity associated with scoliosis,' *IEEE Transactions on Instrumentation and Measurements,* vol. 56, no. 5, October 2007.
2. P. O. Ajemba, N. G. Durdle, and V. J. Raso, 'Quantifying torso deformity using dominant points obtained from structured splines models,' Submitted to *IEEE Transactions on Image Processing*, 2007.
3. Y. P. Wang, S. L. Lee, K. Toraichi, 'Multiscale curvature-based shape representation using B-spline wavelets,' *IEEE Transactions on Image Processing,* vol. 8, no. 11, pp. 1586-1592, 1999.
4. S. Belongie, J. Malik, and J. Puzicha, 'Shape matching and object recognition using shape contexts,' *IEEE Transactions on Pattern Analysis and Machine Intelligence*, vol. 24, no. 4, pp. 509–22, 2002.
5. V. J. Raso, E. Lou, D. L. Hill, J. K. Mahood, M. J. Moreau, N. G. Durdle, 'Trunk distortion in adolescent idiopathic scoliosis,' *Journal of Pediatric Orthopedics*, vol. 18, no. 3, pp. 22-26, 1998.
6. P. O. Ajemba, N. G. Durdle, D. Hill, V. J. Raso, 'Classifying torso deformity in scoliosis using orthogonal maps of the torso, *Medical Biological Engineering and Computing,* vol. 45, pp. 575-584, June 2007.
7. F. Attneave, 'Some Informational Aspects of Visual Perception,' *Psychology Review*, vol. 61, no. 3, pp. 183-193, 1954.
8. C. J. Goldberg, M. Kaliszer, D. P. Moore, E. E. Fogarty, F. E. Dowling, 'Surface Topography, Cobb angles and cosmetic change in scoliosis,' *Spine*, vol. 26, pp E55-63, 2001.
9. R. A. Dickson, 'Spinal Deformity - Adolescent Idiopathic Scoliosis: Nonoperative Treatment,' *Spine*, vol. 24, no. 24, pp 2601-2606, 1999.

CHAPTER 5

SHAPE ANALYSIS: ORTHOGONAL MAPS [N]

5.1 INTRODUCTION

This chapter presents a technique for assessing the torso and classifying scoliosis into mild, moderate and severe categories using two indices, *twist* and *bend*, obtained from orthogonally transformed images of the full torso surface called orthogonal maps. Four transforms are used. The *twist* index gives an indication of the torso axial rotation. The *bend* index gives an indication of the overall severity of lateral tilt, shoulder hump differences and waist crease. The technique gives a visual representation of the entire torso in one view and is tested on scans of eight non-scoliosis and 22 scoliosis volunteers. It is viable for use in a clinical environment.

5.2 ORTHOGONAL MAPS

The method of quantifying changes in torso shape presented in this chapter relies on orthogonally transformed images of the torso called *orthogonal maps* and *half-difference maps* derived from orthogonal maps. In this section, we describe four orthogonal and half-difference maps that can be used to assess torso asymmetry.

Definition (Orthogonal maps): An *orthogonal map* is obtained by applying an orthogonal transform to the surface map of a 3D object.

Orthogonal transforms map cylindrical (ρ,θ,Z) or spherical (ρ,θ,ϕ) coordinate systems onto normalized Cartesian coordinate systems (x,y,z). Each map consists of a $r \times s$ array of numbers, where r is the number of cross-sections or layers and

[N] A version of this chapter has been published. P. O. Ajemba, N. G. Durdle, D. L. Hill, and V. J. Raso, 'Classifying torso deformity in scoliosis using orthogonal maps of the torso,' *Medical and Biological Engineering and Computing*, vol. 45, pp. 575-584, June 2007.

s is the number of points per cross-section. (The points on any particular cross-section are typically evenly spaced $360/s$ degrees apart.) The numbering of the r cross-sections is from the bottom to the top of the torso. The numbering of the s points per cross- section starts at a point 90^0 from a *maximal diameter* of the torso cross-section[1]. By varying r and s, any arbitrary precision can be obtained.

Definition (Half-difference maps): A *half-difference map* is obtained by subtracting the right half of an orthogonal map from its left half. It is a measure of the lateral asymmetry in the shape.

5.2.1 The axial line technique

A description of this technique appeared in a preliminary version of this work [1]. In this technique, the centroids of each of r cross-sections are calculated from the s evenly spaced points per cross-section (Fig. 5.1a). An *axial line* is then obtained by joining the centroids. The cylindrical to Cartesian coordinate transformation used Γ_{al} is defined as:

$$\Gamma_{al} := \{x \to \theta, y \to Z, z \to R = \rho\}.$$

The elements of the $r \times s$ array correspond to the horizontal distance R, between each of the s points per cross-section and the axial line.

5.2.2 The unfolded surface technique

Here, the absolute values of the x and y coordinates of each of the s evenly spaced points on each r cross-section are computed (Fig. 5.1b). Two $r \times s$ arrays are obtained. The elements of the first array correspond to the x coordinates while the elements of the second array correspond to the y coordinates. The cylindrical to

[1] The *maximal diameter* of a closed 2D shape such as a torso cross-section is the longest distance between any two points in the convex hull of the shape.

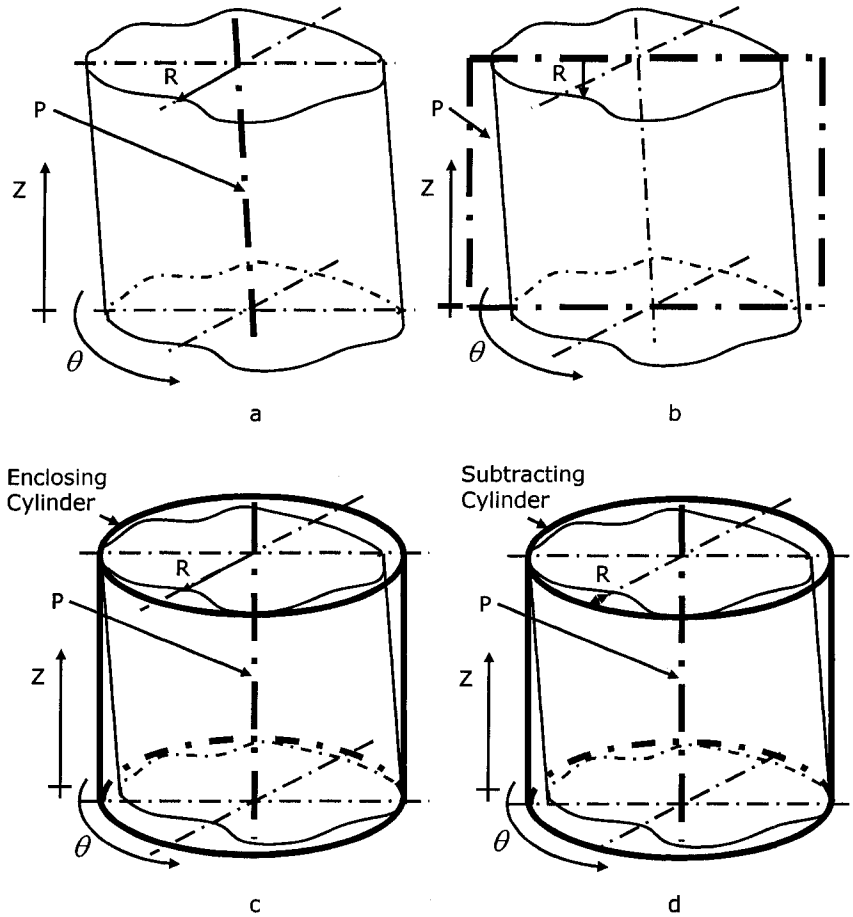

Fig. 5.1: Generating the four orthogonal maps: a) axial line; b) unfolded cylinder; c) enclosing cylinder; and d) subtracting cylinder. P is the axis or plane through about which the transform is taken. The r cross-sections are taken along the Z axis while the s points per cross-section are taken along the θ axis.

Cartesian coordinate transformation used for the first map Γ_{usx} is defined as:

$$\Gamma_{usx} := \{x \to \theta, y \to Z, z \to R = \rho \cdot \cos\theta\}.$$

The transformation used for the second map Γ_{usy} is defined as:

$$\Gamma_{usy} := \{x \to \theta, y \to Z, z \to R = \rho \cdot \sin\theta\}.$$

For this study, the first map (in this case a plot of the x values) would be used as the front and back of the human torso contain more information related to torso deformity than the two sides.

5.2.3 The enclosing cylinder technique

In this technique, an enclosing cylinder is defined as the smallest cylinder that can encompass the entire 3D object (Fig. 5.1c). The elements of the $r \times s$ array correspond to the length of a line R, parallel to the horizontal axis and joining each of the $r \times s$ points to the centroid of the enclosing cylinder. The cylindrical to Cartesian coordinate transformation used Γ_{ec} is defined as:

$$\Gamma_{ec} := \{x \to \theta, y \to Z, z \to R = \rho_{ec}\},$$

where ρ_{ec} is the corresponding coordinate of the enclosing cylinder.

5.2.4 The subtracting cylinder technique

Here, a subtracting cylinder is defined as the smallest cylinder that can fit the entire shape (Fig. 5.1d). It is similar to the enclosing cylinder. The elements of the $r \times s$ array correspond to the absolute difference between the length of a line R, parallel to the horizontal axis and joining each of the $r \times s$ points to the centroid of the subtracting cylinder and the radius of the subtracting cylinder. The orthogonal map is the plot of the $r \times s$ array. The cylindrical to Cartesian coordinate transformation used Γ_{sc} is defined as:

$$\Gamma_{sc} := \{x \to \theta, y \to Z, z \to R = D - \rho_{sc}\}.$$

D is the radius of the subtracting cylinder and ρ_{sc} is the corresponding coordinate of the subtracting cylinder.

5.2.5 An example

A computer model of an elliptical frustum having 30^0 *bend* and 30^0 *twist* (Fig. 5.2) was created to illustrate the mapping techniques. Fig. 5.3 shows the four corresponding orthogonal maps and Fig. 5.4 shows the four corresponding difference maps. The contours on the orthogonal maps correspond to iso-values of the radius of curvature. The *peaks* in the maps correspond to *bumps*, while the *valleys* correspond to *dimples* in the transformed surface[2].

5.3 DEFORMATION INDICES

This section describes the *bend* and *twist* indices obtained from orthogonal maps [1].

5.3.1 The *twist* index

The *twist* index reflects the transverse asymmetry present in cross-sections of the torso and noticeable in its coronal plane view. On orthogonal maps, the troughs of the contours at the edge of the torso correspond to *twist lines*. The *twist* index is a measure of the average slope of the two *twist lines* at the edges of the torso.

Definition (*twist line*): The *twist lines* of a 3D shape are the closures of the paths of maximal curvature at each incremental cross-section on the orthogonal maps of the shape.

Twist lines are computed along the horizontal-vertical (principal) axes but the *twist* index is computed in the coronal plane. The *prominence* of a horizontal-vertical *twist line* at any point is directly proportional to the horizontal curvature of the point on the orthogonal map. The value of the *twist* index at a cross-section is the rate of change of the *twist line* at the cross-section. A circular cylinder would have no *twist lines* and hence zero apparent *twist* as the operation of twisting a circular cylinder

[2] The orthogonal maps of a perfect circular cylinder are devoid of contours.

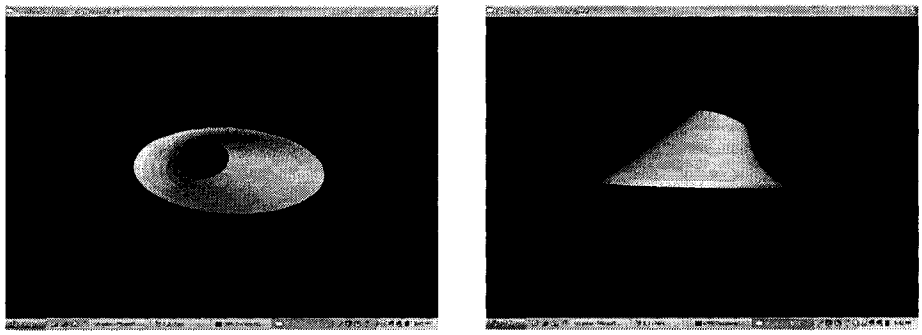

a b

Fig. 5.2: A model of an elliptical frustum with 30^0 *twist* and 30^0 *bend*. a) top; b) side view.

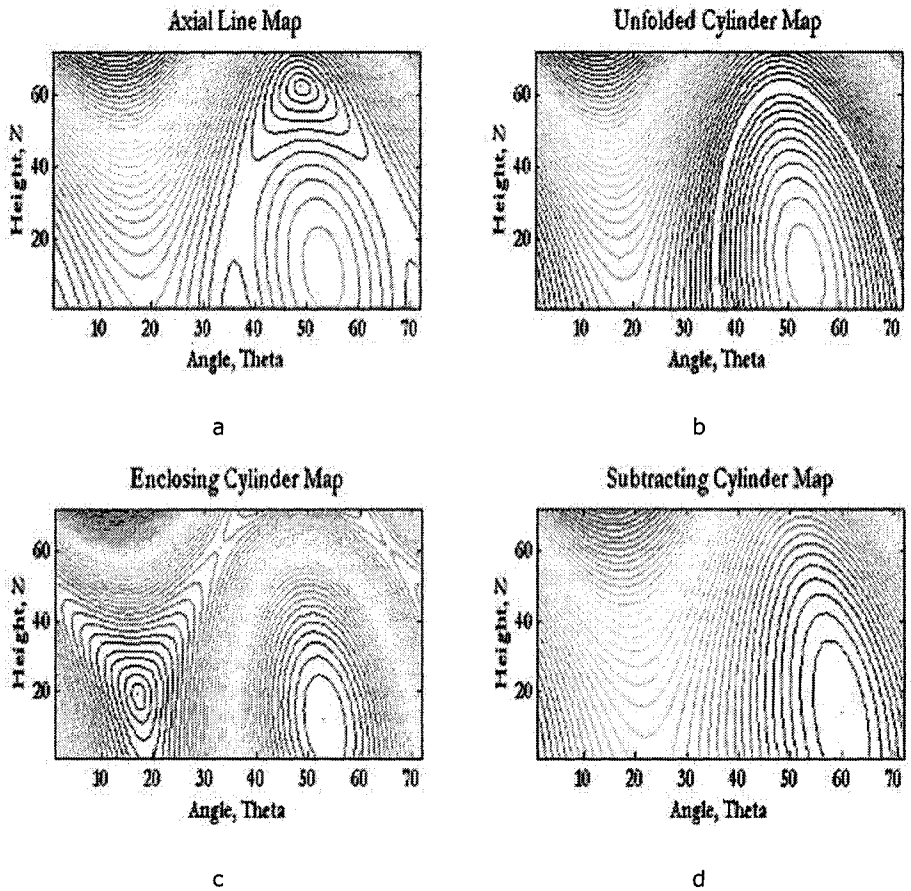

a b

c d

Fig. 5.3: The orthogonal maps of an elliptical frustum with 30^0 *twist* and 30^0 *bend*. The maps emphasize different features. The *axial line map* features a distinct peak that gradually slopes into a distinct valley. The *unfolded cylinder map* has a more pronounced slope at the base of the peak. The *enclosing cylinder* map features two distinct opposing peaks. The *subtracting cylinder map* features a distinct peak that gradually slopes into a very broad valley.

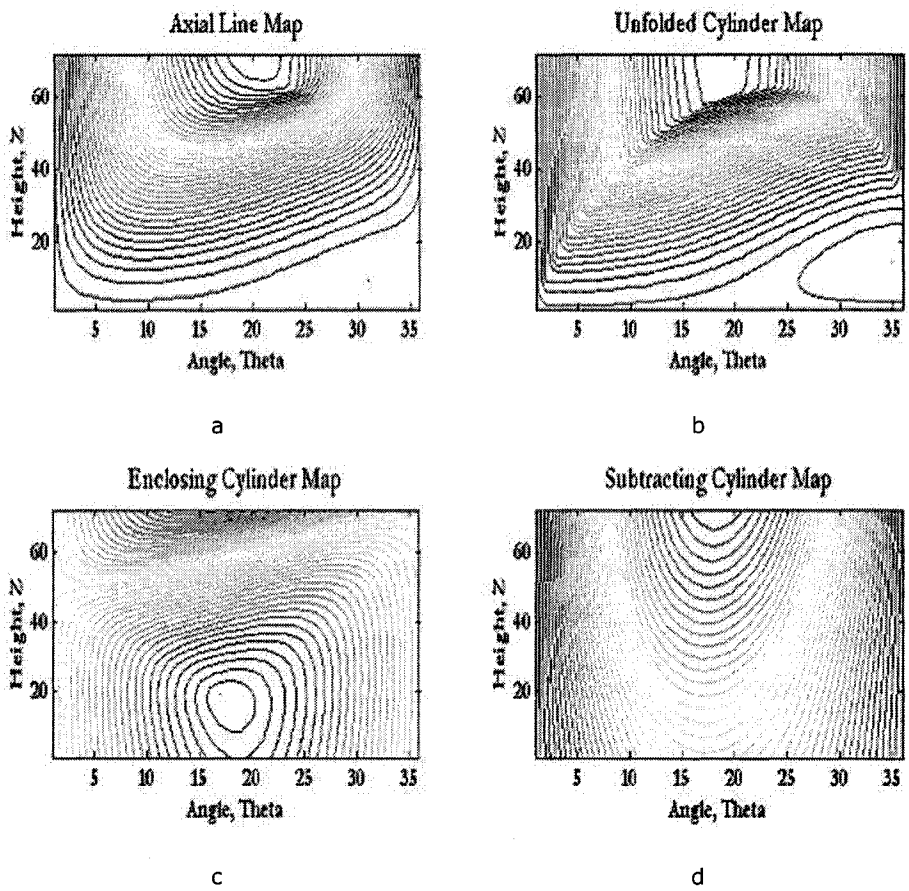

Fig. 5.4: Half-difference maps of an elliptical frustum with 30^0 *twist* and 30^0 *bend*. a) axial line; b) unfolded cylinder; c) enclosing cylinder; and d) subtracting cylinder.

leaves it physically unchanged. Other shapes which deviate from the circular cylinder have at least one *twist line* and symmetric objects have at least two. (The deformed elliptical frustum of Fig. 5.2 has two *twist lines* which correspond to the two vertical edges of its side view.)

For an orthogonal map made from a $r \times s$ array, the *twist* at cross-section i is given by:

$$T_i = \frac{2 \cdot \pi}{r} \cdot s \cdot \frac{\Delta x}{\Delta y}. \qquad (1)$$

Here, Δx is the change in degree units of the 'twist line' per Δy change in the index of the cross-sections. For a 72 × 72 array with $\Delta y = 1$, (1) reduces to $T_i = 2 \cdot \pi \cdot \Delta x$.

5.3.2 The *bend* index

The *bend* index is a measure of the abnormal lateral deformation present in cross-sections of the torso and noticeable in its posterior-anterior view. The *bend* index is a measure of the average slope of the *bend line* that represents the difference between the unsigned magnitudes of the x-coordinates of the surface of the torso.

Definition (*bend line*): The *bend line* of a 3D shape is the closure of the highest points of incremental cross-sections on the half-difference maps of the shape.

Like twist lines, *bend* lines are computed along the horizontal-vertical (principal) axes but the *bend* index is measured in the lateral (or anterior-posterior) plane. The prominence of a horizontal-vertical *bend* line at any point is directly proportional to the horizontal curvature of the point in the half-difference surface. The value of the *bend* index at each cross-section is obtained from the radius of curvature ρ, of the *bend line* at the cross-section.

Let $y = y(t)$ and $z = z(t)$ represent the height and depth of a *bend line*, t is the index of the cross-section, the radius of curvature of the line at cross-section i is:

$$\rho_i = \frac{1}{K_i} = \frac{(y_i'^2 + z_i'^2)^{3/2}}{|y_i' z_i'' - z_i' y_i''|}. \qquad (2)$$

Where K_i is the curvature at i. From (3.2), the *bend* at cross-section i is given by:

$$B_i = \sin^{-1}\left(\rho_i / 2 \cdot h\right). \qquad (3)$$

Here, h is the height of cross-section i, measured from the base of the torso. The value of z at each cross-section is indicative of the lateral deviation of the cross-section from the central axis of the base cross-section.

5.4 CLASSIFICATION OF DEFORMITY

5.4.1 Analysis of Computer Models

Mathematical models consisting of elliptical frustums having various degrees of twist (ranging from 0 to 90^0 in 5^0 steps) and bend (also ranging from 0 to 90^0 in 5^0 steps) were used. 361 models corresponding to all the possible permutations of the selected twist and bend values were created. The four orthogonal maps and their corresponding difference maps were generated for each model. *Twist* and *bend* indices were obtained from each map. The degree of *twist* and *bend* present in each model was blindly ascertained quantitatively using equations (1)-(3). It took about 10 minutes to process a model on a Pentium IV PC running at 1.8GHz. The obtained indices were used to classify the computer models into mild, moderate and severe deformity categories[3]. Table 5.1 shows a pseudo code for the classification system used. Table 5.2 shows typical classification results.

The classification based on the computed indices showed a 100% correspondence with classification based on the known values of the deformation indices validating the proposed technique. Unexpected differences were observed in the possibility of intuitively guessing the classification of maps from their contours. In general, it was relatively easier to guess the classification of axial line maps and unfolded cylinder maps than enclosing cylinder maps and subtracting cylinder maps.

5.4.2 Analysis of Human Torso Scans

Torso scans of 30 volunteers were used to investigate the utility of the system for quantifying torso shape. The scans were obtained using the method of Ajemba *et al.* [2]. The reproduction accuracy of the method was reported to be 1.1±0.9mm [3].

---

[3] As *twist* and *bend* indices are basis vectors in deformity space, the classification uses their norm.

Table 5.1: Pseudo code for classifying the deformation of models of a frustum by severity

IF *twist* AND *bend* $<20^0$	Mild
ELSE IF *twist* AND/OR *bend* $>20^0$	
AND IF *twist* AND *bend* $<60^0$	Moderate
ELSE	Severe

Table 5.2: Example classifications of computer models of a frustum

	Example 1	Example 2	Example 3	Example 4	Example 5	Example 6
Twist (^{0})	10	5	30	0	70	90
Bend (^{0})	10	0	40	50	20	40
Classification	Mild	Mild	Moderate	Moderate	Severe	Severe

The volunteers were recruited from the scoliosis clinic of the Glenrose Rehabilitation Hospital in Edmonton, Alberta, Canada. Twenty-two of the 30 volunteers had scoliosis (mean age 13.1 years). Of the 22, 15 were female. All the volunteers who had no scoliosis (mean age 21.2 years) were male[4]. For this study, the lengths, widths and heights of the torso scans were normalized to account for shape differences due to morphology and gender by selecting an equal number of points per cross-section. The upper, lower, left and right extremities were cropped and a spline interpolation method was used to fill in any missing holes that arose during the image acquisition stage. For each torso scan, orthogonal maps consisting of a 72 × 72 array were obtained from 72 equally spaced cross-sections each having 72 points per cross-section spaced at 50 degree intervals. *Bend* and *twist* indices were calculated for each scan. Fig. 5.5 shows back views of typical *mild*, *moderate* and *severe* scoliosis patients. Fig. 5.6 shows the four orthogonal maps obtained from the torso scan of a male volunteer who did not have scoliosis. Table 5.3 shows the ranges of *twist* and *bend* indices for none, *mild*, *moderate* and *severe* scoliosis volunteers for each of the four orthogonal maps.

[4] Their torso scans were used to check the null-response pattern of the system.

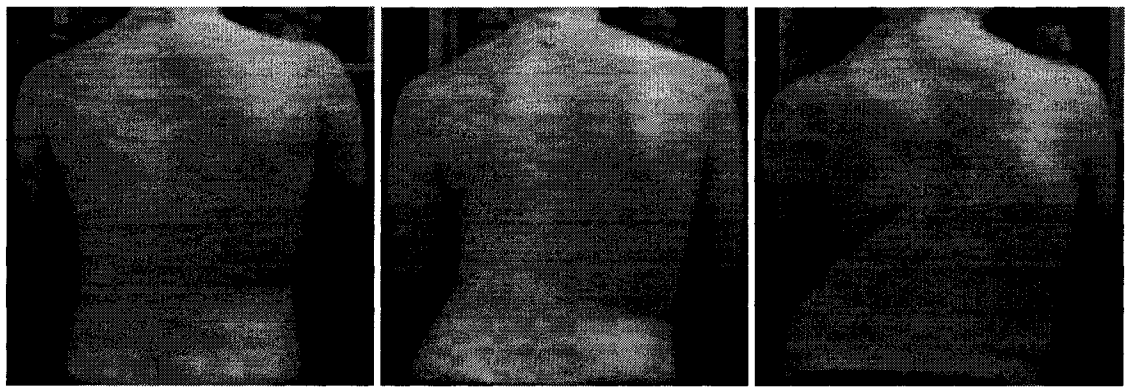

Fig. 5.5: Back views of typical mild, moderate and severe scoliosis patients.

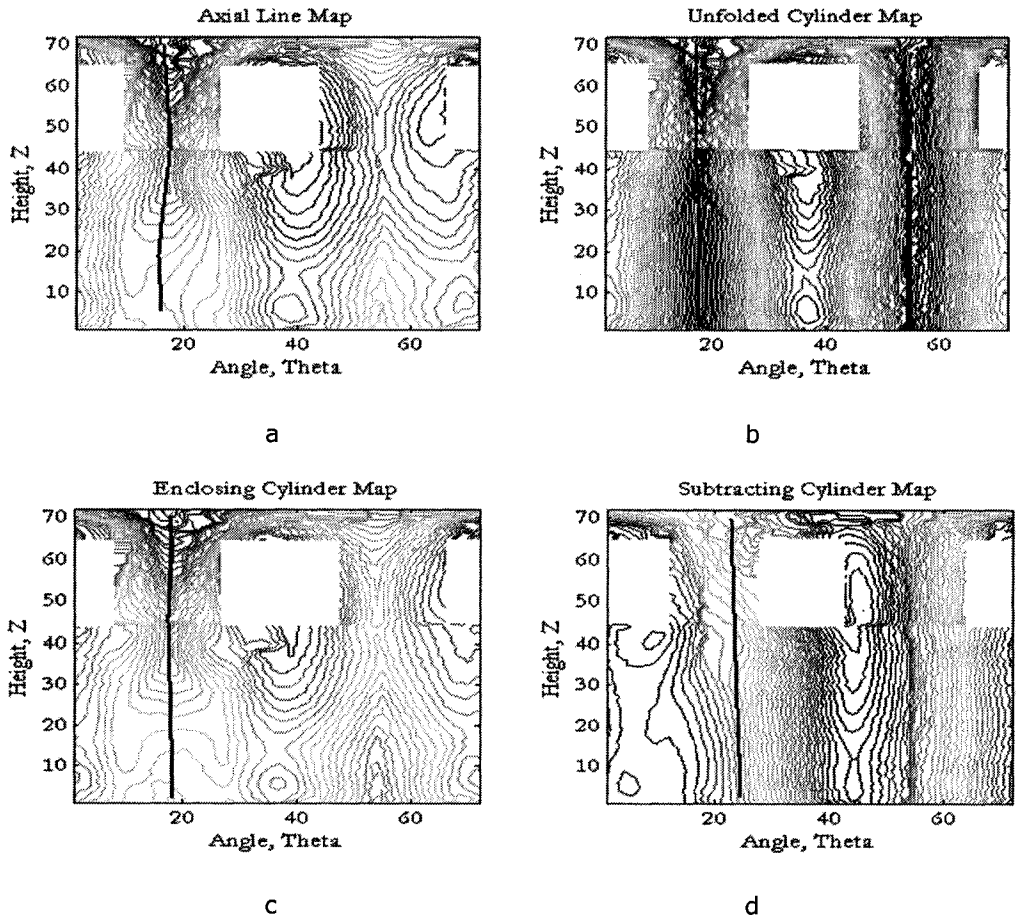

Fig. 5.6: The four different orthogonal maps of a male volunteer without scoliosis. The solid black lines on the right half of the maps are the twist lines. The white patches on the maps were generated when the arms where cropped of the torso at the shoulder region.

Table 5.3: Range of values for the *twist* and *bend* indices for none, mild, moderate and severe scoliosis patients for each of the four orthogonal maps

	Axial Line		Unfolded Cylinder		Enclosing Cylinder		Subtracting Cylinder	
	Twist (^{0})	Bend (^{0})	Twist (^{0})	Bend (^{0})	Twist (^{0})	Bend (^{0})	Twist (^{0})	Bend (^{0})
No Scoliosis	1.0-1.2	1.0-1.4	1.0-1.2	1.1-1.5	1.0-1.4	1.0-1.5	1.0-1.4	1.2-1.5
Mi Scoliosis	1.4-2.2	1.7-3.2	1.5-2.2	1.7-3.2	1.5-2.3	1.7-3.3	1.5-2.2	1.7-3.4
Mo Scoliosis	3.4-3.9	3.5-5.5	3.3-3.8	3.5-5.4	3.2-4.0	3.5-5.3	3.1-4.1	3.5-5.6
Se Scoliosis	4.5-5.6	5.6-7.0	4.6-5.5	5.5-7.2	4.7-5.6	5.6-7.1	4.5-5.5	5.5-7.3

Mi: Mild; Mo: Moderate; Se: Severe.

To create gold standards for the classification obtained using orthogonal map indices, an experienced clinician was asked to retrospectively assign scores to the volunteers in three categories using a visual analog scale. The categories were: 1) external deformity as evidenced from 2D and 3D torso images taken on the day of clinical assessment; 2) internal deformity as evidenced from radio- graphs and other clinical parameters taken on the day of assessment; and 3) clinical history up to the day of assessment based on clinical records. The scores obtained were compared to the Euclidean norm of the twist and bend indices obtained from axial line orthogonal maps. Boundaries for classifying the volunteers into categories were obtained by assessing the histograms and scatter plots of the distributions of scores obtained for break points (Table 5.4). The classification is shown in Table 5.5.

It can be observed from Table 5.5 that eight of the 22 volunteers who have scoliosis (six females and two males) had the same classifications in all three clinical categories. Seven of these also had identical orthogonal map based classifications. The clinical classifications of four of the volunteers ran the available gamut and the orthogonal maps classifier ranked each case as moderate. Table 5.6 shows the result of applying correlation analysis to the clinical and orthogonal maps-based classes. It can be seen that the orthogonal maps based classification significantly correlated with the external deformity classification (as expected) but not with the internal

Table 5.4: Range of scores used in classifying volunteers into *mild*, *moderate* and *severe*

	Internal Deformity	External Deformity	Clinical History	Orthogonal Map
Mild	<1.5	<2.0	<2.0	<4.0
Moderate	1.5-3.5	2.0-3.5	2.0-3.5	4.0-6.0
Severe	>3.5	>3.5	>3.5	>6.0

Table 5.5: Comparison of classifications of scoliosis patients into *mild*, *moderate* and *severe*

	Sex	Age	Int Deformity		Ext Deformity		Clinical History		Orthogonal Map			
			Score	Class	Score	Class	Score	Class	Twist	Bend	Score	Class
1	F	17	3.4	Mo	3.7	Mo	2.5	Mo	3.4	2.7	4.3	Mo
2	M	16	3.3	Mo	4.1	Se	3.1	Se	3.9	4.3	5.8	Mo
3	F	15	1.4	Mi	3.4	Mo	2.1	Mo	2.2	3.2	3.9	Mo
4	F	10	4.0	Se	3.0	Mo	1.2	Mi	3.6	4.8	6.0	Mo
5	F	14	2.0	Mo	2.4	Mo	1.7	Mo	4.5	6.5	7.9	Se
6	M	9	4.9	Se	2.1	Mo	1.4	Mi	3.7	4.7	6.0	Mo
7	M	16	3.9	Se	1.7	Mi	3.0	Mo	5.6	7.0	9.0	Se
8	F	14	4.7	Se	4.1	Se	3.8	Se	4.9	6.3	8.0	Se
9	F	14	2.6	Mo	0.6	Mi	1.4	Mi	3.5	5.5	6.5	Mi
10	F	15	0.1	Mi	2.3	Mo	0.3	Mi	3.6	2.3	4.2	Mo
11	M	9	1.4	Mi	2.4	Mo	1.4	Mi	3.4	3.5	4.9	Mo
12	M	7	0.9	Mi	1.8	Mi	1.6	Mi	1.8	2.4	3.0	Mi
13	F	15	1.2	Mi	1.5	Mi	1.6	Mi	2.6	1.6	3.1	Mi
14	F	14	1.2	Mi	2.7	Mo	1.9	Mi	2.7	2.9	3.9	Mi
15	F	13	2.6	Mo	2.5	Mo	2.0	Mo	2.8	3.3	4.3	Mo
16	M	14	2.7	Mo	2.3	Mo	2.5	Mo	4.0	2.3	4.6	Mo
17	F	12	2.4	Mo	1.7	Mi	1.3	Mi	2.2	1.7	2.8	Mi
18	F	11	1.1	Mi	0.9	Mi	1.2	Mi	1.4	2.5	2.9	Mi
19	M	9	2.7	Mo	4.0	Se	3.0	Mo	4.0	5.4	6.7	Se
20	F	16	4.0	Se	4.1	Se	3.0	Mo	3.4	6.4	7.2	Se
21	F	13	1.0	Mi	2.1	Mo	3.8	Se	4.0	2.2	4.6	Mo
22	F	15	1.0	Mi	1.1	Mi	2.2	Mo	2.2	1.9	2.9	Mi

RMS = root mean square; SD = standard deviation; L = length; W = width; H = height; sample size = 20.

deformity or clinical history classifications (which correlated with each other). The classification obtained did not change when Guassian noise (with mean and standard

Table 5.6: Result of applying correlation analysis to the classifications obtained

	Internal Deformity	External Deformity	Clinical History	Orthogonal Map
Internal Deformity	1			
External Deformity	0.51	1		
Clinical History	0.81*	0.60	1	
Orthogonal Map	0.61	0.85*	0.54	1

*Statistically significant correlation ($p<0.05$)

deviation equal to the reconstruction accuracy of the imaging system used) was added to the input torso scans.

After seeing a patient on any given day at a scoliosis clinic, the clinician needs to make a number of decisions. Two of the most important of these are: 1) Is immediate and/or serious intervention required? 2) Is further treatment and/or follow-up required? To assess the ability of the orthogonal classification scheme to help answer the questions, the *mild* and *moderate* categories were compared to the *severe* category for the first question and the *mild* category was compared to the *moderate* and *severe* categories to answer the second question. Results of these comparisons for each of the clinical classifications are shown in Table 5.7. The proposed classification system achieved the highest levels of accuracy when compared to the external deformity clinical classification.

5.5 DISCUSSION

A method of assessing torso shape using orthogonal maps is presented. Orthogonal maps are complete scans of three-dimensional objects that have been *unfolded* by applying polar to Cartesian coordinate transforms. They give a visual representation of the entire torso in one view. This is important as the overall impression simplifies the identification of anomalies on torso scans and the analysis of torso shape. Four different types of orthogonal maps (axial line, unfolded cylinder, enclosing cylinder and subtracting cylinder) produced by applying different types of orthogonal

Table 5.7: Results of comparing the classification obtained with the axial line indices to clinical classification based on internal deformity, external deformity and clinical history

	Mild and Moderate VS Severe			Mild VS Moderate and Severe		
	Internal Deformity	External Deformity	Clinical History	Internal Deformity	External Deformity	Clinical History
Accuracy (%)	54.5	86.4	72.7	72.7	95.5	77.3
False negative	2	1	2	2	1	1
False positive	2	2	4	4	1	4
Sensitivity	0.60	0.75	0.33	0.85	0.93	0.92
Specificity	0.88	0.89	0.79	0.56	0.86	0.60
Positive predictive value (PPV)	0.60	0.60	0.20	0.73	0.93	0.73
Negative predictive value (NPV)	0.88	0.94	0.88	0.71	0.86	0.86

transforms were evaluated. Two indices, *twist* and *bend*, derived from the maps were used to describe torso shape.

The sensitivity of the technique to detecting torso deformity and the possibility of classifying torso scans according to their degrees of deformity into *mild*, *moderate* and *severe* categories were explored. The indices of asymmetry are not affected by age, gender and morphometry as the process of computing the orthogonal maps automatically normalizes for these factors. This is an important feature as scoliosis progresses rapidly during the adolescent growth spurt period and the morphometry and shape of many scoliosis patients' torsos change significantly between visits to the clinic.

A weakness of the method is that its accuracy cannot be better than the accuracy of the imaging system employed to capture the torso scans used. The accuracy of the system is also affected by the accuracy of the techniques used to pre-process the torso scans and to compute the torso cross-sections. The indices obtained are poor predictors ($p>0.05$) of the internal deformity and clinical history of the patient. This is expected because the relationship between the internal deformity of the torso and

its external shape is complex and changing and dependent on such hard to model variables as body fat, rib-alignment, morphometry and posture [2], [4], [5].

The proposed system classifies the torso based on continuous 3D variables unlike existing methods of torso classification such as the Cosmetic Score [6], the Posterior Trunk Symmetry Index (POTSI) score [7], the Integrated Shape Imaging System (ISIS) score [8], and the Quantec score [9]. The orthogonal maps can be obtained quickly from torso scans. This is particularly important in the fast-paced environments of scoliosis clinics. Once the indices of deformity are computed, the classification of scoliosis can be automatically obtained and coupled with the classification of the internal spinal deformity. By using both the internal and external measures, confidence in the obtained status and classification of scoliosis patients will be increased.

5.6 CONCLUSIONS

This chapter presents the proof of concept of a technique for classifying the torso deformity associated with scoliosis based on indices obtained from orthogonal maps of the full torso. Results show that the technique is robust and clinically relevant. It yields detailed and overall assessments of torso deformity and a continuous measure of deformity and can be used to monitor the progression of scoliosis. Results obtained indicate that the technique is reliable.

Future work will focus on automating the process of computing the shape indices from the orthogonal maps and classifying scoliosis and verifying the results on a larger database of full torso scans. Future work will also focus on developing a three dimensional score for torso deformity based on novel mathematical models[5].

[5] This was achieved by developing the structured splines model. See Chapter 3.

REFERENCES

1. P. O. Ajemba, A. Kumar, N. G. Durdle, V. J. Raso, 'Quantifying torso deformity in scoliosis,' in *Proceedings of the SPIE*, Vol. 6144, 614450, 2006.
2. P. O. Ajemba, N. G. Durdle, D. Hill, V. J. Raso, 'A Torso Imaging System for Quantifying the Deformity Associated with Scoliosis,' in *Proceedings of the IEEE Instrumentation and Measurement Technology Conference*, Ottawa, 17–19 May, 2005.
3. P. O. Ajemba, N. G. Durdle, D. L. Hill, and V. J. Raso, 'A torso imaging system for quantifying the deformity associated with scoliosis,' *IEEE Transactions on Instrumentation and Measurements,* vol. 56, no. 5, October 2007.
4. C. J. Goldberg, M. Kaliszer, D. P. Moore, E. E. Fogarty, F. E. Dowling, 'Surface topography, Cobb angles and cosmetic change in scoliosis,' *Spine*, 26, pp E55–63, 2001.
5. J. L. Jaremko, P. Poncet, J. Ronsky, J. Herder, *et al.*, 'Indices of torso asymmetry related to spinal deformity in scoliosis,' *Clinical Biomechanics*, 17, pp. 559–568, 2002.
6. V. J. Raso, E. Lou, D. L. Hill, J. K. Mahood, M. J. Moreau, N. G. Durdle, 'Trunk distortion in adolescent idiopathic scoliosis', *Journal of Paediatric Orthopaedic*, 18(3), pp 222-26, 1998.
7. N. Suzuki, K. Inami, T. Ono, K. Kohno, M. A. Asher, 'Analysis of Posterior Trunk Symmetry Index (POTSI) in scoliosis: Part 1,' *In Research into Spinal Deformities 2*, 81-4, 1999.
8. A. R. Turner-Smith, J. D. Harris, G. R. Hougton, R. J. Jefferson, 'A method of analysis of back shape in scoliosis', *Journal of Biomechanics.*, 21, pp. 497–509, 1998.
9. X. C. Liu, J. G. Thometz, R. M. Lyon, J. Klein, 'Functional classification of patients with idiopathic scoliosis assessed by the Quantec system,' *Spine*, 26(11), pp. 1274-79, 2001.

CHAPTER 6

SHAPE ANALYSIS: POINT-SET DATA[N]

6.1 INTRODUCTION

The study of the external deformity associated with scoliosis pre-dates modern investigations of spinal deformity using radiographs [1]. Continued interest in the external deformity is justified by the fact that many patients worry more about their external shape than about their spinal deformity [2]. Also, many patients initially seek treatment for scoliosis because they are not satisfied with the appearance of their torsos and view improvement in torso shape as a measure of the success of scoliosis treatment [2].

Since the advent of the use of back shape imaging for the assessment of scoliosis (with systems such as Moiré topography [3]), several research groups have developed scores to quantify torso asymmetry based on indices like scapular angle differences and back surface rotation obtained from images of the back. These scores include: posterior trunk symmetry index (POTSI) [4], [5]; cosmetic score [6]; integrated shape imaging system (ISIS) index [7]; and Quantec score [8]. They are computed from indices that are not linearly independent basis vectors in shape space. This makes them untenable to multidimensional analysis of shape and asymmetry. Thus, it is very possible to see two patients who have the same deformity score and yet present widely different manifestations of torso asymmetry. There is a need to develop more descriptive measures of torso asymmetry based on multi-dimensional analysis of torso shape and asymmetry in shape space.

This chapter presents a technique for evaluating torso shape and asymmetry in

[N] A version of this chapter has been published. P. O. Ajemba, N. G. Durdle, and V. J. Raso, 'Evaluation of torso shape and asymmetry associated with scoliosis,' *Research into spinal deformities 6*, 2006.

scoliosis based on descriptors of the major features of torso deformity: twist, bend and asymmetry (Fig. 6.1). The descriptors are indices of point-set data obtained from torso surface scans.

Point-set data are the maximum curvature points of surface scans and contain key shape information. The centroids, distributions and densities of point-set data are indices of shape and asymmetry. The mean-squared deviations of the centroids per-cross-section from the medial axis are indicative of asymmetry. The distribution and density of point-set data are indicative of shape. The technique was modelled from 30 back shape scans of scoliosis patients and tested on another 18 back shape scans of scoliosis patients.

6.2 POINT-SET DATA

6.2.1 High curvature points

Edges and points of high curvature play an important role in the perception of shape. Research in human cognition and shape recognition suggest that when presented with objects, the human visual system pays much attention to points of high curvature [9]. Davis [10] developed an approach that detects angles and sides at various degrees of coarseness to construct a hierarchy of angles that describe the curve at any desired level of coarseness. The approach was to aid the incorporation of curvature information in descriptions of plane shapes. It can be extended to the description of 3D shapes by representing the 3D shapes by a finite set of cross-sections. In this chapter, high curvature points are called point-set data.

6.2.2 Application to assessing scoliosis

As human torso scans are 3D shapes, point-set data can be used to assess the torso shape and asymmetry associated with scoliosis. The range of deformity patterns

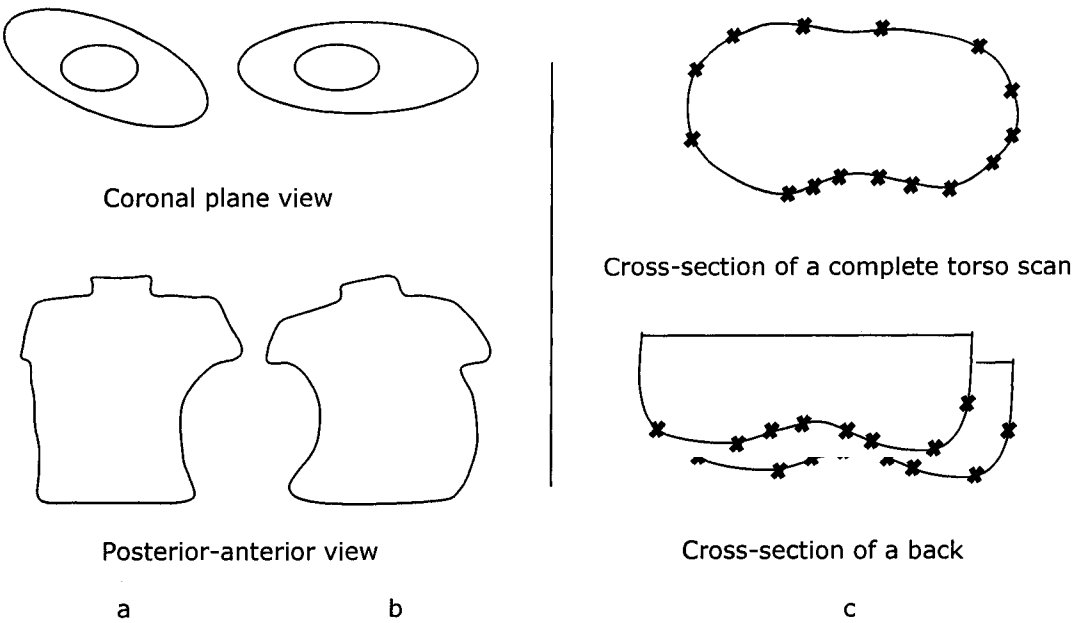

Fig. 6.1. A. Twisted torso shape. B. Bent torso shape. C. Points of high curvature on cross-sections of a complete torso scan and a back shape scan of a human torso.

produces various distributions of point-set data. The torso surface is divided into six regions (Fig. 6.2) and centroids of point-set data in each region computed. The difference between the mean-square deviations from the medial plane of the centroids in the two halves of the torso is a measure of asymmetry. The centroid distributions are indicative of overall twist and bend.

6.3 MATERIALS AND METHODS

Back shape scans of 30 female idiopathic scoliosis patients whose torso deformity run the gamut seen in our scoliosis database (containing over 1000 entries) were used to calibrate the deformity- and symmetry-space of the twist, bend and asymmetry indices. The patients were diagnosed as having idiopathic scoliosis and were between 10 and 18 years old (average age 14.5 years). Each index ranged from 0 to 10 with '0' corresponding to no deformity and '10' corresponding to the maximum found in our database. To obtain an overall score, the three indices were

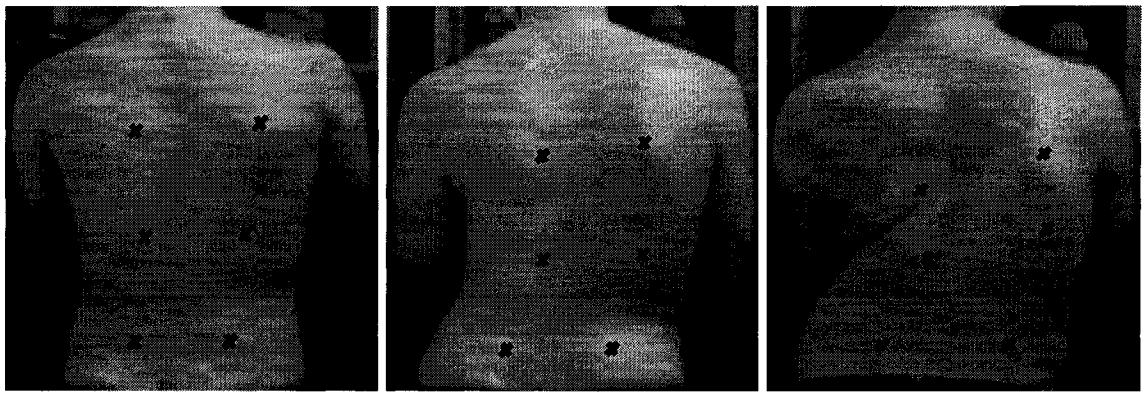

Fig. 6.2: Back shape views of (from left to right) mild, moderate and severe patients showing centroids of the distribution of point-set data of the six sections.

modeled as orthonormal vectors in 3D shape space. The deformity index was the Euclidean norm of the magnitude of the indices. Mild, moderate and severe torso deformity mapped to values of 1-3, 3-5 and 5-10 respectively.

To evaluate the correspondence of the technique to other measures of torso deformity like the cosmetic score [6], 18 torso scans of female scoliosis patients whose demographics matched the earlier group were selected from our scoliosis database (age range, 12-18 years; average age 14.9 years). The torso deformity present in the back shape scans were classified using the proposed technique and compared to the classification obtained using the cosmetic score.

6.4 RESULTS

Table 1 shows the results obtained from classifying 18 scans of female scoliosis patients based on the distribution of their point-set data and a comparison with the cosmetic score classification. Evaluations using point-set data indices were 100% in accord with those based on the cosmetic score. Indices of point-set data have more degrees of freedom and were able distinguish between scans that have similar cosmetic scores. They are a superset of clinical descriptions like the cosmetic score.

Table 6.1: Classification of back shape scans of 18 female scoliosis patients

	Age	Cosmetic Score		Point-set Data	
		Score	Classification	Score	Classification
1	14.1	1.0	Mild	1.0	Mild
2	13.8	1.0	Mild	2.3	Mild
3	13.3	1.1	Mild	1.2	Mild
4	14.2	1.5	Mild	2.3	Mild
5	18.0	1.6	Mild	2.5	Mild
6	17.0	1.8	Mild	2.2	Mild
7	15.1	1.9	Mild	1.6	Mild
8	14.6	1.9	Mild	1.8	Mild
9	15.0	1.9	Mild	2.6	Mild
10	14.8	2.1	Moderate	4.4	Moderate
11	12.8	2.5	Moderate	4.3	Moderate
12	14.4	2.6	Moderate	4.7	Moderate
13	17.4	3.1	Moderate	3.6	Moderate
14	16.2	3.1	Moderate	3.7	Moderate
15	12.7	3.3	Moderate	3.8	Moderate
16	16.1	3.4	Severe	6.5	Severe
17	13.8	3.5	Severe	6.3	Severe
18	16.4	4.9	Severe	7.1	Severe

6.5 DISCUSSION

The proposed technique can be used on back shape data (as in this paper) or on complete torso data [11]. The classifications obtained were in accord with a classification based on the cosmetic score. As shape and asymmetry characterize the external deformity of scoliosis, the technique could be applied to monitoring changes in torso shape in progressive scoliosis. Future work will focus on validating the technique on a larger dataset of patients.

REFERENCES

1. M. A. Hoke, 'A study of a case of lateral curvature of the spine: report on an operation for the deformity,' *American Journal of Orthopaedic. Surgery*, vol. 1, pp 168-208, 1903.

2. R. A. Dickson, 'Spinal Deformity–Adolescent Idiopathic Scoliosis: Nonoperative Treatment,' *Spine*, vol. 24, no. 24, pp 2601-2606, 1999.
3. M. S. Moreland, M. H. Pope, D. G. Wilder, I. A. Stokes, and J. W. Frymoyer, 'Moire fringe topography of the human body,' *Medical Instrumentation*, vol. 15, pp 129-132, 1981
4. N. Suzuki, K. Inami, T. Ono, K. Kohno, M. A. Asher, 'Analysis of Posterior Trunk Symmetry Index (POTSI) in scoliosis: Part 1,' *In Research into Spinal Deformities 2*, 81-84, 1999.
5. K. Inami, N. Suzuki, T. Ono, Y. Yamashita, K. Kohno, H. Morisue, 'Analysis of Posterior Trunk Symmetry Index (POTSI) in scoliosis: Part 2,' *In Research into Spinal Deformities 2,* 85-88, 1999.
6. D. L. Hill, J. K. Mahood, M. J. Moreau, V. J. Raso, N. G. Durdle, 'The scoring of Trunk Distortion in Scoliosis,' *In Research into spinal deformities 1*, JA Sevastik and KM Diab (Eds.) IOS Press, 1997.
7. I. Weisz, R. J. Jefferson, A. R. Turner-Smith, G. R. Houghton, J. D. Harris, 'ISIS scanning: a useful assessment technique in the management of scoliosis,' *Spine*, vol. 13, pp 405-408.
8. C. J. Goldberg, M. Kaliszer, D. P. Moore, E. E. Fogarty, and F. E. Dowling, 'Surface Topography, Cobb angles and cosmetic change in scoliosis,' *Spine*, vol. 26, pp E55-63, 2001.
9. F. Attneave, 'Some Informational Aspects of Visual Perception,' *Psychological Review*, 61(3), 183-193, 1954.
10. L. S. Davis, 'Understanding Shape-Angles and Sides,' *IEEE Transactions on Computers*, vol. 26, no. 3, 236-242, 1977.
11. P. O. Ajemba, N. G. Durdle, D. L. Hill, and V. J. Raso, 'A torso imaging system for quantifying the deformity associated with scoliosis,' *IEEE Transactions on Instrumentation and Measurements,* vol. 56, no. 5, October 2007.

CHAPTER 7

TORSO IMAGING SYSTEM: IMAGE ACQUISITION[N]

7.1 INTRODUCTION

In this chapter, we present a low-cost torso imaging system for quantifying the deformity associated with scoliosis. The system has image-capture and image-analysis components. The image-capture component obtains full-torso scans using a rotating positioning platform and one or two 3D surface digitizers (Fig. 7.1). The image analysis component is based on a commercial visualization toolkit and assesses the shape of the torso from torso scans. We describe the system architecture and possible configurations and present the results of system calibration and error analysis (accuracy of reproduction based on tests on inanimate objects and human subjects). Finally, we discuss the use of maps obtained from torso scans in quantifying the deformity associated with scoliosis.

7.2 THEORETICAL BACKGROUND

7.2.1 Image capture

A rotating positioning platform and one or two laser digitizers (cameras) are needed.

1. One-Digitizer Configuration: This is based on the ideas that: 1) four shots of an object taken at right-angles to each other will effectively capture the full 360^0 view of the object; 2) it is possible to generate a full-torso scan from four orthogonal partial-scans using image matching techniques; and 3) errors associated with the image-capture and matching procedures are either acceptable or can be compensated for.

[N] A version of this chapter has been published. P. O. Ajemba, N. G. Durdle, D. L. Hill, and V. J. Raso, 'A torso imaging system for quantifying the deformity associated with scoliosis,' *IEEE Transactions on Instrumentation and Measurements*, vol. 56, no. 5, October 2007.

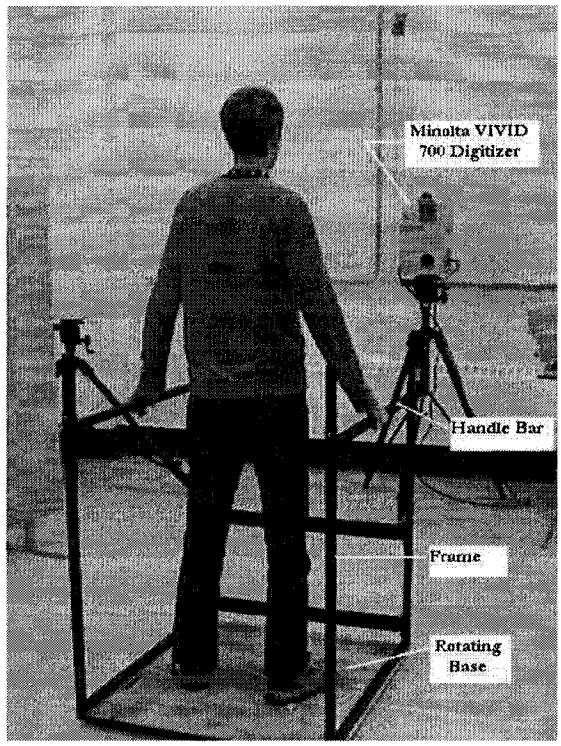

Fig. 7.1: The Minolta 700 surface digitizer system and rotating positioning platform

Details of the technique can be found in [1] and [2]. In brief, the cameras are fixed and the positioning platform is rotated after each step. The four range images obtained from each position are converted into mesh objects and stitched together to form full-torso scans using image registration techniques [3]. In regions of overlap between the meshes (a 30% overlap typically exists), spline interpolation is used to produce the approximate surface.

2. Two-Digitizer Configuration: An additional assumption particular to this configuration is that the simultaneous use of two digitizers, rather than one, will reduce errors due to patient re-positioning (sway and breathing) and motion artifacts [1] as the *average scan* obtained from the two cameras would have less variance than the scans obtained from either camera [4]. By combining scans from the two cameras, the time difference between the four scans used in the image synthesis is

reduced to one rotation[1], rather than the three rotations obtained with the single camera system.

The number of unique arrangements of two cameras in four positions around a circle is 2. Fig. 7.2 shows the two arrangements. Four partial scans corresponding to the front, back and sides of the scanned object are needed to construct a full-torso image in both arrangements.

7.2.2 Image analysis

The image analysis model is based on 3D spline-based models—spline objects, that consist of a series of m latitudinal and k longitudinal closed spline curves, $\mathbf{S}_c$ and $\mathbf{S}_l$ respectively, given as:

$$\mathbf{S}_c = \sum_{j=0}^{m-1} \zeta_j^c(t) = \sum_{j=0}^{m-1} \sum_{i=0}^{n-1} \alpha_{i,j}^c(t)\mathbf{P}_{i,j}, \tag{2.1}$$

$$\mathbf{S}_l = \sum_{j=0}^{k-1} \zeta_j^l(t) = \sum_{j=0}^{k-1} \sum_{i=0}^{n-1} \alpha_{i,j}^l(t)\mathbf{P}_{i,j}, \tag{2.2}$$

where $\zeta_j^c(t)$ and $\zeta_j^l(t)$ are the latitudinal and longitudinal cross-sectional closed spline curves respectively and $\mathbf{P}_{i,j}$ are the control points of spline curve i. $\alpha_{i,j}^c$ and $\alpha_{i,j}^l$ are spline basis functions. The numbers m and k and the positions of spline curves vary with application. The longitudinal splines curves could be made to pass through prominent anatomical landmarks on the torso by making the control points $\mathbf{P}_{i,j}$ coincide with those landmarks. For this study, we use evenly spaced curves along the length of the torso.

Definition 1: Let β represent a transformed version of a spline object γ such that each of the closed spline curves in γ is transformed into an open spline curve in

[1] This is achieved by using the first and second scans of both digitizers. The first scans of both digitizers are taken simultaneously as are the second scans of both digitizers.

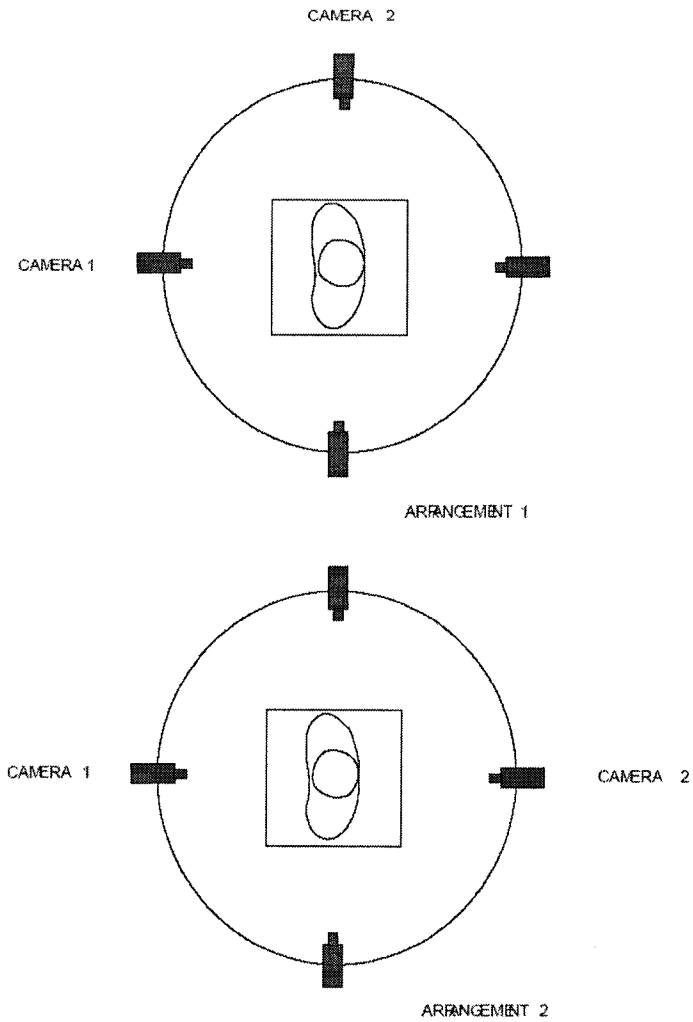

Fig. 7.2: The two arrangements for the two camera configuration

β by applying a transformation T. Then, the object β made up of a series of modified spline curves is called a modified spline object. β could be referred to as the *open equivalent* of spline object γ.

To quantify the shape of a torso, a spline object is generated and transformed into its *open equivalent* modified spline object. In this study, T transforms the spline curves of the spline object into an *open equivalent* curve by plotting the distances from the centroids of each spline curve to locations on the surface of the curve as a

function of its sector angle (formed by lines joining the centroid to the points on the surface) (Fig. 7.3). To compare two torso scans (A and B) of the same individual taken at different times (or torso scans of two different individuals), spline objects with equal numbers of horizontal closed spline curves are obtained and transformed into their equivalent modified spline objects. The graphs obtained from the open spline objects are subtracted to produce a difference surface. The difference surface provides a quantitative and visual assessment of differences between the subtracted torso surfaces.

7.3 MATERIALS AND METHODS

Scans of a test-box (of dimensions $300\times150\times200mm^3$; machined to an accuracy of 1mm and measured to a precision of 0.1mm) and a plaster cast (made from a cast of the torso of a scoliosis patient) were used to assess the accuracy of the image capture system. Analyses were performed to: 1) assess the accuracy of reproduction of the dimensions and aspect ratios of the sides of the test-box; 2) assess the effect of misaligning partial scans of the test-box; and 3) assess the effect of using one or two cameras on the accuracy of reconstruction of a plaster cast.

To assess the accuracy of reproduction of the dimensions and aspect ratios of the test-box, ten complete scans of the box were obtained using a single laser camera (Minolta VIVID™ 700 Digitizer[2]) with the box repositioned after each scan. Five of these scans were taken with the sides of the box perpendicular to the line of sight of the digitizer. The other five were taken with the sides at an angle of 45^0 to the line of sight of the digitizer. The lengths, widths and heights of the reconstructed image of the test-box were measured from each scan. The values of the three aspect ratios of the test-box (length-width, length-height and height-width) were obtained. The root

[2] Konica-Minolta Inc., Mahwah, NJ, USA.

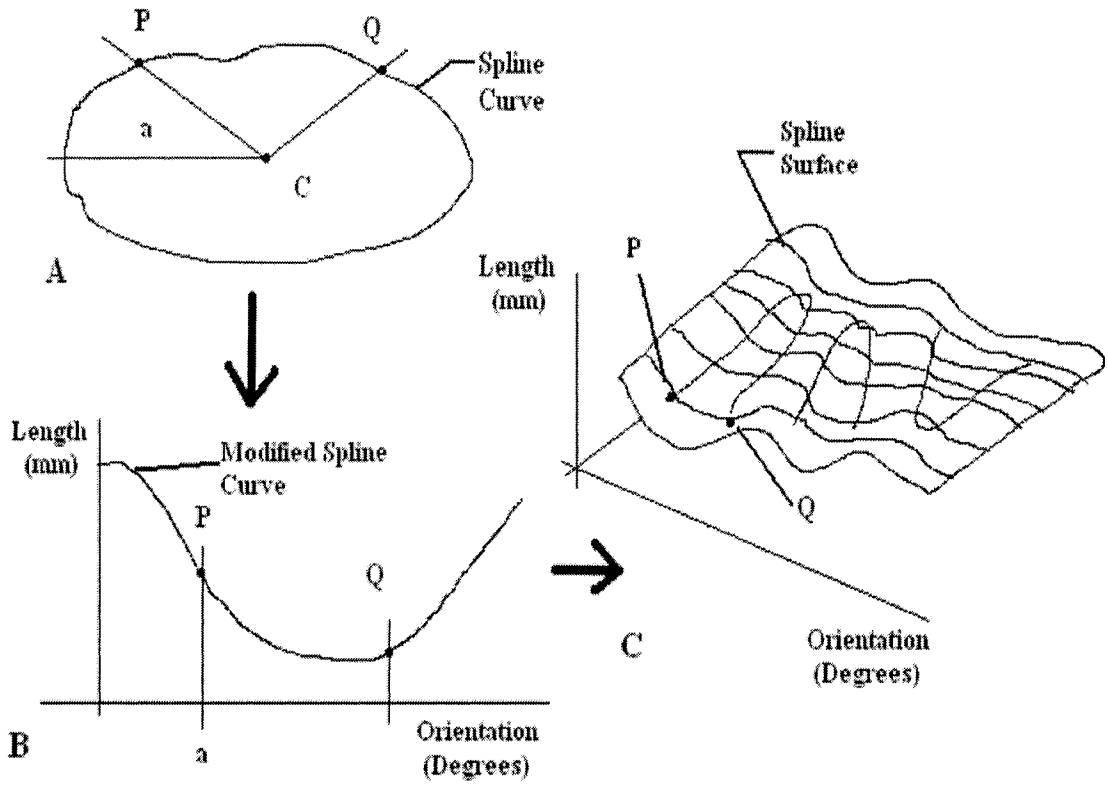

Fig. 7.3: Obtaining a spline surface. A: A cross-section modeled as a spline curve. B: Open equivalent of A. C: A spline surface obtained from a series of open equivalent spline curves.

mean square errors and the standard deviations in the dimensions and aspect ratios of the test-box were calculated. Errors here refer to the difference between the measured and actual values of the dimensions and aspect ratios.

To assess the effect of aligning the partial scans of the test-box to an angle different from 90^0 on its reconstruction accuracy, scans of the test-box were obtained from partial scans aligned by 80, 82.5, 85, 87.5, 90, 92.5, 95, 97.5 and 100^0 from each other. The volumes of the models created from misaligned partial-scans of the test-box were determined. The accuracy of reconstructing the models was assessed by comparing their volumes to that of the box. In general, smaller error in the volume of the reconstructed model implied a higher reconstruction

accuracy[3]. A plot of alignment error versus reconstruction accuracy was obtained (Fig. 7.4). For any given value of reconstruction accuracy, a *maximum tolerable error of alignment* could be ascertained from the plot. The *maximum tolerable error of alignment* is the largest value of alignment error that would produce a scan whose accuracy is less than or equal to the specified reconstruction accuracy.

To compare the effect of using one camera operating alone to two cameras operating in parallel (with regards to the accuracy of reconstruction of a test object), ten scans of a plaster model of a human torso were obtained using each of the two cameras individually. Ten other scans of the plaster cast were obtained from the two cameras at once (the cameras were placed opposite each other as in Arrangement 2 of Fig. 7.2). The lengths of the range images were computed and their standard deviations calculated.

An integrated software package based on an AVS/Express[4] shell provided the visualization platform for the image analysis component of the system. Proprietary software developed by our group and running as scripts off the shell performed tasks such as computing cross-sections of torso scans, calculating points $\mathbf{P}_{i,j}$ ((1) and (2)), deriving *spline surfaces* and computing *difference surfaces* from the *spline surfaces*[5]. Two scans of the bare torso of a 22-year old male volunteer who has no scoliosis or any other spinal deformity were obtained within one hour of each other. The volunteer was allowed to move around freely between scans. *Spline* surfaces comprising 40 latitudinal and 40 longitudinal cross-sections were computed from the scans and subtracted to generate a *difference surface*. The variation in the scans was assessed using the *difference surface* obtained.

---

[3] The reconstruction accuracy of the surfaces of the box (assessed by computing the standard deviation of the individual surface points from their ideal positions) was less than the reconstruction error (1mm).
[4] Advanced Visual Systems Inc., USA

[5] This is done by subtracting one *spline surface* from another. The second *spline surface* may be generated from another image of the same individual taken at a different time or may belong to another individual.

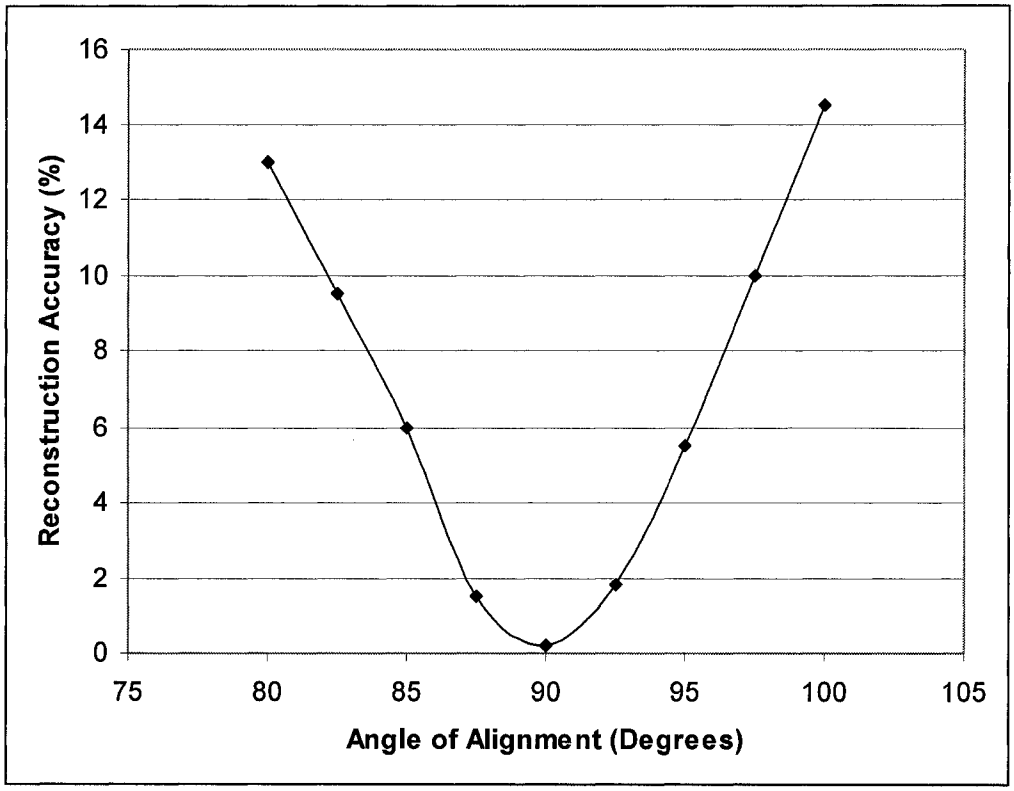

Fig. 7.4: Reconstruction accuracy as a function of the angle of alignment

7.4 RESULTS

Table 7.1 shows the root mean square errors and standard deviations in the dimensions of the sides of the test-box. Overall the dimensions of the test-box varied by 1-2%. Scans obtained with the sides of the test-box at an angle of 45^0 to the line of sight of the camera showed more variation than scans obtained with the sides of the test box perpendicular to the line of sight of the camera. Table 7.2 shows the root mean square errors and the standard deviations in the aspect ratios of the test-box. Overall the aspect ratios of the test-box varied by 1-3%. The orientation of the test-box also significantly influenced the variations in the aspect ratios of the scans obtained as higher variations were obtained for scans taken with the sides of the box at an angle of 45^0 to the line of sight of the camera.

Table 7.1: RMS and SD error in the dimensions of the test-box

	90^0 to digitizer line-of-sight			45^0 to digitizer line-of-sight		
	Mean	RMS Error	SD	Mean	RMS Error	SD
Length	299.9	0.8	0.9	300.2	1.8	1.9
Width	150.1	0.8	0.9	149.6	2.1	2.1
Height	199.9	0.9	1.0	200.7	2.1	2.2

RMS = root mean square; SD = standard deviation; sample size = 20.

Table 7.2: RMS and SD error in the aspect ratios of the test-box

	90^0 to digitizer line-of-sight			45^0 to digitizer line-of-sight		
	Mean	RMS Error	SD	Mean	RMS Error	SD
L/W	2.0000	0.0054	0.0059	2.0075	0.0255	0.0291
L/H	1.5000	0.0038	0.0040	1.4975	0.0134	0.0129
H/W	1.3300	0.0039	0.0039	1.3400	0.0232	0.0228

RMS = root mean square; SD = standard deviation; L = length; W = width; H = height; sample size = 20.

Figure 7.4 shows a plot of the reconstruction accuracy (defined as the percentage difference between the volume of the reconstructed scan and the actual volume of the test-box) as a function of the angle of alignment of the partial scans. The *maximum tolerable error of alignment* was 5^0 for reconstruction accuracy of 5%. Thus, barring other errors, the system could reconstruct an object to an accuracy of at least 5% if the partial scans were set-off by an angle between 85 and 95^0. As the design of the system almost certainly precludes the possibility of misaligning the partial scans by up to 5^0, the *maximum error of alignment* of the system was 2%.

Table 7.3 shows the standard deviations in the values of the lengths of ten evenly spaced cross-sections of the plaster cast obtained using each of the two cameras (Digitizers A and B) alone and both digitizers simultaneously. The cross-sections were numbered in increasing order from the waist of the cast upwards. The standard deviations in the lengths of the first few cross-sections (close to the waist of the cast) were lower than those of later cross-sections. This was due to persistent errors

Table 7.3: RMS and SD error in the aspect ratios of the test-box

	Standard Deviation		
	Digitizer A	Digitizer B	Digitizers A and B
1	0.64	0.58	0.47
2	0.83	0.75	0.67
3	0.92	0.83	0.75
4	1.04	1.14	0.98
5	1.12	1.03	0.95
6	1.06	1.04	0.94
7	1.06	1.10	0.93
8	1.12	1.01	0.94
9	1.16	1.06	0.99
10	1.71	1.82	1.04

in aligning the central axis of the cast to the line of sight of the camera. These errors were introduced by the positioning platform and are entirely a function of the setup of the experiments. The standard deviations in the lengths of the cross-sections obtained from the two-camera scans were less than that of the one-camera scans.

Fig. 7.5 shows a plot of one of the spline surfaces obtained from the male volunteer. The *spline* and *difference surfaces* were divided into five regions: chest, stomach, right scapula, left scapula and back for the purpose of analysis. The difference surface showed a maximum average variation of 4mm in each section. Most of the point-by-point differences observed were attributable to errors caused by patient re-positioning and are less than the size of anatomical landmarks on the torso.

7.5 DISCUSSION AND CONCLUSIONS

A full torso imaging system based on surface digitizers and a rotating positioning platform was described. The system consisted of image capture and image analysis components and required four partial scans set-off at 90^0 to produce a full scan.

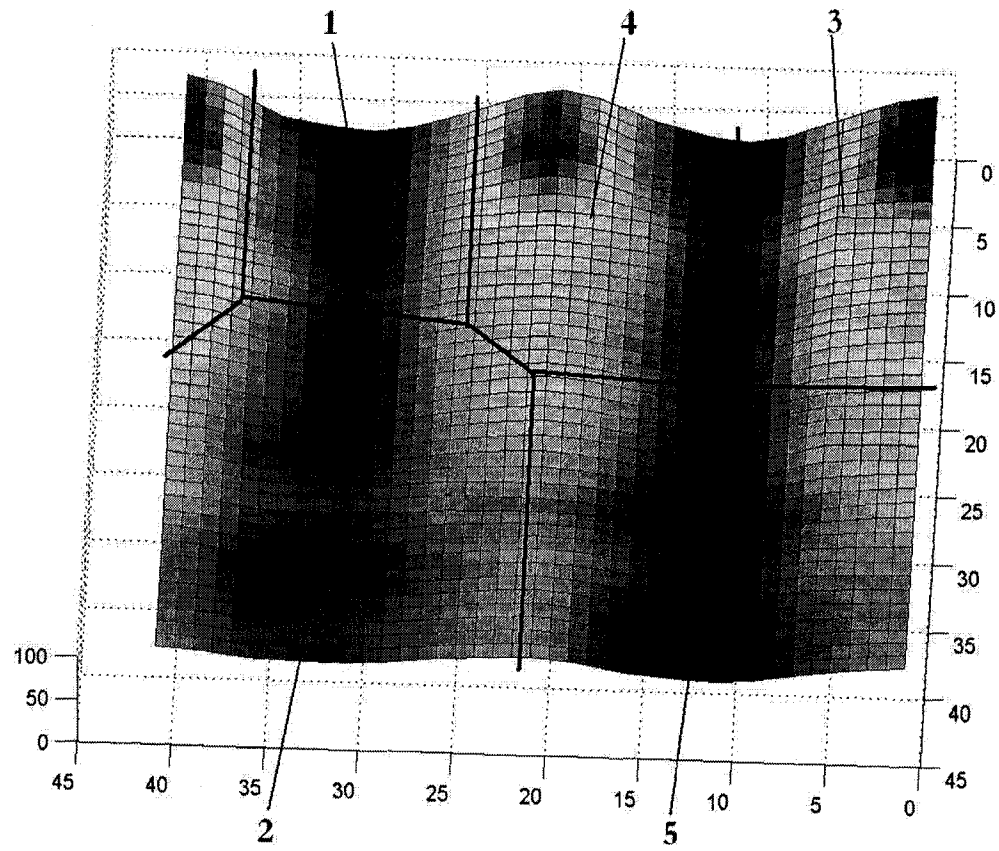

Fig. 7.5: Orthogonal surface obtained from torso scans of a male volunteer. The surface was divided into 5 sections: 1: Chest; 2: Stomach; 3: Right scapula; 4: Left scapula; 5: Spine.

Several models of a test-box were used to assess the reconstruction accuracy of the system's image capture component. The dimensions and aspect ratios of the models of the test-box obtained varied by less than 3%.

Several models of a plaster cast of an actual scoliosis torso were obtained and analyzed to quantitatively compare the image capture component of the one-camera to that of the two-digitizer configuration. Variations of 1-3% were observed. This was comparable to results obtained from our previous work [1]. In [1], the maximum variations in the dimensions of models obtained from five volunteers were found to be less than 4%. The higher error value was attributed to errors caused by sway and

breathing. As expected, errors associated with the two-digitizer configuration were lower than those associated with the one-digitizer configuration.

These results indicate that the system can be used to create acceptable models of the torso. It can also be used to quantify and describe the torso deformity caused by scoliosis from analysis of torso scans of scoliosis patients. A limitation of the system is that two fairly skilled people are needed for its operation. Future work[6] will focus on creating more elaborate mathematical models for analyzing, quantifying and classifying torso deformity.

REFERENCES

1. P. O. Ajemba, N. G. Durdle, D. L. Hill, and V. J. Raso, 'Re-positioning Effects on a Full Torso Imaging System for the Assessment of Scoliosis,' *Proceedings of the 2004 IEEE Canadian Conference on Electrical and Computer Engineering*, Niagara Falls, Canada, May 2-5, 2004.
2. P. O. Ajemba, N. G. Durdle, D. L. Hill, and V. J. Raso, 'Effect of Posture on a Full Torso Imaging System for the Assessment of Scoliosis,' *Proceedings of the 2004 Conference of International Research Society for Spinal Deformities*, Vancouver, Canada, June 10-12, 2004.
3. P. Poncet, S. Delorme, J. L. Ronsky, J. Dansereau, G. Clynch, J. Harder, R. D. Dewar, H. Labelle, P. Gu, and R. F. Zernicke, 'Reconstruction of Laser-scanned 3D Torso Topography and Stereoradiographical Spine and Rib-cage Geometry in Scoliosis' *Computer Methods in Biomechanics and Biomedical Engineering*, vol. 4, pp 59-75, 2000.
4. C. J. Goldberg, E. E. Fogarty, D. P. Moore, and F. E. Dowling, 'Scoliosis Imaging and the Problem of Postural Sway' *in Sevastik, J. A and Khaled, M. D. (Eds.) Research into spinal deformities 1: (IOS Press, Oxford)*, 1997.

[6] This was achieved by developing the structured splines model. See Chapter 3.

CHAPTER 8

TORSO IMAGING SYSTEM: PRE-PROCESSING [N]

8.1 INTRODUCTION

This study presents a procedure for pre-processing range images used in the assessment of torso deformities. The procedure includes an interactive technique for clipping stray points and extremities and a novel interpolation technique for filling holes and correcting for surface errors. Contributions of this chapter include four indices for validating the reconstruction accuracy obtained from pre-processing range images. However, its most important contribution is putting together the different pre-processing operations into an easy to apply procedure.

8.1.1 Previous work

The problem of filling holes in 3D images is not new. Past work on hole-filling and edge completion encompass those applied to content-based [1] and feature-based images [2]. Methods applied to content-based images are beyond the scope of this chapter. The basic idea of interpolating a set of points to obtain a curve or surface can be viewed as a limiting case of hole-filling a feature-based image in the form of a silhouette with a hole occurring between every two consecutive points. A variety of methods have been used for hole filling, including spline-based techniques such as *B*-splines [3], Bezier curves [4], Beta curves [5] and T-splines [6]. Uniform versus non-uniform and rational and non-rational formulations have been used (for example, NURBS [7]). Radial basis functions [8] have also found some use in hole-

[N] A version of this chapter has been submitted for publication. P. O. Ajemba, A. Kumar, N. G. Durdle, and V. J. Raso, 'Range data pre-processing and reconstruction for the analysis of torso images in scoliosis,' *IEEE Transactions on Information Technology in Biomedicine*, 2006.

filling. Splines enable an arbitrary degree of smoothness or curvature to be achieved and make use of nearby points to estimate the filled curve or surface[1]. The underlying assumption for their use is that the degree of smoothness of the missing part is known.

Allen *et al.* [8] used a technique that roughly approximates the human body surface to fill holes in range images of human body parts. They produced good reconstructions that can be used for applications primarily concerned with the anthropometric relationships of body parts. However, for applications that employ surface or cross-sectional images of the human body for medical diagnosis, such glib approximations are unacceptable as the roughness of a cross-section, for instance, may be a factor in the prognosis of a disease or condition. Model fitting [9] used to estimate surfaces from range images, has been used for hole-filling by elastically deforming an ideal model to the desired shape [10]. The moving least squares (MLS) projection procedure which minimizes the sum of squared Euclidean distances of surfaces [11] has also been used to represent surfaces by clouds of points.

In the presence of large holes, arbitrarily aligned extremities and a significant amount of stray points, a comprehensive pre-processing and reconstruction procedure is needed for clinical applications.

8.1.2 Overview

The pre-processing and reconstruction procedure described in this chapter consists of three stages: torso cross-sectioning and clipping, torso hole filling and sub-sampling, and torso surface re-generation (Fig. 8.1). The first stage comprises of torso clipping (cropping the extremities) and torso cross-sectioning (sectioning the torso into some number of cross-sections defined by the user[2]). The torso clipping routine uses an

[1] All the points in the Bezier curve method are control points that are not necessarily interpolated.

[2] The sections are usually evenly spaced but division into a number of equal volume segments is possible.

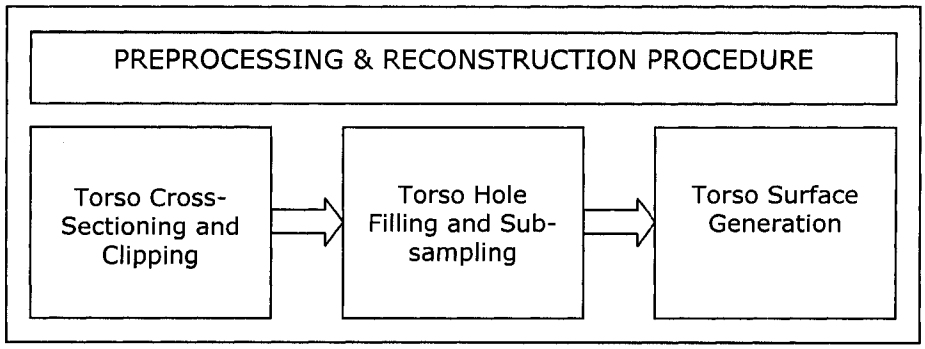

Fig. 8.1: Flow chart of the preprocessing and reconstruction procedure.

implementation of the Sutherland-Hodgman polygon clipping algorithm [12]. An enhancement detects the boundary points of the extremities and holes in the torso using a *convexity* algorithm. A *hole* is defined as a region in the torso cross-section where the two nearest points on the plane are not connected by a line segment. At the end of the torso clipping and cross-sectioning stage, much of the surrounding artefacts that are not part of the image are removed.

The points in each cross-section are evaluated to fill holes in the 3-D scan in the hole filling stage. Once a hole is detected, depending on its size, a decision is made to either connect the two nearest points to it to fill it directly or to generate intermediate points to fill it by interpolation. The sub-sampling and surface generation stage re-samples the sets of cross-sectional points into a user-defined number of evenly spaced points per cross-section. The sets of points are resampled using *B*-spine interpolation. The resulting points are triangulated and rendered to generate the filled surface.

8.2 THEORETICAL BACKGROUND

The novel approximation procedure proposed in this chapter, the spline-fitted moving least squares (SMLS) procedure, utilizes the Bezier curve (BC) approximation theory and the moving least squares (MLS) projection theory. The MLS projection theory is

based on the MLS approximation theory. The theoretical backgrounds to MLS and BC approximation are given in appendix III.

In this chapter, the SMLS procedure is defined in 2D as it is applied to fill holes in cross-sections of the torso but it can easily be extended to 3D[3]. The procedure consists of a first pass involving spline fitting with BC approximation that yields the approximate positions of the intermediate points and a second pass during which the positions of the intermediate points are refined using MLS projection.

Let p_1, p_2, p_3 and p_4 be four consecutive points on a cross-sectional plane Q with a constant z coordinate, such that $p_i \in R^3$ $\{i=1, 2, 3, 4\}$ with rectangular coordinates (p_{ix}, p_{iy}, p_{iz}). In this case, p_{iz} is constant for all i. Let the part of the connectivity map of Q containing p_1 to p_4 be given by $\{\ldots p_1 \leftrightarrow p_2 \circ p_3 \leftrightarrow p_4 \ldots\}$ where $p_1 \leftrightarrow p_2$ denotes that p_1 and p_2 are connected and $p_2 \circ p_3$ denotes that there is a hole (or disconnection) between p_2 and p_3. Let the mean Euclidean distance between all the connected pairs of points in the connectivity map of Q be given by

$$MD = \sum_{i=1}^{C-1} \left(\frac{\sqrt{(p_{(i+1)x} - p_{ix})^2 + (p_{(i+1)y} - p_{iy})^2}}{C-1} \right),$$

where C is the total number of points in the connectivity map of the cross-section and i is the index of one such point p. Finally, let the standard deviation of the distribution of Euclidean distances between connected points in the connectivity map be σ[4]. If the Euclidean distance between p_2 and p_3 is less than or equal to $MD + 2 \cdot \sigma$, then the hole can be filled by drawing a line between p_2 and p_3. If the

[3] This is achieved by working with the cross-sections in an increasing order of position. For all cross-sections apart from the first, the previous section serves as a rough estimate of its shape.

[4] The distribution of distances between neighboring points for this application is generally skew-symmetric.

distance is greater than $MD + 2 \cdot \sigma$, the SMLS approximation procedure is invoked. In the first pass, asymptotes joining p_1, p_2 and p_3, p_4 are defined respectively as

$$y - p_{1y} = \frac{p_{3y} - p_{1y}}{p_{3x} - p_{1x}}(x - p_{1x}) \text{ and } y - p_{2y} = \frac{p_{4y} - p_{2y}}{p_{4x} - p_{2x}}(x - p_{2x}). \quad (1)$$

The point of intersection of these two asymptotes is denoted as $p_5 \in R^3$ (Fig. 8.2) where:

$$p_{5x} = \left(\frac{(p_{2y} - p_{1y})(p_{3x} - p_{1x})(p_{4x} - p_{2x}) - p_{1x}(p_{3y} - p_{1y})(p_{4x} - p_{2x}) - p_{2x}(p_{4y} - p_{1y})(p_{3x} - p_{1x})}{(p_{3y} - p_{1y})(p_{4x} - p_{2x}) - (p_{4y} - p_{2y})(p_{2x} - p_{1x})} \right),$$

$$p_{5y} = \left(\frac{p_{3y} - p_{1y}}{p_{3x} - p_{1x}} \right)(p_{5x} - p_{1x}) + p_{1y},$$

$$p_{5z} = p_{iz}.$$

Also, $i = 1, 2, 3, 4$. Two new 3D points $p_6, p_7 \in R^3$ are constructed from p_2, p_3 and p_5 such that

$$p_6 = \left(\frac{p_2 + p_5}{2} \right) \text{ and } p_7 = \left(\frac{p_3 + p_5}{2} \right).$$

The four points p_2, p_6, p_7 and p_3 then become the edges of the control polygon of a BC that provides a rough interpolate of $p_2 \circ p_3$. The parametric equation of the BC is

$$p(t) = (1-t)^3 * p_2 + 3*(1-t)^2 * t * p_6 + 3*(1-t) * t^2 p_7 + t^3 * p_3, \quad (2)$$

where $0 \le t \le 1$ and $p(t) = (x(t), y(t), z(t))$. An initial t value is chosen for (2) starting from p_1. To determine the location of the intermediate points between p_2 and p_3, t is varied at equal intervals of length in a series $\{t, 2t, 3t, \ldots, It\}$, where $I \in Z$ is the total number of intermediate points required between p_2 and p_3 and is a function of the ratio of MD to the distance between the points . Let the control point distance $CPD \in R$ be the sum of the Euclidean distances between p_2 and p_6,

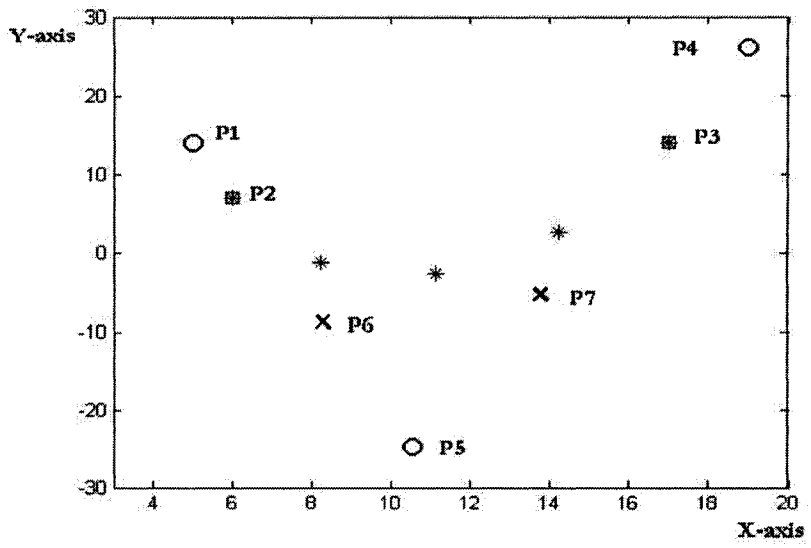

Fig. 8.2: Interpolating a hole (P2 ∘ P3) using the SMLS method. P5 is the intersection of lines P1 ↔ P2 and P3 ↔ P4. P6 and P7 are intermediate points. The *s are the interpolated points.

p_6 and p_7, and p_7 and p_3 such that

$$CPD = \sqrt{(p_{6x} - p_{1x})^2 + (p_{6y} - p_{1y})^2} + \sqrt{(p_{7x} - p_{6x})^2 + (p_{7y} - p_{6y})^2} + \sqrt{(p_{2x} - p_{7x})^2 + (p_{2y} - p_{7y})^2}.$$

In the second pass, the SMLS procedure is implemented using either of two methods. In the first method $X \in Z \approx CPD / MD$. The number of intermediate points computed at this stage is given by $I = (X - 1)$ where $t = 1/I$ is a parametric operator that varies from 0 to 1 at equal intervals. The ensuing SMLS construction yields a number of intermediate points P which have an average spacing of MD. The points in P provide better approximation using bivariate local polynomials and smoothing using radial Gaussian weights.

In the second method $X \in Z \approx Integer(CPD)$. The key difference between this method and the first is that this ensures that the average distance between the intermediate points created by the BC equation is one unit. In this case, the SMLS procedure assumes that the number of intermediate points is greater than what is

required to correctly fill the gap as MD is usually greater than double the distance between the intermediate points. I and t are defined as in the previous method. Let $P = \{p_2, p_t, p_{2t}, p_{3t}, \ldots, p_{It}, , p_3\}$ be the set of points obtained. P_{SEL}, a subset of P containing enough key control points[5] to make the mean distance MD, is obtained by iteration and yields the final set of interpolants of $p_2 \circ p_3$. This approach is slower but more accurate than the first and is used in our implementation.

8.3 IMPLEMENTATION

8.3.1 Torso clipping and cross-sectioning

The torso image is aligned such that its medial axis is parallel to the vertical axis of the imaging plane. The upper extremities (the regions of the image above the base of the neck) and the lower extremities (the regions of the image below the waist) are cropped using a horizontal cutting plane implemented using the Sutherland-Hodgman plane clipping algorithm [12]. The coefficients of the cutting planes in the neck and waist (p_{ny} and p_{wy} respectively) are user-defined and delineate the extent of the crop. As the human torso is usually asymmetric, the left and right extremities rarely attach to the torso in planes parallel to the torso medial plane[6]. This makes it difficult to automatically crop the left and right extremities of most torsos using a plane clipping algorithm. A semi-automatic cropping regime using a box or sphere clipper that clips the parts of the image that lie within its boundaries is preferable.

In this chapter, the left and right extremities are clipped using an implementation of the Sutherland-Hodgman box clipping algorithm (see Fig. 8.3). For every instance of the box clipper, four variables $p_{ix(MIN)}$, $p_{iy(MIN)}$, $p_{ix(MAX)}$ and $p_{iy(MAX)}$ (where i is

[5] Key control points whose removal from the curve perceptibly changes the shape of the curve.

[6] The degree of misalignment of the left and right extremities is reflective of torso asymmetry.

the instance of the box clipper) that delineate the extent of the boundaries of the box in the $X-Y$ plane, are user-defined. The box is assumed to have an infinite depth.

The implementation of SMLS is preceded by a cross-sectioning stage. The number of cross-sections and the region of the torso to be sectioned is also user-defined. A vertex array and a connectivity map are obtained for each cross-section. The vertex array is a $N \times 3$-dimensional array that stores the physical locations of each point in the cross-section. The vertices in the vertex array are numbered in a generally counter-clockwise loop starting from the left-most point in the plane orthogonal to the medial axis of the image. The connectivity map is an array sequence that shows the connections between the N points in the vertex array and their neighbours. For example, $\{\ldots p_1 \leftrightarrow p_2 \circ p_3 \leftrightarrow p_4 \ldots\}$ shows that p_1 and p_2 are connected but p_2 and p_3 have a hole (or disconnection) between them.

To obtain a cross-section at a height p_{oy}, the data points near the height are contoured and the boundaries between regions are interpolated to generate an isosurface. These boundaries correspond to contour surfaces of a constant scalar value (in this case p_{oy}). Contouring begins at p_{oy} and usually requires interpolation because most of the points will not be exactly located on the user-defined contour. Linear interpolation along the edges is used to generate points on contour surfaces that are stored in the vertex array. Once the points on the edges are generated, they are connected to form contours (as represented in the connectivity map) by detecting edge intersections and tracking the contour as it moves across the polygons. The contour is tracked until it forms a closed loop or exits the dataset boundary. If there are no holes, a perfect connectivity map consisting of a single loop is obtained.

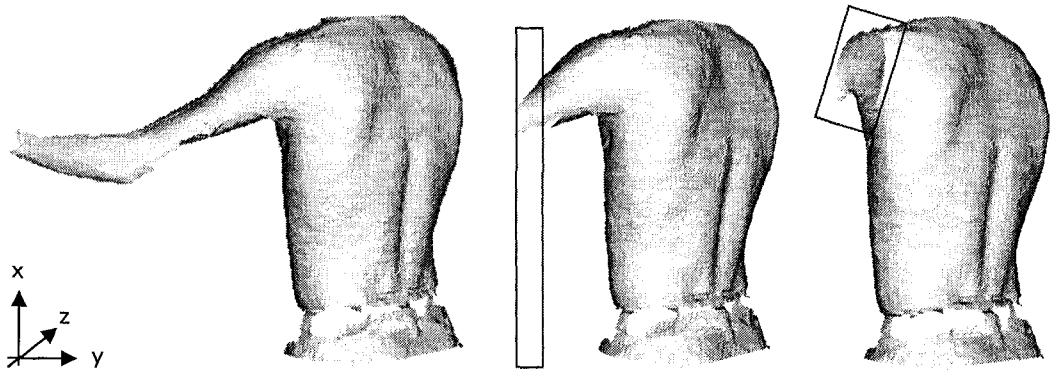

Fig. 8.3: Progressing clipping of a torso scan using plane and box clipping tools. The cutting boxes are shown in red.

8.3.2 Hole detection

Definition: A hole exists if $\|p_i \circ p_{i+1}\| \geq MD + 2 \cdot \sigma$, $\forall \ p_i, p_{i+1} \in P$, $i \in \{1,\ldots,N\}$.

In other words, a hole is a disconnection between points in the connectivity map of a cross-section. Holes are identified during the generation of the connectivity map in the cross-sectioning stage. Boundary points are points that are adjacent to holes and connected to exactly one other point. Stray points are connected to no other point and exist in the vertex array but not in the connectivity map. These are removed from the vertex array and appropriate modifications made to maintain consistency. Missing points exist in the connectivity map but not in the vertex array. Two arrays P_{ord} and P_{hole} are created. P_{ord} stores points in their sequential order akin to the vertex array and P_{hole} stores all the boundary points of the holes in their order of occurrence. The centroid of the cross-section $c = (c_x, c_y, c_z)$, $c \in R^3$, is obtained from the rectangular coordinates of the points in the vertex array as

$$c_x = \left(\frac{\sum_{i=1}^{N} p_{ix}}{N} \right), c_y = \left(\frac{\sum_{i=1}^{N} p_{iy}}{N} \right), c_z = p_{iz}.$$

In a symmetric cross-section of the torso, the farthest points lie on opposite sides of the centre point spanning the *maximal diameter* of the cross-section[7]. In Algorithm I, $\max Dist$, the Euclidean distance between $\max p_1$ and $\max p_2$, is the *maximal diameter* of the cross-section. The *maximal radius*, half of the *maximal diameter*, is used to construct a point $p_s = (p_{sx}, p_{sy}, p_{sz})$, $p_s \in R^3$, which serves as the initial point in the P_{ord} array, where

$$\begin{aligned} p_{sx} &= (\max imalRadius \times \cos(st)) + c_x, \\ p_{sz} &= (\max imalRadius \times \sin(st)) + c_z, \\ p_{sy} &= c_y. \end{aligned} \tag{3}$$

The value of $st \in R$ used in (3) was 0.5 radians.

8.3.3 Convexity algorithm

Another problem associated with clipping torso images of humans is how to handle the shoulder regions and the regions of the upper arms above the armpit. Based on the application, a decision was made to retain both regions and crop other parts of the arm. This created the problem of locating the positions of the armpits as the imaging posture required placing the arms close to the body. To solve this problem, the regions of the arms below and above the armpits were defined by their convexity.

In their work on digital point-based curves, curvature functions and graphs, Pikaz and Dinstein [13] define a concave chain as a sequence of points in which each point and its two immediate neighbours generate a negative angle. This definition can be directly applied to torso cross-sections represented as point-based curves as in the

[7] This assumption does not hold for arbitrary shapes such as severely deformed torso cross-sections. In general, the *maximal diameter* can be defined as twice the farthest distance of any point from the centre of the cross-section.

forgoing. A concave chain belonging to P will be a convex chain of P after changing the plane of orientation. Based on this definition, regions of the arm above or below the armpit can be differentiated by their convexity as shown in Fig. 8.4 by using a user-defined threshold. Thus, the task reduces to detecting and eliminating regions whose convexities are above the user-defined threshold. Its operation is based on the ordered set of points P_{ord} and depend on the depth p_{iz}, of individual points with respect to their neighbours around user-defined regions of interest defined by their p_{ix} coordinate.

Upon inspecting the 3D image the user selects two points p_{az} and p_{bz} based on their p_{ix} values representing the two regions of interest. The most convex points are assumed to lie within $p_{ix} \pm 20$ units of the selected points. The value of 20 was chosen from experiments. The algorithm was applied to points in the cross-section whose depth with respect to the depth of the centre $p_{iz} - c_z$ were below the user-defined range $\max(p_{az} + 20, p_{bz} + 20)$. This is shown in Fig. 8.5. Quadrants of an inscribing circle of *maximal radius* centred at c were obtained.

The points within each quadrant were arranged in order of the magnitude of their depth from the plane of c. Points whose depths were below the threshold were said to be within the region of interest (Fig. 8.5). Points within the regions of interest accounted for an average of 30% of points in P_{ord}. The most convex point within each quadrant was determined and the section of interest (Fig. 8.6) selected. The sections of interest in the four arrays were merged to form the updated P_{ord}.

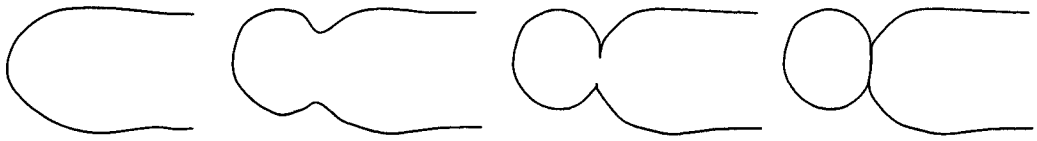

Fig. 8.4: Varying degrees of convexity: Concave and partly concave half-sections (leftmost two); partly convex and completely convex half-sections (rightmost two).

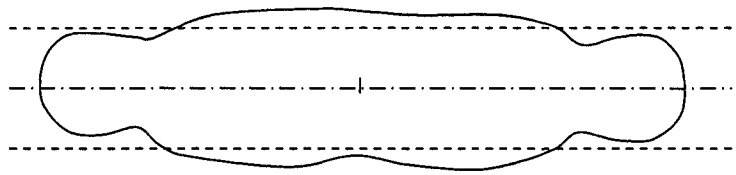

Fig. 8.5: *Regions of Interest*: The regions of interest correspond to the parts of the cross-section between the two dotted lines and centered on the center line.

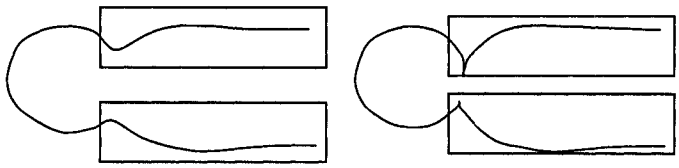

Fig. 8.6: *Sections of Interest*: The sections of interest are contained in the rectangular boxes for the partly concave and partly convex half-sections.

8.3.4 Torso Hole Filling

Torso hole filling was implemented using the SMLS approximation procedure. The first part of the procedure was spline interpolation to estimate the shape of the missing part. The second part was interpolation using MLS. From Section 8.2, the second part can be implemented in either of two ways. Depending on which method was used, the interpolated data points were stored in either the P_{MLS} or P_{SEL} array. Each new data point was added to the P_{ord} array between the boundary points of the corresponding hole resulting in a connected set of points in the P_{ord} array with an

average separation of MD. The SMLS procedure was implemented on one cross-section at a time. For each cross-section apart from the first, the initial estimate obtained from spline interpolation is combined with the data from the previous cross-section to produce the estimate used in the second part of the SMLS procedure. This yields a better result as the 3D form of the image is exploited.

8.3.5 Re-sampling and surface generation

The P_{ord} arrays contain points from cross-sections of varying sizes. Mid-range cross-sections are generally the largest of all. Point distributions obtained from the P_{ord} arrays are generally non-uniform in size and inadequate for dynamic rendering. They need to be uniformly resampled to a user defined density per cross-section. This is achieved by spline interpolation using splines. The resampled rectangular array of points is stored in the P_{comp} array. Redundancy in P_{comp} is reduced. This ensures that the points are centered on the centroid and uniformly spaced around the enclosing circle of the cross-section. For a user-defined number of points per cross-section NP, the angular spacing between points is

$$st = \left(\frac{2\pi}{NP}\right). \tag{4}$$

8.4 RESULTS

This section presents the results of testing the SMLS reconstruction procedure on torso images of 30 volunteers, 22 of whom have scoliosis. The scans were obtained using the methods of Ajemba *et al.* [14], [15]. The procedure was implemented in the Microsoft Visual C++ .Net 2003 environment on a Pentium IV PC running at 1.8GHz. Fig. 8.7 shows a stepwise implementation of the procedure on a torso scan

of a volunteer who has scoliosis. Tests were performed to evaluate and compare the reconstruction accuracy achieved using the SMLS, MLS the BC theories.

8.4.1 Hole filling using the SMLS, BC and MLS techniques

Twenty cross-sections containing holes with different bounding polygons were obtained from ten range images of the human torso and filled using the MLS-based procedure, the BC-based procedure and the SMLS-based procedure. Fig. 8.8 shows the results obtained for four of the holes. In general, the MLS projection theory failed as it produced straight interpolation lines since the holes were too large. The BC approximation theory produced symmetrical C^{∞} smooth interpolation arcs while the SMLS projection procedure produced smooth interpolation arcs that were somewhat skewed. The degree of skew of the arcs was determined by the MLS parameters used. Cross-sections of the human torso do not exhibit perfect local symmetry, thus the SMLS interpolation tended to yield a closer fit to the original curve.

8.4.2 Validation of cross-sections reconstructed using the SMLS and BC techniques

Ten complete cross-sections (containing no holes) were obtained from each of the 30 torso images. The cross-sections were modified by randomly creating holes on them that account for up to 10% of their perimeters. Each modified cross-section was then reconstructed using the SMLS and BC based procedures and evaluated using four validation indices (Table 8.1). The original sections with no holes were used as the gold standard for the comparisons. The reconstructed cross-sections were optimally aligned to the original cross-sections using their centroids and maximal diameters. A minimum bounding circle containing the actual and reconstructed cross-sections was defined as the universal set for the purpose of computing indices C and D (Table

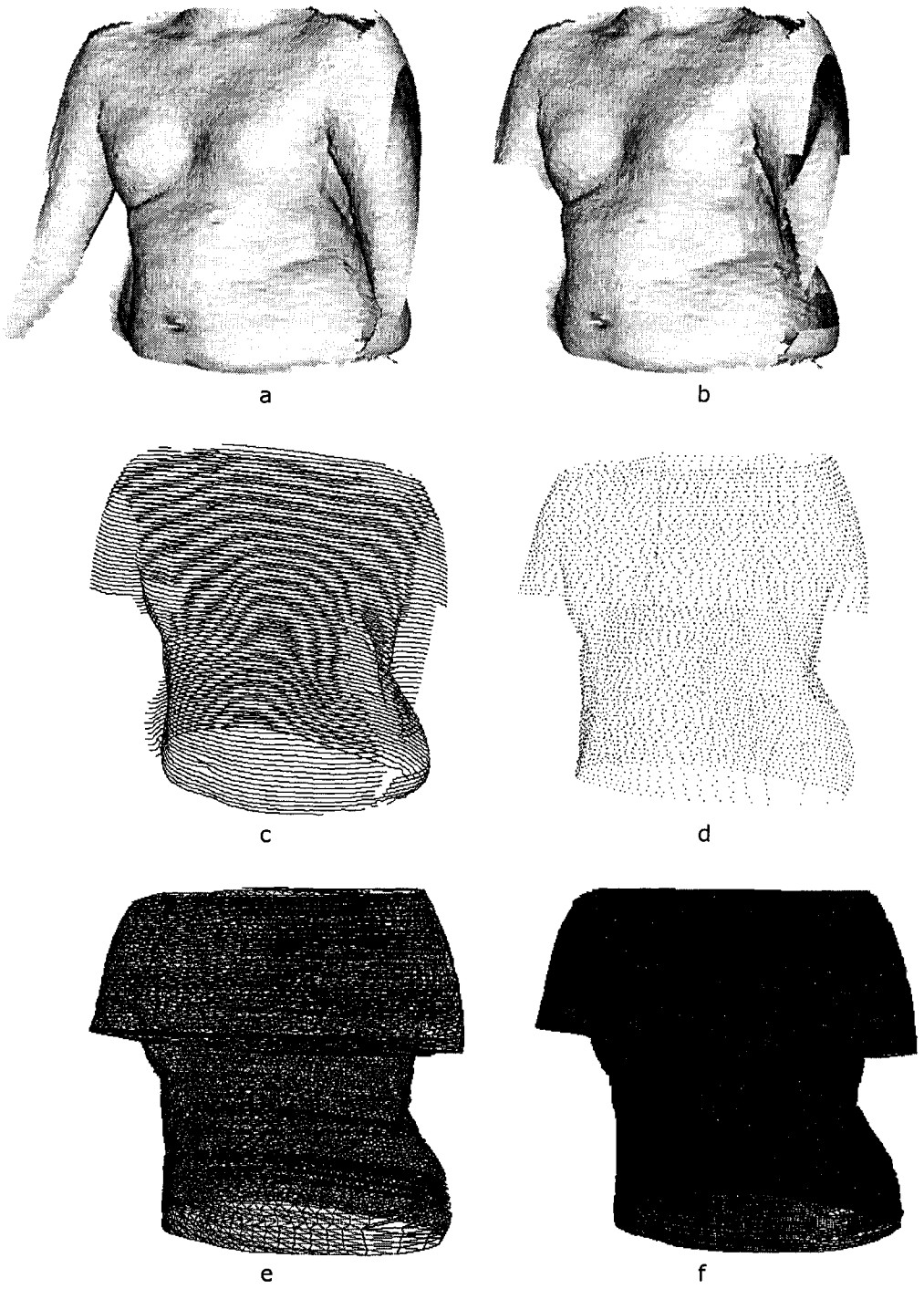

Fig. 8.7: Stepwise implementation of the SMLS procedure. Results of (a): Plane-clipping; (b) Box-clipping; (c) Cross-sectioning (72 cross-sections); (d) Hole and convexity-detection and hole-filling; (e) Resampling and meshing; and (f) Surface generation.

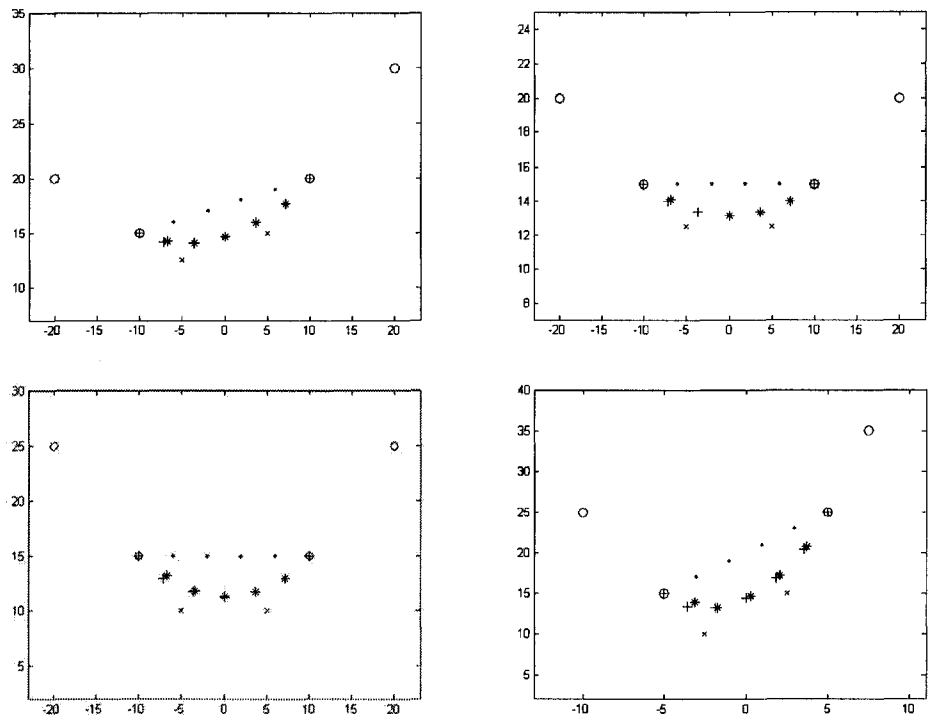

Fig. 8.8: Results of interpolating four holes with MLS (•.), BC (*) and SMLS (+)

8.1). An average value for each index was obtained over the 300 cross-sections. Table 8.2 shows the results obtained. The SMLS procedure outperformed the BC in all the measured indices.

8.4.3 Validation of volumes reconstructed using the SMLS and BC techniques

Table 8.2 also shows validation results obtained from five torso images. The images were randomly selected from the 30 originally obtained and reconstructed using the SMLS procedure. Holes accounting for up to 10% of the surface area were randomly created on the torso images. The modified torso images were then reconstructed using the SMLS projection procedure and the BC approximation procedure. The reconstructed cross-sections were optimally aligned to the original cross-sections using their centroids and maximal diameters. The universal set for computing indices C and D was the minimum bounding cylinder enclosing both the original and

Table 8.1: Validation indices used

	Formula*	Psuedo-name	Description
A	$\frac{C_a \cap C_p}{C_a}$	Positive Predictive Value	This is a ratio of the size of the overlap between the original and reconstructed cross-section (or volume) to the size of the original cross-section (or volume).
B	$\frac{C_a \cap C_p}{C_p}$	Sensitivity	This is a ratio of the size of the overlap between the original and reconstructed cross-section (or volume) to the size of the reconstructed cross-section (or volume).
C	$\frac{\Im - C_a \cup C_p}{\Im - C_a}$	Negative Predictive Value	This is a ratio of the size of the difference between the union of the two cross-sections from the universal set to the difference between the original cross-section (or volume) from the universal set.
D	$\frac{\Im - C_a \cup C_p}{\Im - C_p}$	Specificity	This is a ratio of the size of the difference between the union of the two cross-sections from the universal set to the difference between the reconstructed cross-section (or volume) from the universal set.

*C_a is the original cross-section (or volume); C_a is the reconstructed cross-section (or volume); and $\Im$ is the universal set consisting of the minimum bounding circle (or cylinder) containing the original cross-section (or volume) and the reconstructed cross-section (or volume).

Table 8.2: Average validation indices obtained for 300 cross-sections and 5 volumes reconstructed using the SMLS projection procedure and the BC approximation procedure

Indices	Cross-Sections				Volumes			
	A	B	C	D	A	B	C	D
SMLS	0.88	0.87	0.86	0.88	0.80	0.77	0.76	0.79
BC	0.83	0.81	0.79	0.81	0.82	0.75	0.72	0.80

reconstructed images. An average value of each index was obtained over the 5 images. The SMLS procedure outperformed the BC procedure in two of the four measured indices.

8.4.4 Error tolerance

The tolerance of the SMLS, BC and MLS procedures to errors (holes) were tested by reconstructing models of a randomly selected complete surface (reconstructed using the SMLS technique) with 0.05-0.20 hole-area-per-total-surface-area-ratio. A procedure is said to fail if all the validation indices obtained are less than 0.70[8]. The MLS, BC and SMLS procedures failed for hole-area-per-total-surface-area-ratios of 0.10, 0.20 and 0.20 respectively. Though both the BC and SMLS procedures failed at the same hole-area-per-total-surface-area-ratios, the BC procedure failed in a more drastic manner (Fig. 8.9).

8.5 CONCLUSION

Spline based interpolation techniques like BC assume uniform smoothness on both sides of a hole and return symmetric curves when interpolating holes that occur at the edge of the torso. Though the output can be visually pleasing, it is generally unrealistic as actual human torsos are usually locally unsymmetrical. Also, the global nature of BC interpolation makes outlier points significantly influence the generated curves. The MLS approximation technique applies more weight to the control points close to the hole than those far away from it. Thus in theory, MLS should perform better than BC for interpolating unsymmetrical shapes. However, for hole-area-per-total-surface-area-ratio (or hole-length-per-total-cross-section-length-ratio) greater than 0.10, the MLS technique fails. This failure can be prevented by leveraging the strengths of both MLS and spline fitting. This was achieved in the framework of the SMLS projection procedure.

This chapter presented a comprehensive procedure for pre-processing and reconstructing range images comprising an interactive technique for cropping stray

[8] We chose this value from our experiments.

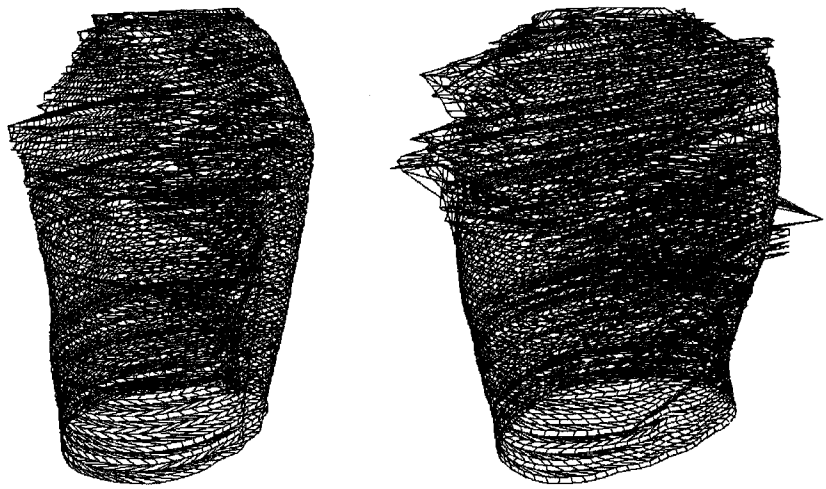

a b

Fig. 8.9: Results of re-sampling and meshing a badly deformed torso scan of a normal volunteer using the SMLS projection (a) and the BC approximation procedures (b) at 0.2 hole-area-per-total-surface-area.

points and extremities and a novel interpolation technique (SMLS) for filling holes. Three stages were involved: cross-sectioning and clipping; hole-filling and sub-sampling; and surface re-generation. Results of tests on images of 30 volunteers, with and without scoliosis, showed that the technique outperformed spline based techniques in the presence of large holes (as is usually the case in torso images used for evaluating scoliosis). The results were based on four new validation metrics (corresponding to sensitivity, specificity, negative predictive value and positive predictive value). The procedure can be applied to pre-processing range images used in other areas of medicine, science and engineering.

REFERENCES

1. A. Sarti, R. Malladi, J. A. Sethian, 'Subjective surfaces: A method for completing missing boundaries,' *Proceedings of the National Academy of Science*, vol. 97, no. 12, June 2000.
2. R. E. Crochiere, L. R. Rabiner, 'Interpolation and decimation of digital signals-A tutorial review, *Proceedings of the IEEE*, 69(3) pp 300 - 331, March 1981.
3. N. Newmann and S. Sproull, *Principles of Interactive Computer Graphics*, McGraw-Hill, USA, 1973.

4. E. Cohen, R. F. Riesenfeld, G. Elber, *Geometric Modeling with Splines: An Introduction*, A K Peters, Natick, Massachusetts, 2001.
5. D. Blanco, D. R. Ruiz, E. Alameda-Hernandez E, *et al.*, 'Extinction pulses synthesis for radar target discrimination using beta-splines,' *IEEE Transactions on Antennas and Propagation,* 54 (5) 1577-85 May 2006.
6. T. N. Sederberg, J. M. Zheng, A. Bakenov, *et al.*, 'T-splines and T-NURCCs,' *ACM Transactions on Graphics,* 22 (3): 477-484 Jul 2003.
7. V. N. Vapnik, *Statistical Learning Theory*, New York, NY: Wiley, 1998.
8. B. Allen, B. Curless, Z. Popovic, 'Articulated Body Deformation from Range Scan Data,' *ACM Transactions on Graphics*, v 21, n 3, pp. 612-9, July 2002
9. C. Liao, and G. Medioni, 'Surface Approximation of a Cloud of 3D Points,' *Graphical Models and Image Processing*, vol. 57, No. 1, pp 67-74, 1995.
10. B. Allen, B. Curless, Z. Popovic, 'The space of human body shapes: reconstruction and parameterization from range scans,' *ACM Transactions on Graphics*, vol. 22, no. 3, pp. 587-94, July 2003.
11. M. Alexa, J. Behr, D. Cohen-Or, S. Fleishman, D. Levin, C. T. Silva, 'Computing and Rendering Point Set Surfaces,' *IEEE Transactions on Visualization and Computer Graphics*, 9(1), pp 3-15, January-March, 2003.
12. I. E. Sutherland, G. W. Hodgman, 'Reentrant Polygon Clipping,' *Communication of the ACM*, 17(1), pp 32-42, January, 1974.
13. A. Pikaz, and I. Dinstein, 'Using Simple Decomposition for Smoothing and Feature Point Detection of Noisy Digital Curves,' *IEEE Transactions on Pattern Analysis and Machine Intelligence*, vol. 16, no. 8, pp 808-813, August, 1994.
14. P. O. Ajemba, N. G. Durdle, D. L. Hill, and V. J. Raso, 'A torso imaging system for quantifying the deformity associated with scoliosis,' *IEEE Transactions on Instrumentation and Measurements,* vol. 56, no. 5, October 2007.
15. P. O. Ajemba, N. G. Durdle, D. L. Hill, and V. J. Raso, 'A Torso Imaging System for Quantifying the Deformity Associated with Scoliosis,' *In Proceedings of the IEEE Instrumentation and Measurement Technology Conference*, Ottawa, 17–19 May, 2005.

CHAPTER 9

EVALUATION OF THE TORSO IMAGING AND ANALYSIS SYSTEM[N]

9.1 INTRODUCTION

In this chapter, we consider the task of evaluating the entire system for imaging and assessing human torsos for deformities such as scoliosis. (A discourse on scoliosis and torso imaging is presented in Chapter 2.) The system comprises of image acquisition, image reconstruction and shape analysis components. The evaluation procedure consists of three steps: 1) assessment of the accuracy of reconstruction of the system using inanimate models; 2) evaluation of the system response to anticipated errors in the input values due to patient positioning, sway and breathing; and 3) analysis of the variability of clinically relevant indices using multiple scans of a number of volunteers with and without scoliosis. The clinically relevant indices can be grouped into landmark-based and shape-based categories. This chapter also attempts to justify investing in full torso imaging systems, as against the more prevalent back torso imaging systems. This is done by analyzing the relative contributions of the front and back torso relative to the full torso.

9.2 THE IMAGING AND ANALYSIS SYSTEM

The system for imaging and assessing torso deformity consists of three components: 1) a torso imaging system comprising of two Minolta VIVID 700 digitizers and a rotating positioning platform (Chapter 7); 2) image reconstruction routines for filling

---

[N] A version of this chapter has been accepted for publication. P. O. Ajemba, N. G. Durdle, and V. J. Raso, 'Validation of an imaging and analysis system for assessing torso deformities,' *Computers in Biology and Medicine*, 2005. Additional material contained in this chapter has been submitted for publication: P. O. Ajemba, N. G. Durdle, and V. J. Raso, 'Suitability and robustness of structured splines models for the assessment of torso deformity due to scoliosis,' *Medical and Biological Engineering and Computing*, 2007.

holes, removing eliminating stray data points, and cropping away unwanted parts of the torso image (Chapter 8); and 3) shape analysis routines for obtaining the structured splines model and associated indices of torso deformity (Chapter 3).

9.3 INDICES OF TORSO DEFORMITY

Indices of torso deformity can be grouped into landmark-based and shape-based categories. In this section, we describe the two categories and review methods of classifying torso deformity in scoliosis based on both categories.

9.3.1 Landmark-based indices

There are a number of anthropometric landmarks on the human torso. Fig. 9.1 shows seventeen of them. The location of a torso landmark is often given in terms of the vertebrae levels where T is for thoracic, L is for lumber, and S is for sacral. For example, the bottom of the sternum is located close to T5 or the fifth thoracic vertebrae. A class of landmark-based indices of torso deformity were developed as part of many legacy torso imaging systems. These include the Cosmetic Score [1], the Posterior Trunk Symmetry Index (POTSI) score [2], the Integrated Shape Imaging System (ISIS) score [3], and the Quantec score [4]. Table 9.1 shows a representative set of landmark-based indices of torso deformity [5], [6].

9.3.2 Shape-based indices

Our previous work (Chapter 3) introduced the structured splines model, a novel shape descriptor for 3-D objects based on curvature. The structured splines model was applied to solve the problem of quantifying torso deformity and tracking changes in torso shape in scoliosis (Chapter 4). Three indices of torso deformity were obtained from the analysis of key points of structured splines models: twist, bend and tilt corresponding to rotations in the side, back-front and top views respectively.

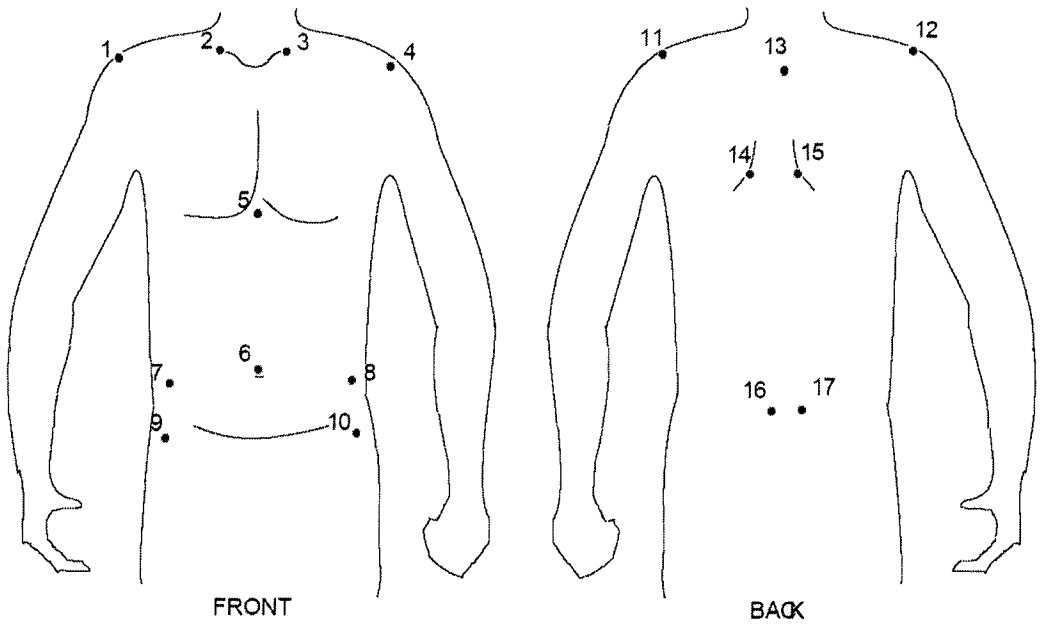

Fig. 9.1: Prominent anthropometric landmarks on the torso. 1–Right Acronium (Front); 2–Right Clavicle; 3–Left Clavicle; 4–Left Acronium (Back); 5–Bottom of Sternum; 6–Umbilicus; 7–Top of Right Iliac Crest; 8–Top of Left Iliac Crest; 9–Right Anterior Superior Iliac Spines of the Pelvis; 10–Left Anterior Superior Iliac Spine of the Pelvis; 11–Left Acronium (Back); 12–Right Acronium (Back); 13–Seventh Cervical Vertebra; 14–Tip of Left Shoulder Blade; 15–Tip of Right Shoulder Blade; 16–Left Posterior Iliac Spine; 17–Right Posterior Iliac Spine.

9.3.3 Classification of torso shape

The deformation indices yield at least two approaches to classifying torso shape: grouping by aggregation of distributions and grouping by locations in shape space. Single valued indices (which include most landmark-based indices) are often grouped by distribution. Here, appropriate boundaries are sought in their histograms or grouping is achieved using techniques such as the *k*-means classification method. The most common grouping strategy for torso shape is mild, moderate and severe deformity. Multi-valued indices are more amenable to grouping by location in shape space. For our shape-based indices, an eight-class system is obtained from the signs of the deformation indices (Table 4.2). Fig. 4.7 shows examples of each class.

Table 9.1: Representative indices of torso deformity

Index category	Torso asymmetry index	Unit	Torso level
Centroid line	Range of lateral deviation	mm	T7 - L4
Principal axes	Range of PAX orientation	(^{0})	T12 - L5
	Maximal Rotation of PAX	(^{0})	T11 - L4
	Minimum cross-section eccentricity	...	T8 - L5
Back surface rotation	Range of rotation	(^{0})	T3 - L3
	Maximal value of rotation	(^{0})	T5 - T12
	Range of rib hump; left-right, measured from PAX	mm	T10 -S1
	Difference between PAX orientation and BSR	(^{0})	T11 - L5
Envelope	Range of left-right difference in aspect ratio (lat/AP)	...	T7 - L2
	Diff between left & right half-widths from centroid	...	L2 - L5
0th moment	Diff between left and right half areas	...	T7 - S1
1st moment	Diff between left and right half-centroid, AP locations	mm	T11 - S1
2nd moment	Quasi-Cobb angle of curve of left-right diff in lateral inertia	(^{0})	T11 - S1
Quarter areas	Range of orientation of line joining rear quarter-centroids	(^{0})	T8 - L5
	Range of left-right difference in rear quarter areas	...	T12 - L5
Ratios	Ratio of waist diameter to hip diameter; relative placements of wait and hip centers (Cosmetic Score)	...	T5 - L5
SPL	Range of lateral deviation	mm	T12 - L4

... = dimensionless, AP: anterior-posterior, lat: lateral, PAX: principal axes, BSR: back surface rotation, SPL: spinous process line, diff: difference.

9.4 MATERIALS AND METHODS

The scoliosis volunteers for this study were recruited from the scoliosis clinic at the Glenrose Rehabilitation Hospital, Edmonton, Alberta, Canada. The following inclusion criteria were used: 1) a diagnosis of idiopathic scoliosis; 2) age at first clinical visit of at least 8 years; and 3) availability of one or more back torso or full torso images showing visible torso deformity. Patients admitted to the scoliosis clinic were generally deemed to have progressive scoliosis. The images were acquired as

described in [7], [8]. The data collection procedures and experimental protocols were approved by the University medical research ethics panel.

Four analyses were performed: 1) an assessment of the reconstruction accuracy of the system using repeat acquisitions of images of static models (a calibration box and a mannequin); 2) an analysis of the response of the system to expected variations in shape due to sway and breathing using repeat acquisitions of the images of three non-scoliosis volunteers; 3) an analysis of the variability in clinically relevant indices of torso deformity using repeat acquisitions of the images of ten scoliosis volunteers; and 4) an analysis of the relative contributions of the back torso and front torso images using full torso images obtained from 43 scoliosis volunteers.

9.4.1 Reconstruction accuracy

The accuracy of reconstruction of the imaging system was assessed from repeat acquisitions of the range images of a calibration box (of dimensions 300 mm by 150 mm by 200 mm; machined to an accuracy of 1 mm and measured to a precision of 0.1 mm) and a mannequin (made from a cast of an actual scoliosis torso and measured to a precision of 0.1 mm). The edges of the box served as markers detectable on both the geometry and texture data of the 3-D reconstructions. The digitizers were placed opposite each other as in Arrangement 2 of Fig. 9.2. The effect of lighting on surface reconstructions was qualitatively assessed. The *acquisition-room* was darkened but differences in surface reconstructions due to subtle variations in the lighting conditions were still observed.

To assess the accuracy of reproduction of the dimensions of the test-box, two sets of five full surface scans of the box were acquired with the box repositioned after each scan. One set of scans was taken with the sides of the box perpendicular to the line of sight of the digitizer. The other set of scans was taken with the sides 45^0 to the line of sight of the digitizer. The dimensions of the reconstructed image of the

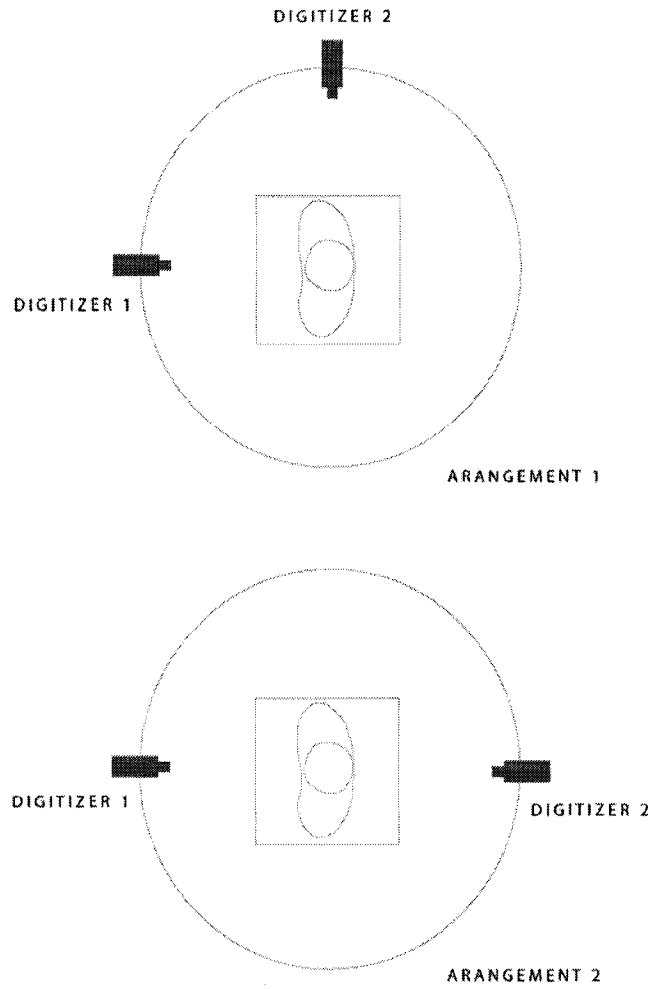

Fig. 9.2: The two arrangements for the two digitizer configuration

test-box were measured from each scan and the root mean square errors and standard deviations were calculated. The 12 edges (four each of length, width and height) were measured from the reconstructed images (2 positions × 5 repetitions × 12 edges). A multi-way analysis of variance was conducted on the measured dimensions to evaluate the accuracy of the reconstructions and to highlight some factors with significant effect. Acquisition sequence, positioning (or placement) of the test-box relative to the digitizer, and digitizer (A or B) used were factors. The effects of re-positioning and the use of one or two digitizers on the accuracy of reconstruction were assessed. A set of ten scans of a mannequin (Fig. 2.7) was obtained using the two digitizers placed at right angles to each other as in

Arrangement 1 of Fig. 9.2. Two sets of scans were also obtained using each of the digitizers (A and B) separately.

9.4.2 System response to sway and breathing

The response of the system to expected variations due to sway and breathing was assessed from repeated acquisitions of images of three non-scoliosis volunteers. The volunteers were male and had no history of scoliosis or any other spinal deformity. They were 18.5, 19.6 and 21.2 years old.

Ten torso images were obtained for each volunteer at thirty-minute intervals during a five-hour long imaging session. The volunteers were standing and grabbing the side handles of a rotating positioning platform (Fig. 2.1). The two digitizers were placed as in Arrangement 2 of Fig. 9.2. The positioning platform was placed such that the back (or front, depending on the digitizer, see Fig. 9.2) of the images of the volunteers were at 90^0 to the line of sight of the digitizers at the start of the image acquisition cycle. The volunteers were asked to inhale deeply and hold their breadths as each shot was taken. Though the acquisition room was darkened during the image acquisition cycles, subtle differences in lighting were still observed.

The holes in each acquired image were interpolated and stray points removed. The extremities (arms, head and neck, and regions below the waist) of each image were cropped. Each torso image was sectioned into ten evenly spaced cross-sections. A centroid line joining the centroids of each section was generated for the purpose of analyzing the effect of sway on the reconstruction system. The distance D, between the centroid and a fixed vertical line was calculated at each cross-section (Fig. 9.3). The fixed vertical line is the origin of the bottom cross-section. For the variability due to sway, the standard deviations in D at each cross-section were calculated for each volunteer from the ten scans obtained per volunteer. The width W and length L of the ten cross-sections obtained per volunteer was calculated at each level. Variability

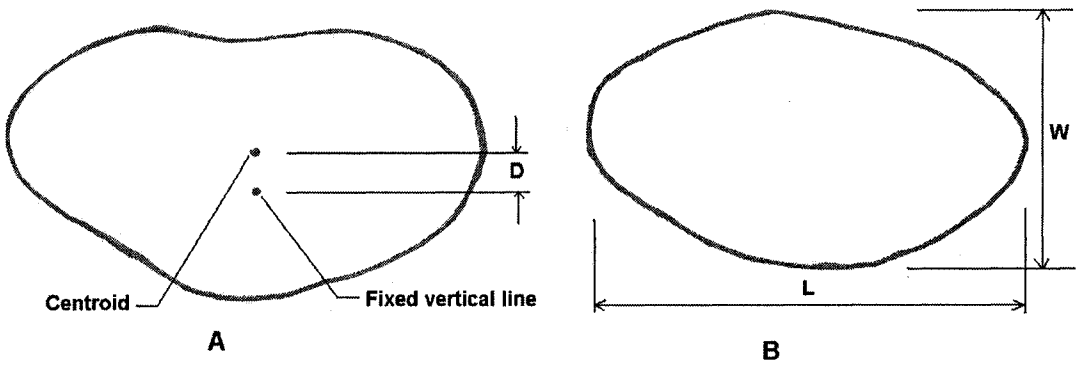

Fig. 9.3: **A**, the variability due to sway. D is the offset of the centroid from the fixed vertical line. **B**, the variability due to breathing. H and L are the torso height and width.

due to breathing was assessed by calculating the standard deviations in W and L at each cross-section from the ten scans obtained for each volunteer.

For each of the ten images of the three volunteers, a $180\times180\times3$ structured spline model was obtained. The shape-based deformity indices: twist, bend and tilt, were calculated in ten horizontal segments for each image. The system response to the calculated variability due to sway and breathing was assessed from the standard deviations in the shape-based indices over the ten images of each volunteer.

9.4.3 Variability of clinically relevant indices

The variability of clinically relevant indices of deformity (both landmark-based and shape-based) was assessed from three repeated acquisitions of the images of ten scoliosis volunteers. Table 9.2 shows the clinical indices of the volunteers. The images were acquired and pre-processed in a way similar to those of the non-scoliosis volunteers. $180\times180\times3$ structured spline models were obtained for each of the three images of the ten volunteers. Shape-based deformation indices: twist, bend and tilt, were obtained from the structured splines model. Landmark-based deformation indices; cosmetic score, were also obtained for each torso image. The variability of the clinically relevant indices was assessed from the standard deviations

Table 9.2: Clinical description of the volunteers used to validate the system

Volunteer	Sex	Age	Cobb Angle	Height	Weight	DC	TT	MCS
One	F	16.1	40	163	54	25	18	3.7
Two	F	15.1	50	157	53	33	11	1.4
Three	M	16.9	50	167	62	17	19	2.7
Four	F	15.4	45	169	60	17	19	2.5
Five	M	14.3	25	165	61	10	12	3.5
Six	F	13.8	54	165	56	5	14	2.5
Seven	F	17.6	27	156	58	4	7	1.3
Eight	F	14.8	46	167	61	0	22	3.3
Nine	F	14.4	45	165	57	18	12	2.1
Ten	F	12.5	25	156	50	35	1	1.0

Cobb angle, decompensation (DC) and trunk twist are given in degrees. Height is in cm. Weight is in kilograms. Mean Cosmetic Score (MCS) is the mean of the scores obtained from the images we use in our analysis and ranges from 0 to 10 in increasing order of deformity. TT is trunk twist.

in each index value for each volunteer. Variability is shape-based classification was also assessed from the frequency of class change.

9.4.4 Relative information contents of front and back torso images

The analysis of the relative information contents of the back torso and front torso images was based on information from the full torso images of 43 scoliosis volunteers. The torso images were acquired and pre-processed in the same way as those of non-scoliosis volunteers. Fig. 9.4 shows the distribution of the shape-based deformation indices obtained from the back torso, front torso and full torso images. The relative information contents of the back torso and full torso was assessed from the variability of the distributions as information content is related to entropy.

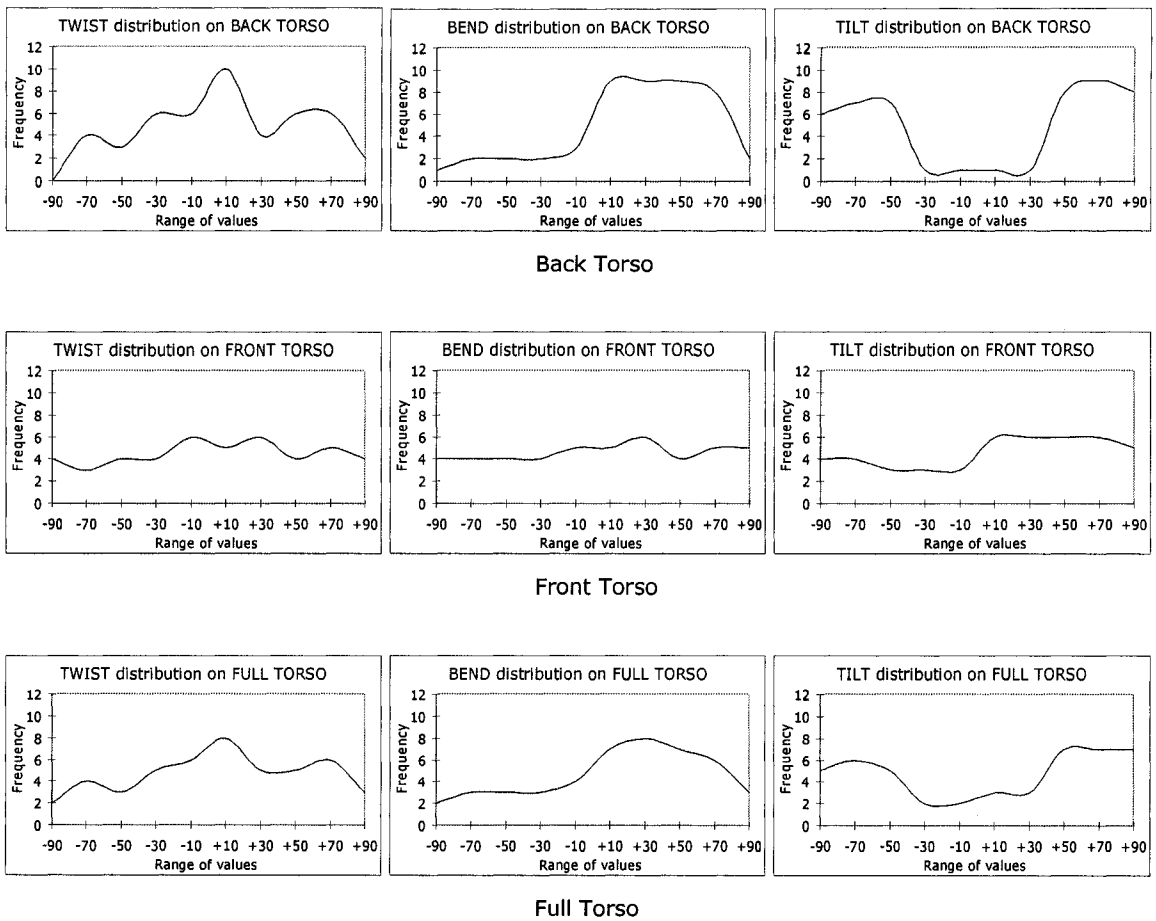

Fig. 9.4: Distribution of shape based deformation indices in the dataset of 43 patients

9.5 RESULTS

9.5.1 Reconstruction accuracy

Table 9.3 shows the errors in calculating the length, width and height (dimensions) of the sides of the test-box. Overall, the error was estimated to be 1.16 ± 1.04 mm, which is of the order of magnitude as the digitizer's resolution. The absolute errors in the dimensions of the test box followed a half normal distribution with a standard deviation of 1.04 mm. Measurements of the length of the box showed the highest variation 1.32 ± 1.13 mm. Table 9.4 gives the analysis of variance in the dimensions of the test-box for acquisitions. It shows a significant difference in the sum of

Table 9.3: Errors related to the dimensions of the test-box

Dimensions	Errors	RMS Errors	Range	N
Lengths	0.99 ± 0.98 mm	1.93 mm	0 - 4.1 mm	40
Widths	1.17 ± 1.06 mm	2.46 mm	0 - 4.6 mm	40
Heights	1.32 ± 1.13 mm	2.98 mm	0 - 4.6 mm	40
Average of Dimensions	1.16 ± 1.04 mm	2.45 mm		

Table 9.4: Analysis of variance in the dimensions of the test-box (in mm)

	Sum of Squares	Degree of Freedom	Mean Squares	Fischer coefficient	Prob > *F*
Acquisitions	103.04	9	11.45	5.94	0*
Dimensions	467720.09	11	42520.01	22060.04	0*
Error	190.82	99	1.93		
Total	468013.96	119			

*Statistically significant correlation ($p<0.05$)

squares between acquisitions and dimensions. Analysis of variance performed using sets of scans instead of acquisitions shows that there is a significant difference within series and between series and that the variations within the set obtained with the faces 45^0 to the line of sight of the digitizer was 20% higher than within the set obtained with the sides of the box perpendicular to the line of sight of the digitizer.

Table 9.5 shows the standard deviations in the lengths of ten evenly spaced cross-sections of a mannequin obtained using each of two digitizers (A and B) alone and both digitizers in tandem. The numbering of the cross-sections increased from the waist of the mannequin upwards. The deviations in the lengths of the cross-sections close to the waist were lower than those of cross-sections farther from the waist due to persistent errors in aligning the central axis of the mannequin to the line of sight of the digitizer. These errors were caused by the not-perfectly symmetrical motion of the test platform and are a function of the setup of the experiment. The deviations in the lengths of cross-sections obtained from *single-digitizer images* were about 20% higher than those obtained from *double-digitizer images*. Table 9.6 shows the results

Table 9.5: Standard deviations in the lengths of cross sections of the mannequin

Digitizers	Standard Deviation (mm)									
	1	2	3	4	5	6	7	8	9	10
A	0.64	0.83	0.92	1.04	1.12	1.06	1.06	1.12	1.16	1.71
B	0.58	0.75	0.83	1.14	1.03	1.04	1.10	1.01	1.06	1.82
A and B	0.47	0.67	0.75	0.98	0.95	0.94	0.93	0.94	0.99	1.04

Table 9.6: Standard deviations in the lengths of cross sections of a human volunteer

Digitizers	Standard Deviation (mm)									
	1	2	3	4	5	6	7	8	9	10
A	0.82	1.09	1.20	1.33	1.44	1.40	1.38	1.43	1.51	2.24
B	0.84	1.15	1.23	1.29	1.51	1.42	1.41	1.41	1.49	2.26
A and B	0.80	1.01	1.02	1.13	1.14	1.14	1.23	1.34	1.44	2.14

of a similar analysis for one of the non-scoliosis volunteers. The deviations in the lengths of cross-sections obtained from the volunteer were about 30% higher than those obtained from the mannequin because of the added sway.

These results and other qualitative information obtained showed that a significant fraction of the errors observed was due to the registration and merging of the partial scans. Variations in light intensity and surface reflectance contributed to the observed errors as well as the imperfect alignment of the positioning platform.

9.5.2 System response to sway and breathing

Fig. 9.5 shows the variability in the dimensions of the ten cross-sections due to sway and breathing for each of the three non-scoliosis volunteers. The figure in addition shows the variability in the shape-based deformity index values (Euclidean norm of twist, bend and tilt) at each of the ten evenly spaced horizontal sectors for each volunteer. Each sector corresponds to a cross-section in Fig. 9.5. The standard

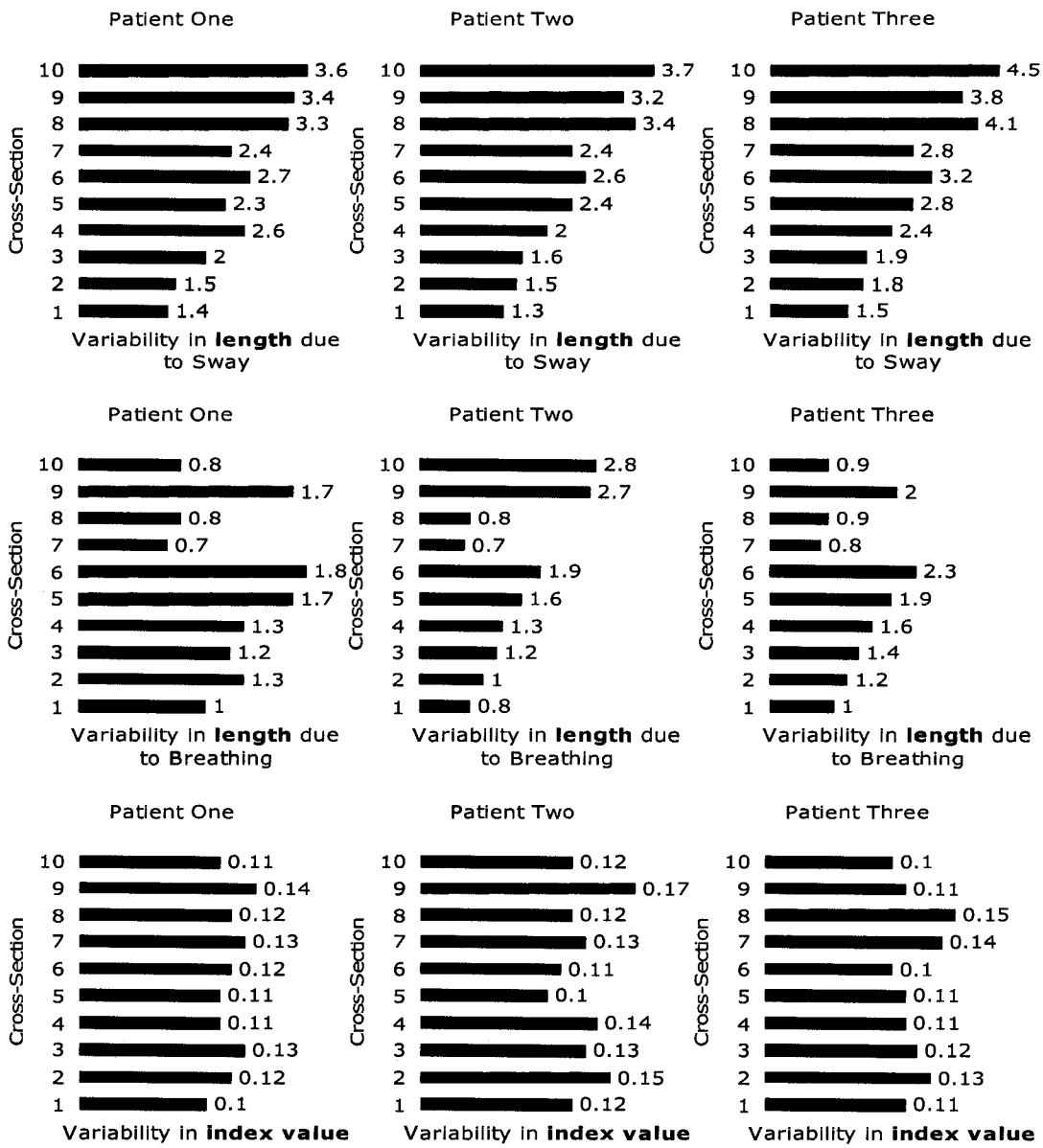

Fig. 9.5: Variability in the dimensions and index values due to sway and breathing in points.

deviations in the variability due to sway for all the cross-sections was termed the overall variability due to sway. The standard deviations in the variability due to breathing or shape were calculated similarly. Table 9.7 shows the system response to the effect of sway assessed from the ratios of the overall variability due to sway and the overall variability in the shape index value. The system response to breathing was assessed in a similar fashion.

Table 9.7: The high *ratios* indicate a low system response to the effect of sway and breathing.

		Patient One	Patient Two	Patient Three
Average Shape Index variation		0.0120	0.0202	0.0169
Average variations due to	Sway	0.7613	0.8293	1.0185
	Breathing	0.4057	0.7671	0.5292
Variation ratio due to	Sway	33.9	37.9	31.4
	Breathing	63.6	41.0	60.4

9.5.3 Variability of clinically relevant indices

Fig. 9.6 shows three views of two of the ten models used to evaluate the variability of clinically relevant indices. Table 9.8 shows the deformation index values for the shape based indices: twist, bend and tilt, and the landmark index: cosmetic score, assessed from three repeat acquisitions of the torso images of ten scoliosis volunteers. The shape-based deformity indices were calculated using the four horizontal segment-structured splines models of each image.

From Table 9.8, the standard deviations in the landmark-based index (Cosmetic Score) was about 6% of the average index values while the standard deviations in the shape-based indices were generally around 2-3% of the average index values. This difference suggests that the Cosmetic Score shows more variability than the shape-based indices.

9.5.4 Relative information contents of front and back torso images

Table 9.9 shows the variation in the distributions of twist, bend and tilt values for back torso, front torso and full torso images of 43 scoliosis volunteers. From the table, back torso images showed more variation than front torso images. Table 9.10 shows the relative information content of the back and front torso images. The ratio of the information content is on average 3 to 1 in favour of the back torso image.

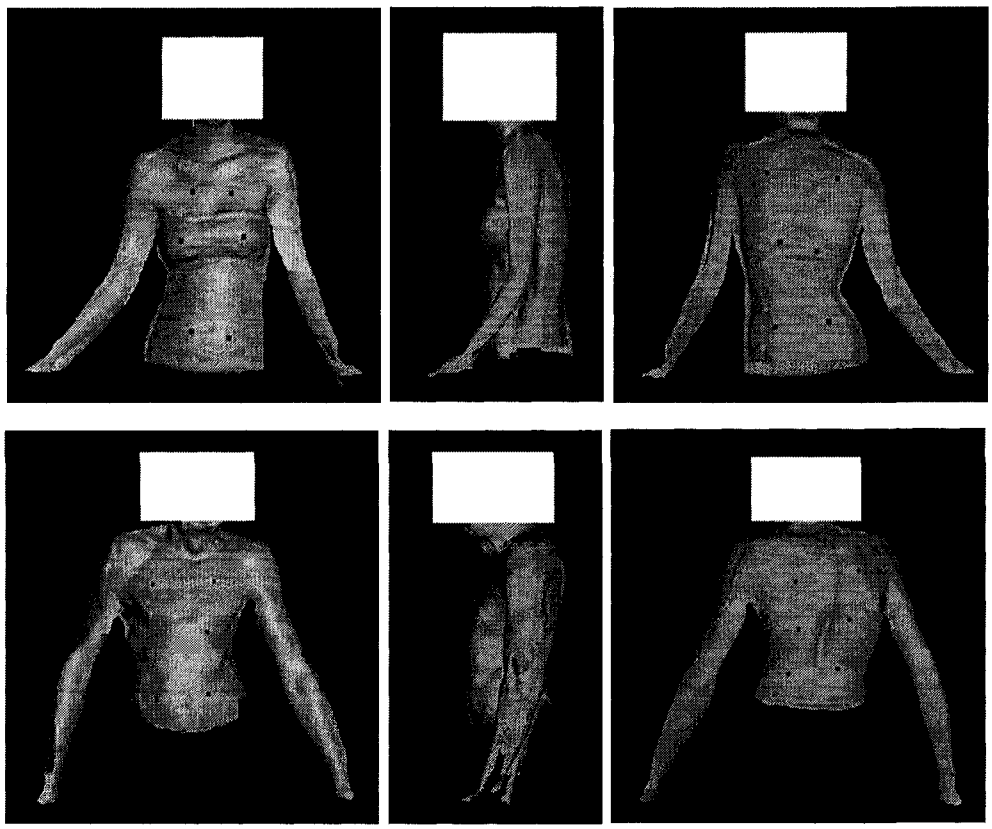

Fig. 9.6: Three views of the torso images of two of the ten patients (patients one and three) showing the centroids on the right and left parts of the three horizontal segments.

Table 9.8: The deformation index values of the ten patients in deformation points.

Volunteer	Av. Twist Ψ_T		Av. Bend Ψ_B		Av. Tilt Ψ_A		ACS	
	Score	SD	Score	SD	Score	SD	Score	SD
One	24	1	42	1	36	2	74	10
Two	-19	2	27	2	16	3	28	8
Three	32	3	-60	3	-43	1	54	6
Four	25	2	-45	1	37	1	50	8
Five	20	2	22	1	18	2	70	12
Six	30	1	26	2	41	3	50	4
Seven	18	1	26	2	34	4	26	5
Eight	41	1	38	2	16	5	66	10
Nine	54	2	24	1	28	1	42	4
Ten	17	1	12	2	42	2	20	5

Av.: Average; SD: Standard Deviation; MCS: Modified Cosmetic Score is the cosmetic score X 20.

Table 9.9: The variations in the deformation index distributions (in deformation points).

	Twist	Bend	Tilt
Back Torso Image	2.7508	3.5292	3.4464
Front Torso Image	0.9718	0.6992	1.3499
Full Torso Image	1.7670	2.1705	2.2211

Table 9.10: The relative information content of the back and front torso images (in %).

	Twist	Bend	Tilt	Average*
Back Torso Image	74	83	72	76
Front Torso Image	26	17	28	24
Total	100	100	100	100

*The standard deviation in the back and front torso images is 5.8.

9.6 DISCUSSION

The accuracy of reproduction of a complete torso imaging system was evaluated using a test-box and a mannequin whose shape was modelled from an actual scoliosis torso. Results showed that there was a significant difference between measurements made with the sides of the test box aligned perpendicular to the line of sight of the digitizer and those obtained with the line of sight 45^0 to the line of sight of the digitizer. This may be explained by the non-uniform effect of light on the inclined surfaces of the test-box in the 45^0 position and may be particular to our setup.

It was qualitatively observed that subtle changes in the external lighting of the *acquisition room* and varying reflectance of the test surface introduced small random errors in the measurements. Errors due to lighting can be controlled by eliminating sources of external lighting and using a controlled amount of artificial light. In general, the lighting conditions should be adjusted for each person before every scanning session bearing skin characteristics in mind. Using a two-digitizer

configuration improved the repeatability of the system by 20% over the one-digitizer configuration. Re-positioning increased the errors associated with the system by 30%. Overall, the accuracy of the 3D reconstruction system evaluated from the test-box and mannequin was found to be adequate for analysis of human torso asymmetry. It was observed that the accuracy of the two-digitizer system was significantly better than that of the single digitizer system. A four-digitizer system may provide better results than a two-digitizer system.

The system response to sway and breathing was evaluated from three repeat acquisitions of the torso shapes of three non-scoliosis volunteers. Analysis (Fig. 9.5) shows that the variability due to sway increases from the waist upwards to the shoulders. This suggests that the torso is most stable at the waist. The variability due to breathing however does not show such as clear pattern. Table 9.7 shows a comparison of the variability in the shape-based deformation index values of the three volunteers to the variability in the positioning of the cross-sections due to sway and the variability in the dimensions of the cross-sections due to breathing. The *variation ratio*, which is the ratios of the aforementioned variability, shows that shape changes due to sway and breathing is much smaller than the actual changes in position and dimensions due to sway and breathing.

Table 9.8 compares the shape-based deformation indices (twist, bend and tilt) to a landmark-based deformation index (Modified Cosmetic Score). The modification to the Cosmetic Score was to multiply it by 20 so that its range can be comparable to those of the shape-based indices. Analysis shows that shape-based deformation indices are much less variable than the landmark-based index. This is because shape-based deformation indices are much less affected by the effect of posture, positioning and sway. Also, difficulties in consistently locating torso landmarks add errors to the calculation of landmark-based indices.

Tables 9.8 and 9.9 show the variation in the distribution of the deformation indices for back torso, front torso and full torso images as well as the relative information content of the back and front torso images. Back torso images, on average, contain up to three times the amount of information contained in front torso images. Though the use of back torso images rather than full torso images would result in a loss of only a quarter of the available information in the torso shape, a hidden advantage of using full torso images is that they are more resilient to the effect of posture on the torso indices obtained. For example, if a patient is leaning forward during the image acquisition, their back torso image alone would appear to have an exaggerated tilt. The effect of leaning forward is however lost if the full torso image is analyzed.

9.7 CONCLUSIONS

A complete torso image acquisition system was designed and evaluated. Experiments using a test-box and a mannequin led to better understanding of the system accuracy. Experiments with three volunteers who do not have scoliosis and with ten scoliosis volunteers shed more light on the system response to the effect of sway and breathing, an intractable problem in torso imaging, and the variability of clinically relevant indices. Landmark-based indices showed more variability than shape-based indices, suggesting that shape-based indices may be more reliable. The relative information contents of the front-torso and back-torso images were assessed. Back torso images were found to contain, on average, up to three times the amount of information contained in front torso images. Thus, the use of back torso images alone in the analysis of torso deformities caused by scoliosis means forfeiting up to a quarter of the available information. An additional advantage of using full torso images is that they provide robustness to variations in clinically relevant indices such as tilt.

REFERENCES

1. V. J. Raso, E. Lou, D. L. Hill, J. K. Mahood, M. J. Moreau, N. G. Durdle, 'Trunk distortion in adolescent idiopathic scoliosis', *Journal of Paediatric Orthopaedics*, vol. 18, no. 3, pp 222-226, 1998.
2. N. Suzuki, K. Inami, T. Ono, K. Kohno, M. A. Asher, 'Analysis of Posterior Trunk Symmetry Index (POTSI) in scoliosis: Part 1,' *In Research into Spinal Deformities 2*, 81-4, 1999.
3. A. R. Turner-Smith, J. D. Harris, G. R. Hougton, R. J. Jefferson, 'A method of analysis of back shape in scoliosis', *Journal of Biomechanics*, 21, pp. 497–509, 1998.
4. X. C. Liu, J. G. Thometz, R. M. Lyon, J. Klein, 'Functional classification of patients with idiopathic scoliosis assessed by the Quantec system,' *Spine*, 26(11), pp. 1274-79, 2001.
5. J. L. Jaremko, P. Poncet, J. Ronsky, J. Harder, J. Dansereau, H. Labelle, R. F. Zernicke, Indices of torso asymmetry related to spinal deformity in scoliosis, *Clinical Biomechanics*, 17, pp. 559–568, 2002.
6. J. L. Jaremko, P. Poncet, J. Ronsky, J. Harder, J. Dansereau, H. Labelle and R. F. Zernicke, 'Estimation of spinal deformity in scoliosis from torso surface cross sections,' *Spine*, vol. 26, no. 14, pp 1583-1591, 2001.
7. P. O. Ajemba, N. G. Durdle, D. L. Hill, and V. J. Raso, 'A torso imaging system for quantifying the deformity associated with scoliosis,' *IEEE Transactions on Instrumentation and Measurements,* vol. 56, no. 5, October 2007.
8. P. O. Ajemba, N. G. Durdle, D. L. Hill, and V. J. Raso, 'A Torso Imaging System for Quantifying the Deformity Associated with Scoliosis,' *In Proceedings of the IEEE Instrumentation and Measurement Technology Conference*, Ottawa, 17–19 May, 2005.

CHAPTER 10

CONCLUSIONS

This thesis describes the research and development of the structured splines model, a method for analyzing, quantifying and tracking the shape of 3-D objects based on their curvature and symmetry. Structured spline modelling brings together and expands on ideas from mathematical shape analysis, computer engineering and biomedical image analysis. It possesses the following properties: 1) intuitiveness – it is based on features of an object that are most relevant to its visual perception; 2) relatability - it yields indices that can be understood in terms of the common description of shape such as bend, twist and tilt; 3) practicality – it accepts range images of objects, a form of input that is available from most segmentation or image acquisition applications; 4) error-correction – it corrects such errors in the input data as holes and stray points.

In this chapter, the major contributions of this thesis are highlighted and some suggestions for future work presented.

10.1 OVERALL ACHIEVEMENT

A review of the relevant literature (Chapter 2) described the existence of two gaps. First, there was a need to develop a shape analysis method that intuitive, practical, relatable and error-correcting [1]. Second, there was a need to apply shape-based analysis to the assessment of torso deformity in scoliosis management [2]. This thesis fulfilled those two needs.

First, an imaging system was developed for use in the acquisition of the torso topographic images of scoliosis and non-scoliosis patients (Chapter 7) and pre-processed (Chapter 8). These images were used for model development and clinical

validation. Second, three shape analysis methods were developed: 1) *Orthogonal mapping*, which involved performing a cylindrical to Cartesian coordinate transformation on torso images (Chapter 5); 2) Point-set data, which involved calculating points of high curvature on the object's surface (Chapter 6); 3) Structured splines modelling, which makes use of curvature information extracted from structured cross-sections of objects (Chapter 3). Third, three sets of deformation indices corresponding to each of the shape analysis methods described above were developed (Chapter 4). The shape analysis methods and their corresponding deformation indices were then applied to the shape-based assessment of torso deformity in scoliosis. Finally, the overall system is evaluated using the developed curvature-based shape analysis method (Chapter 9).

10.2 MAJOR CONTRIBUTIONS

The major contributions of this thesis span three fields: mathematical shape analysis, computer engineering and biomedical image analysis.

1. Mathematical shape analysis – this thesis developed a framework for multi -scale shape analysis using *B*-spline basis functions and presented a description of the relationship between the Gaussian scale space and the *B*-spline scale space.
2. Computer engineering – this thesis presents a procedure for analyzing the shape of three-dimensional objects using their structured splines models. It also presents procedures for describing the shape of three-dimensional objects using a multi-dimensional deformation index, and for analyzing three-dimensional shapes that incorporate hole-filling and error correction of range images.
3. Biomedical image analysis – this thesis presents an intuitive, descriptive and practical tool for assessing and describing the torso deformity caused by scoliosis and tools for quantifying and tracking torso deformity and clinical management of scoliosis.

10.3 SUGGESTED FUTURE WORK

This thesis presents a shape analysis method that is intuitive, relatable, practical and error-correcting. Suggested future work arising from this thesis includes:

1. Integrating the modules into a graphical user interface: To better appreciate the suite of software developed in this thesis, the software should be organized and re-implemented using a user-friendly graphical user interface.
2. Improving the range acquisition system: This could be achieved by making use of up to four digitizers rather than two. The digitizer should also have a resolution higher than 1mm.
3. Applying structured splines models to other areas: The concepts described in this thesis can be applied to other areas of study. Currently, applications are being envisaged for areas such as medicine and computer vision. Medical applications include the use of structured splines models to achieve shape based tracking of the motions of organs such as the heart. Applications in computer vision include performing the biometric identification of faces from their structured splines models.

REFERENCES

1. P. O. Ajemba, N. G. Durdle, and V. J. Raso, 'Quantifying torso deformity using dominant points obtained from structured splines models,' Submitted to *IEEE Transactions on Image Processing*, 2007.
2. P. O. Ajemba, N. G. Durdle, and V. J. Raso, 'Quantifying and tracking torso deformity using dominant points of structured splines models,' Submitted to *IEEE Transactions on Medical Imaging*, 2007.

APPENDIX 1

A SUPPORT VECTORS CLASSIFIER APPROACH FOR PREDICTING THE RISK OF PROGRESSION OF ADOLESCENT IDIOPATHIC SCOLIOSIS[N]

A1.1 INTRODUCTION

Adolescent Idiopathic Scoliosis (AIS) is a condition involving lateral deviation and rotation of the spine causing visible asymmetries of the trunk [1]. It affects between 2 – 4% of adolescents and its aetiology is still unclear. A goal of current research work by our group is to develop decision support systems for predicting the risk of progression of AIS using artificial intelligence and machine learning techniques. The most common protocols employed in the management of AIS are surgical intervention and bracing. Surgical intervention is usually carried out to halt the increase in deformity and reduce the abnormal curvature of the spine without injury to the spinal cord [2]. Bracing is usually done to check the increase in deformity during the high-risk adolescent growth spurt and delay surgical intervention [3].

The most common indicator of AIS is the Cobb angle [4], a radiographic indicator obtained from posterior-anterior (PA) radiographs of the spine. The Cobb angle is measured between the endplates of the upper and lower vertebrae of the scoliotic curve. Seventeen common radiographic indicators including the Cobb angle (known as the Lenke set of indicators) were accumulated by Lenke *et al.* while developing a new classification system for AIS [5], [6] (Table A1.1). Our group is examining the

[N] A version of this chapter has been published. P. O. Ajemba, L. Ramirez, N. G. Durdle, D. L. Hill and V. J. Raso, 'A support vectors classifier approach to predicting the risk of progression of adolescent idiopathic scoliosis,' *IEEE Transactions on Information Technology in Biomedicine*, vol. 9, no. 2, pp. 276 – 282, June 2005.

Table A1.1: Listing of Lenke radiographic indicators

Parameter	Mean (Standard Deviation)			Range		
	I	II	III	I	II	III
1 Proximal thoracic Cobb angle	18.2 (6.9)	17.8 (6.9)	18.9 (7.0)	6–34	6–34	8–34
2 Main thoracic Cobb angle	28.9 (9.3)	29.0 (9.6)	28.6 (9.2)	11–47	11–47	16–44
3 Thoracolumbar/Lumbar angle	25.7 (9.3)	26.3 (10.3)	24.4 (6.7)	5–49	5–49	13–32
4 Thoracic apical vertebrae+	20.2 (15.5)	20.916.3	18.6 (14.1)	-25–57	-25–57	-5–45
5 Lumbar apical vertebrae +	-13.5 (16.6)	-14.0 (17.7)	-12.2 (14.4)	-64–39	-64–39	-33–23
6 Coronal decompensation+	-7.5 (13.0)	-7.0 (14.2)	-8.5 (10.2)	-33–24	-33–24	-27–6
7 T1 tilt angle	1.8 (6.0)	1.9 (6.5)	1.6 (5.2)	-8–12	-8–12	-8–8
8 Sagittal T2-T12 Cobb angle	22.3 (9.9)	22.5 (8.4)	21.9 (12.9)	2–43	5–43	2–43
9 Sagittal T2-T5 Cobb angle	8.0 (5.2)	8.5 (5.2)	7.0 (5.2)	0–21	2–21	0–18
10 Sagittal T5-T12 Cobb angle	14.4 (9.0)	14.3 (8.1)	14.8 (11.1)	0–35	0–35	0–35
11 Sagittal T10-L2 Cobb angle	9.1 (6.5)	8.5 (5.7)	10.5 (8.1)	0–33	2–24	0–33
12 Sagittal T12-S1 Cobb angle	51.3 (13.2)	49.3 (13.9)	55.4 (10.8)	18–76	18–76	40–71
13 Sagittal balance C7-sacrum+	-5.2 (33.8)	0.0 (36.3)	-15.6 (25.9)	-60–87	-60–87	-56–34
14 Gross Risser Grade++	1.6 (0.5)	1.7 (0.5)	1.1 (0.3)	1–3	1–3	1–2
15 Maximum Vertebral Rotation	1.7 (0.6)	1.6 (0.6)	1.8 (0.8)	0–2.5	0–2.5	1–2
16 Spondylolysis	0.1 (0.5)	0.2 (0.5)	0.1 (0.3)	0–2.5	0–2.5	0–1
17 Wrist X-ray+, +++	12.8 (1.1)	13.5 (1.1)	12.0 (1.0)	10–17	10–17	10–13
18 Chronological age*	12.3 (1.4)	12.6 (1.5)	11.8 (1.1)	10–15	10–15	10–13
19 Sex (0=Female, 1=Male) *	+	+	+	0–1	0–1	0–1
20 Growing? (0=No, 1=Yes) *	+	+	+	0–1	0–1	0–1

+: Not applicable. *: Index is not part of the Lenke set. +Index is not bounded. ++The Gross Risser Grade is our clinical modification of the Risser Grade. 1 = Risser 0 or 1 (Immature); 2 = Risser 2 or 3 (In transition); and 3 = Risser 4 or 5 (Mature). +++The Wrist X-ray replaces Lenke's Triradiate Cartilage that we are unable to measure due to X-ray cropping

inter- and intra-observer variability of measuring the individual Lenke indicators and results obtained so far are encouraging. For more on the manifestation and treatment of AIS the reader is referred to the Scoliosis Research Society website [7].

Since AIS has an unclear aetiology, its risk of progression (the principal determinant of its treatment options) can only be assessed from its indicators. For this study, progression of AIS was deemed to be a five-degree increase in Cobb angle [8]. Many researchers believe that indicators such as chronological age, bone

age, curve size and the stage of development of the apophysis of the iliac crest – the Risser sign (or grade) [9] – are associated with the risk of progression of AIS [8], [10], [11], [12], [13].

Complex indicators such as spinal imbalance [10], rate of growth of the spine [11] and the angle between the plane of maximum deformity and the front-back axis [14] have been shown to predict scoliosis progression with varied success. As most indicators yield at best partial results, some researchers have used statistical combinations of indicators from different sources [8], [10], [11] to obtain better results. However, obtaining the value of most of these indicators is arduous and involves much skill and repeated measurements taken over time and often subject to unknown inter- and intra-observer variability. Thus, getting results from predictive models based on them is very time consuming, making them difficult to use in a clinical setting.

Machine learning (ML) techniques have not been applied to predicting the risk of progression of AIS. We believe that combining a number of common indicators from one source (such as the Lenke set of radiographic indicators) with some ML based analytical tools such as support vector classifiers (SVC) [15]; we can develop a fast predictive tool that could be used in a clinical setting.

In this study, using a SVC, we investigate the possibility of predicting the risk of progression of AIS in patients with moderate curves (20–45 degrees) from Lenke indicators and clinical variables. A SVC was chosen because, unlike techniques such as Artificial Neural Networks, the support vector theory offers the possibility to train generalizable, non-linear classifiers in high-dimensional space using small training sets [16] as is usually the case in scoliosis research. Finally, finding no comparable ML model, we compare the result of applying our SVC to three datasets of scoliosis patients to that obtained by applying a "substantially equivalent" [17] binary logistic regression (BLR) model and a stepwise linear regression (SLR) model [18] to the

datasets to fulfill the requirement of comparability needed for decision support systems [17].

A1.2 MATERIALS AND METHODS

A1.2.1 Patient datasets

Retrospectively, radiographs and clinical records of AIS patients from the database of the scoliosis clinic at Glenrose Rehabilitation Hospital were examined to select patients for the study. The following inclusion criteria were used: (1) A diagnosis of AIS; (2) Age at initial clinical visit of at least 10 years; (3) Clear standing posterior-anterior (PA) and lateral radiographs with a maximum Cobb angle of 20-45 degrees; (4) A follow-up period of one year from first clinical visit if the curve progressed or to skeletal maturity (as shown by a Risser sign of 4 or 5, wrist X-ray showing a bone age of 15-17 years or an increase in height of less than 2cm/yr) if the curve did not progress. To be admitted to the scoliosis clinic, the patients are deemed to be at risk of progression.

Forty-four patients satisfied the inclusion criteria and were placed in group I. Of these, 38 (87%) were girls. The mean age of the group was 12.3 ± 1.4 years (range 10 – 15) and the mean maximum Cobb angle was 32 ± 8 degrees (range 18 – 49). Of the 44, 31 patients (70%) had progressive curves. To isolate the effect of bracing (if any) on the risk of progression of AIS, the 30 patients in group I who were not braced (observed patients) were placed in group II and the remaining 14 patients were placed in group III. Of the 30 observed patients, 22 had curves with maximum Cobb angles greater than 30 degrees but were not braced either because they refused bracing or their surgeons deemed that brace-wear would not be effective in their case (for instance, some had passed their adolescent growth spurt period at their first visit to the clinic). Six patients who were prescribed braces were placed

with the observed because their surgeons noted them to be clearly non-compliant to wearing their braces.

Seventeen pre-operative Lenke indicators were measured for each of the 44 patients from PA and lateral radiographs. These indicators in addition to chronological age, sex and a dichotomous indicator "growing" (1, if increase in height $\geq$ 2cm/year in the year after first visit to the clinic; 0, otherwise) made up the 20 features of datasets II and III. Dataset I contained, in addition, another dichotomous indicator "bracing" (1, if patient was braced; 0, otherwise). Table A1.1 shows statistical information of these indicators.

A1.2.2 Support vector classifiers

Support vector classifiers, originally designed to solve two-class classification problems, have been used with a measure of success in such applications as storm cell classification [19]. In this approach, a margin is created between the classes and around the decision boundary. The margin is defined by the distance to the nearest training patterns known as support vectors which define the classification function. The aim of training is to maximize the margin between classes thereby minimizing the number of support vectors chosen to define the decision boundary described in [16] as:

$$D(x) = \sum_{\forall x_i \in S} \alpha_i \lambda_i K(x_i, x) + \alpha_0 , \qquad (1)$$

where $K(x_i, x)$ is the kernel function (for example, for a linear kernel, $K(x_i, x) = (x \cdot x_i)$) of a pattern to be classified x and a training pattern x_i. S is a subset of the training set (the support vector set), and $\lambda_i \in \{-1, 1\}$ is the label of pattern x_i. As described in [16], during training, optimization of $\alpha_i \geq 0$ is achieved by:

$$\min_{\alpha}(\alpha^T \Lambda K \Lambda \alpha + C\sum_j \varepsilon_j), \qquad (2)$$

constrained by $\lambda_i D(x) \geq 1 - \varepsilon_j$, $\forall x_j$ in the training set. Λ is a diagonal matrix containing the labels λ_j and the matrix K stores the values of the kernel function K(xi, x) for all pairs of training patterns. ε_j are slack variables which allows for class overlap, controlled by the penalty weight C>0. For C $\rightarrow \infty$, no overlap is allowed. During optimization, the values of all α_i become 0, except for those associated with the support vectors. Consequently the support vectors are the only ones that are finally needed in deciding the position of the decision boundary.

Sequential minimal optimization [20] with radial basis and linear kernels was used to train the dataset. To select the appropriate values for C and γ (the spread for the radial basis kernel), a process of 3-fold cross-validation of the dataset was carried out. The sets of parameters used in the cross-validation were: C $\in \{0.1,1,10\}$ and $\gamma \in \{2^{-1},2^{-2},2^{-3}\}$.

A1.2.3 Statistical analysis

As the datasets are samples from the general population of scoliosis patients, known correlations between features of the general population and progression were verified to check that the samples are representative of the population. These features include developmental status (chronological age and Risser grade) and maximum Cobb angle [8], [10]. This was done by determining the percentage of progressive curves for various ranges of values of those features.

A1.2.4 Training and testing the SVC models

As a preprocessing stage, the data for the experiments were normalized to attain a

zero mean and one standard deviation. Principal component analysis (PCA) (Fig. A1.1) and Pearson's correlation analysis were performed on each dataset for the purpose of feature selection. Due to the paucity of data samples (44, 30 and 14 for datasets I, II and III respectively), training and testing were done using the leave-one-out method and the results were averaged. Six models based on a SVC (SVC1–SVC6, Table A1.2) were used. These models utilized different combinations of features (all the features, top features obtained from PCA, and top features obtained from Pearson's correlation analysis) and kernel functions (radial basis and linear kernels). A voting model, SVC-Voting, based on three of the better performing SVC models was also used. The output of the model was the majority vote (2-1 or 3-0) of the outputs of SVC4-6. For the BLR model, best results were obtained by training in the forward conditional mode. In comparing the BLR and SLR models to the SVC models, the "gold standard" [24] was the actual outcome of the patients (whether they progressed or not).

A1.3 RESULTS

This section compares the results, in testing, of the SVC models with those of the BLR and SLR models and evaluates their performance. Results of investigating the correlation between developmental status and maximum Cobb angle to the risk of progression in the datasets confirmed that the risk of progression reduces with increase in developmental status and increases with maximum Cobb angle. For instance, 12/14 (90%) of the 10- and 11-year old patients in the datasets had progressive curves while only 3/8 (40%) of 14- and 15-year olds progressed.

The results of classifying the curves into progressive and non-progressive curves

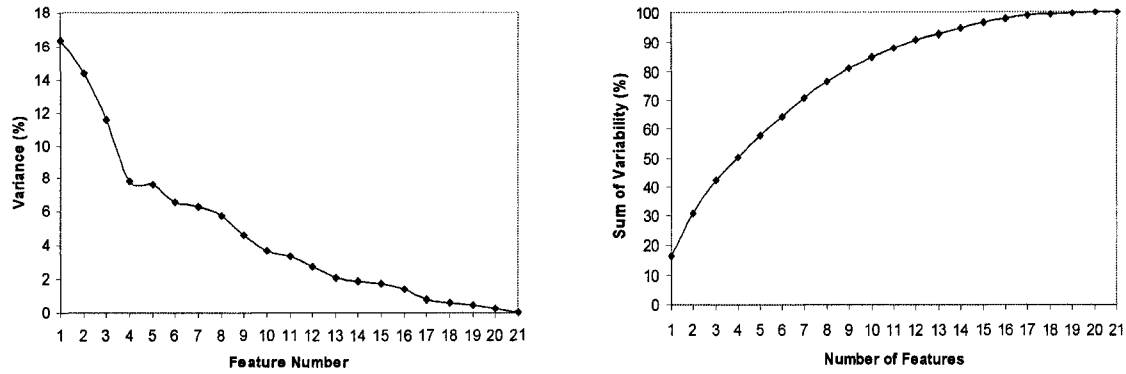

A

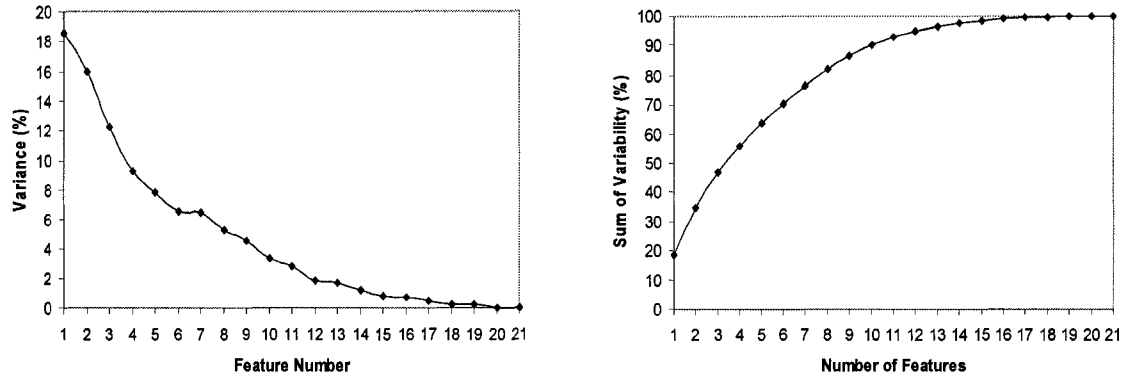

B

Fig. A1.1: Plots of variance per feature and cumulative variance A, Dataset I: The top seven feature account for up to 70% of the variability in the dataset. B, Dataset II: The top seven feature account for up to 80% of the variability in the dataset.

Table A1.2: Selections of features used to train the SVC

Selection	Criteria Used	Features Selected (Feature Numbers)	Kernel Used
SVC1	All features	All	Radial Basis
SVC2	All features	All	Linear
SVC3	PCA features explaining at least 10% of total Variance	Between 7 and 21 features may be used	Radial Basis
SVC4	PCA features explaining at least 10% of total Variance	Between 7 and 21 features may be used	Linear
SVC5	Features with correlation to progression statistically significant at $p<0.05$	Dataset I: 8 and 18; Dataset II: 1, 2, 4, 14, 17, 18 and 20; Dataset III: 13 and 17	Radial Basis
SVC6	Features with correlation to progression statistically significant at $p<0.05$	Dataset I: 8 and 18; Dataset II: 1, 2, 4, 14, 17, 18 and 20; Dataset III: 13 and 17	Linear

are summarized in Table A1.3. SVC-Voting and SVC4 outperformed other SVC models and the BLR and SLR models with an accuracy of 78 and 80% for databases I and II, compared to 73 and 73 % respectively for SVC4, 68 and 70% for SVC6, 66 and 70% for SVC5 and 66 and 67% for SVC3. As the number of features in dataset III exceeded the number of records, PCA could not be applied so SVC3 and SVC4 could not be used on dataset III. Four SVC models (SVC3, SVC4, SVC5 and SVC6) classified datasets I and II with accuracies 65-73%. SVC-Voting was based on three of these models (SVC4-6). SVC5 and SVC6 classified dataset III with 79% accuracy. The BLR model achieved accuracies of 61, 60 and 57% for datasets I, II and III compared to 50, 52 and 50% for the SLR model.

Table A1.4 shows the detailed classification of patients in datasets II using the SVC4 and SVC-Voting models. It can be seen that the SVC4 and SVC-Voting correctly classified 91% and 86% of progressive curves respectively, in dataset II. Of the 44 records in database I, 23 (53%) were correctly classified by all the models (SVC, BLR and SLR) while 6 (14%) were misclassified by all. Detailed result of determining the risk of progression in dataset II using the SVC models are shown on Tables A1.5.

A1.4 DISCUSSION

Six models based on a support vector classifier (SVC1-6) were used to predict the risk of progression of AIS from radiographic and clinical indicators. A seventh model, SVC-Voting, whose output was the majority vote of the outputs of SVC4-6, was also used. Results obtained showed that five of the seven models (SVC3–6 and SVC-Voting) achieved classification accuracies 65-80% in testing and 100% in training on the datasets used, outperforming a "statistically equivalent" [17] BLR model and an SLR model [16]. The models also outperformed other models based on combinations of indicators from various sources proposed in the literature [8], [10]. In [10], a

Table A1.3: Test results (% accuracy) with the SVC, BLR and SLR models

Accuracy	SVC1	SVC2	SVC3	SVC4	SVC5	SVC6	SVC-Voting	BLR	SLR
Dataset I	64	61	66	73	66	68	78	61	50
Dataset II	70	67	67	73	70	70	80	60	52
Dataset III	71	50	NA+	NA+	79	79	71	57	50

+: Not Applicable: Cannot apply PCA because dataset III has more features (20) than records (14)

Table A1.4: Test results of classifying Dataset II using the SVC4 and SVC-voting models

Actual \ Predicted	SVC4			SVC-Voting		
	P	NP	Total	P	NP	Total
Progressive	19 (91%)	6 (67%)	25	18 (86%)	3 (33%)	21
Non-progressive	2 (9%)	3 (33%)	5	3 (14%)	6 (67%)	9
Total	21	9	30	21	9	30

P: Progressive; NP: Non-progressive

Table A1.5: Results of determining the risk of progression in dataset II

	SVC1	SVC2	SVC3	SVC4	SVC5	SVC6	SVC-Voting
Accuracy (%)	70	67	67	73	70	70	80
False negative	2	4	7	2	2	3	3
False Positive	7	6	3	6	7	6	3
Sensitivity	0.91	0.81	0.67	0.91	0.91	0.86	0.86
Specificity	0.22	0.33	0.67	0.33	0.22	0.33	0.67
Positive Predictive Value (PPV)	0.73	0.74	0.82	0.76	0.73	0.75	0.86
Negative Predictive Value (NPV)	0.50	0.43	0.46	0.60	0.50	0.50	0.67

logistic regression model was used to predict the risk of progression of AIS from a cohort of 159 girls (Cobb angels 25-35 degrees). The model achieved an accuracy of 81% in training.

A total of seven of the 20 indicators (21 for database III) chosen because of their high correlation to progression ($p<0.05$) were used by two models (SVC5 and SVC6).

The statistically equivalent BLR model and the SLR model needed 20 and 12 indicators respectively. Eight of the 20 indicators used (Proximal and Main thoracic Cobb angles, Gross Risser Grade, Wrist X-ray, Chronological age, AVT – Thoracic, Sagittal T2-T12 Cobb angle, Sagittal balance C7-sacrum and "Growing", Table A1.2) had statistically significant correlations with the risk of progression ($p<0.05$). This finding is similar to observations made in [8] and [10].

It was observed that 23 (53%) of the records in database I were correctly classified by all the models. 30 (68%) of the records were correctly classified by the top four models (SVC3–6). The relatively small number of records consistently misclassified by all the models may suggest these were "outliers" present in the datasets. If that were the case, it may be possible to obtain better results from a larger dataset having fewer of outliers. Though only eight indicators showed a statistically significant correlation to the risk of progression, the SVC-voting model achieved sensitivity and specificity values of 0.86 and 0.67, and NPV and PPV values of 0.86 and 0.67 and an accuracy of 80% (Table A1.5) on dataset II. As patients admitted to the clinic are deemed at risk of progression, improvements in PPV will translate to savings in healthcare costs as it will reduce the number of patients unnecessarily treated. Improvements in NPV will reduce the number of progressive patients whose clinical treatments are delayed.

The 20 indicators used in our study can be measured quickly (especially in the fast-paced clinical environment) and requires no pre-processing. It took less than 20 minutes per patient to measure the indicators, input their values into the system and produce the needed results. These findings suggest that a SVC-based decision support system may be viable for use in a clinical environment to aid in management of AIS at the initial clinical visits as the prediction results can be obtained quickly.

A1.5 CONCLUSION

Our study indicates that it may be possible to predict the risk of progression of AIS (to an accuracy of up to 80%) from radiographic indicators and clinical variables using a decision support system based on a SVC. This could be useful in the management of AIS in a fast-paced clinical environment. Once the initial radiographs and clinical data are acquired, the risk of progression can be assessed and an appropriate course of treatment chosen very quickly especially at the early stages of manifestation of AIS.

Results of statistical analysis (section A1.1.3) showed that our datasets (representing samples from the general population of scoliotic patients) exhibited trends similar to those found in the general population of scoliosis patients. Due to the low rate of occurrence of patients satisfying our inclusion criteria, we are currently pursuing a retrospective validation of our results on larger datasets of patients from other scoliosis clinics.

Future work will focus on studying more patients (to further assess the applicability of the SVC for clinical decision making), developing a better classification system based on the SVC, and incorporating additional information about prognostic factors for curve progression to improve the predictive capability of our system.

REFERENCES

1. V. J. Raso, E. Lou, D. L. Hill, J. K. Mahood, M. J. Moreau, and N. G. Durdle, "Trunk distortion in adolescent idiopathic scoliosis", *Journal Pediatr Orthoped*, vol. 18, no. 3, pp 222-226, 1998.
2. J. G. Lonstein, "Adolescent idiopathic scoliosis," *The Lancet*, vol. 344, pp 1407-1412, 1994.

3. E. Lou, D. Benfield, J. Raso, D. Hill, and N. Durdle, "Intelligent Brace System for the Treatment of Scoliosis," In TB Grivas (Ed.), *Research Into Spinal Deformities 4*, IOS Press, 2002.
4. J. R. Cobb, "Outline for the study of scoliosis, instructional course lectures," *The American Academy of Orthopedic Surgeons*, vol. 5, pp 261-275, 1948.
5. L. G. Lenke, R. B. Betz, J. Harms, K. H. Bridwell, D. H. Clements, T. G. Lowe, and K. Blanke, "Adolescent Idiopathic Scoliosis: A new classification to determine extent of spinal arthrodesis," *J. Bone and Joint Surg.*, vol. 83-A, no. 8, pp 1169-1180, 2001.
6. L. G. Lenke, R. B. Betz, D. Clements, A. Merola, T. Haher, T. Lowe, P. Newton, K. H. Bridwell, and K. Blanke, "Curve prevalence of a new classification of operative adolescent idiopathic scoliosis: Does classification correlate with treatment?" *Spine*, vol. 27, no. 6, pp 604-611, 2001.
7. Scoliosis Research Society, "Scoliosis Research Society Patient Information web site". Available at: http://www.srs.org. Accessed July 9, 2003.
8. J. E. Lonstein, and J. M. Carlson, "The prediction of curve progression in untreated idiopathic scoliosis during growth," *J. Bone and Joint Surg.*, vol. 66-A, pp 1061-1071, 1984.
9. J. C. Risser, "The iliac apophysis: an invaluable sign in the management of scoliosis," *Clinical Orthop.,* vol. 11, pp 111-119, 1958.
10. L. Peterson, and A. L. Nachemson, "Prediction of Progression of the Curve in Girls Who Have Adolescent Idiopathic Scoliosis of Moderate Severity", *Journal of Bone and Joint Surgery*, vol. 77A, no. 6, pp 823-827, 1995.
11. G. Duval-Beaupere, and T. Lamireau, "Scoliosis at less than 30 degrees. Properties of Evolutivity (risk of progression)," *Spine*, vol. 10, pp 421-424, 1985.
12. A. Nachemson, J. Lonstein, and S. L. Weinstein, "Prevalence and Natural History Committee Report," *Read at the Annual Meeting of the Scoliosis Research Society*, Denver, Colorado, September 22-25, 1982.
13. L. A. Karol, C. E. Johnston, R. H. Browne, and M. Madison, "Progression of the curve in boys who have idiopathic scoliosis," *J. Bone and Joint Surg.*, vol. 75-A, pp 1804-1810, 1993.
14. Y. Kohashi, M. Oga, and Y. Sugioka, "A New Method Using Top Views of the Spine to Predict the Progression of Curves in Idiopathic Scoliosis During Growth," *Spine*, vol. 21, no. 2, pp 212-217, 1993.
15. V. N. Vapnik, *Statistical learning theory,* New York, John Wiley & Sons, 1998.
16. A. K. Jain, R. P. W. Duin, and J. Mao, "Statistical Pattern Recognition: A Review," *IEEE Trans. Pattern Analysis and Machine Intelligence*, vol. 22, no. 1, pp 4-27, 2000.
17. A. E. Smith, C. D. Nugent, and S. I. McClean, "Evaluation of Inherent Performance of Intelligent Medical Decision Support Systems: Utilizing Neural Networks as an Example," *Artificial Intelligence in Medicine*, vol. 27, no. 1, pp 1-27, 2003.

18. P. O. Ajemba, N. G. Durdle, V. J. Raso, and D. Hill, "Assessing the Risk of Progression of Adolescent Idiopathic Scoliosis," *Proceedings of the 4th Biomedical Engineering Conference*, Banff, Alberta, Canada, October 24-26, 2003.
19. L. Ramirez, W. Pedrycz, and N. Pizzi, "Classification of severe storm cells using support vector machines," *In Roy R, Koppen M, Ovaska S, Furuhashi T, and Hoffmann F, eds., Soft computing and industry: Recent applications*, New York, Springer, 2002, pp 281-292.
20. J. Platt, "Fast Training of Support Vector Machines Using Sequential Minimal Optimization," In B. Scholkopf, C. J. C. Burges, and A. J. Smola, eds., *Advances in Kernel Methods - Support Vector Learning*, Cambridge, Mass., MIT Press, 1999.

APPENDIX 2

EFFECT OF POSTURE AND RE-POSITIONING ON TORSO IMAGING FOR SCOLIOSIS ASSESSMENT[N]

A2.1 INTRODUCTION

Complete torso images are becoming an important part of the comprehensive treatment available at clinics that treat scoliosis, a condition characterized by lateral deviation and rotation of the spine resulting in visible torso deformities. Scoliosis affects about 2–4% of adolescents, mostly girls [1]. Conventional methods of assessing idiopathic scoliosis are focused on evaluating the internal nature of the deformity–curvature of the spine, deformation of the ribcage and twist of the individual vertebrae. Thus, the most widely accepted indicator of scoliosis is the Cobb angle [2], measured from standing posterior-anterior radiographs of the entire spine. As most cases of late-onset idiopathic scoliosis will have no attendant health risks on the patient in the long run [3], the primary purpose of treatment is to improve torso appearance with its attendant social and psychological deprivation often of great concern to patients and their families [4]. Contact and non-contact surface imaging methods have been developed to assess scoliosis. Contact methods such as contour tracers [5] are generally limited in their use and low-cost, but provide limited information. Non-contact methods include back surface imaging methods based on optical techniques such as Moire [6], ISIS [7] and Quantec [8] systems. Recently, more costly full torso imaging systems utilizing multiple cameras and scanners to capture multiple views simultaneously, including InSpeck 3D digitizers, were

[N] A version of this chapter has been published. P. O. Ajemba, N. G. Durdle, D. L. Hill and V. J. Raso, 'Posture and re-positioning considerations of a complete torso topographic imaging system for assessing scoliosis,' *Research into spinal deformities 6*, 2006.

proposed. To reduce the cost of full torso imaging, a system utilizing a rotating positioning frame and a single Minolta VIVID 700 3D digitizer was developed [4]. The system requires four images taken at 90 degree intervals over 10 seconds to generate a torso image.

To better understand the output of torso imaging systems, their accuracies and factors that influence their performance need to be understood. In this paper the influence of posture and re-positioning (sway and breathing) on the accuracy of reproduction of a human torso topographic analysis system used in the clinical assessment of scoliosis was assessed. The accuracy of reproduction of the system for inanimate test objects was previously assessed as 1.1 ± 0.9mm [4].

The purpose of this study was to demonstrate that though the use of a rotating positioning frame introduces additional motion artifacts; their overall effect on the accuracy of reproduction of the system is within acceptable limits and outweighed by savings in cost [9], [10].

A2.2 MATERIALS AND METHODS

A2.2.1 Torso imaging system

The torso imaging system comprises a rotating positioning frame and a Minolta VIVID 700 3D digitizer (Konica Minolta Photo Imaging U.S.A., Inc.). The digitizer unit contained a camera and a laser scanner (Fig. A2.1). The laser scanner produces a near horizontal beam of light that is swept along the length of the object. The camera captures the contour of the beam as it is swept along. The deformation of the beam as it strikes the object and knowledge of the relative positions of the scanner and digitizer is used to compute the distance from the digitizer to each 3D point. The camera also captures a 3D texture map of the object. It takes about 0.6 seconds to scan one view of an object. The texture map of the scanned object aids

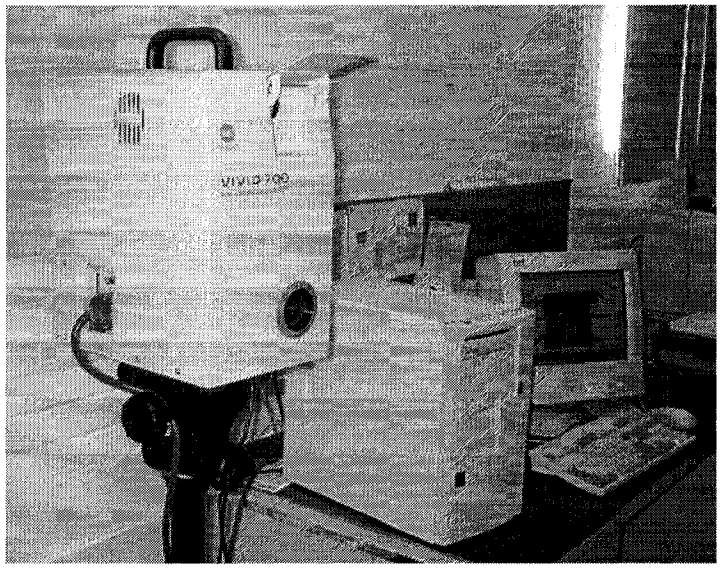

Fig. A2.1: The Minolta VIVID 700 digitizer

users during image editing procedures such as cropping the arms of generated models. To produce a full torso view, the digitizer was placed in four separate positions relative to the object to be scanned (Fig. A2.2) to capture its four orthogonal views. The four views were captured at three speeds (8, 10 and 12 seconds). Mesh objects generated from the 3D scans obtained from the four positions were stitched together to form the full torso model using an image registration technique. A spline interpolation algorithm was used to obtain the true surface at regions of overlap between the meshes.

A2.2.2 Data acquisition

Five male volunteers aged between 19 and 26 years who have no scoliosis were recruited for the study. The average age of the volunteers was 23.5 years. The experimental protocol was explained to the volunteers before the start of data acquisition and each gave their informed consent. The effect of posture on the accuracy of the torso imaging system was assessed from forty torso scans of all five volunteers. Each volunteer was imaged twice in four postures (free-standing, holding

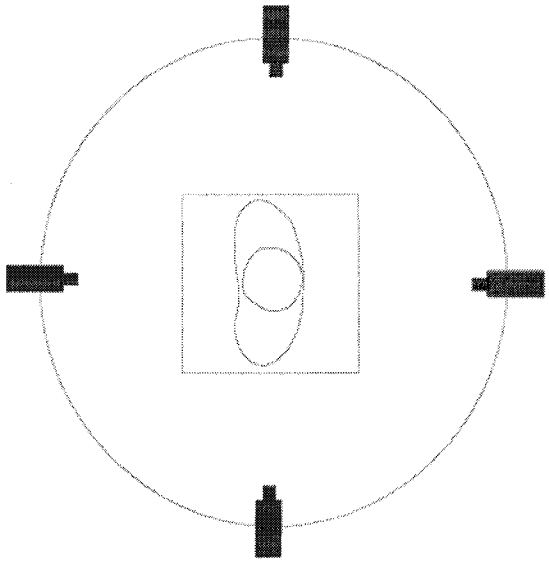

Fig. A2.2: The four positions of the digitizer

side supports, holding front supports and with their hands on their shoulders) at 30-minute intervals in a randomized manner. The volunteers were required to hold their breaths as each shot was taken and released their breaths as the positioning frame was moved to the next position after each shot. The volunteers provided structured qualitative feedback on the various postures and the kinematics of the imaging process (such as the speeds of rotation of the positioning frame).To assess the effect of repositioning (sway and breathing), two male volunteers (aged 20 and 27 years) having no scoliosis were each imaged 10 times holding the side supports at 30-minute intervals in a randomized manner. The posture was used because our preliminary experimental trials showed that it was associated with the least amount of errors compared to other postures. The volunteers were also required to hold their breaths as each shot was taken. Fig. A2.3 shows four views of a typical torso image obtained using the system.

A2.2.3 Data analysis

The arms of each torso image were cropped and twenty evenly-spaced cross-

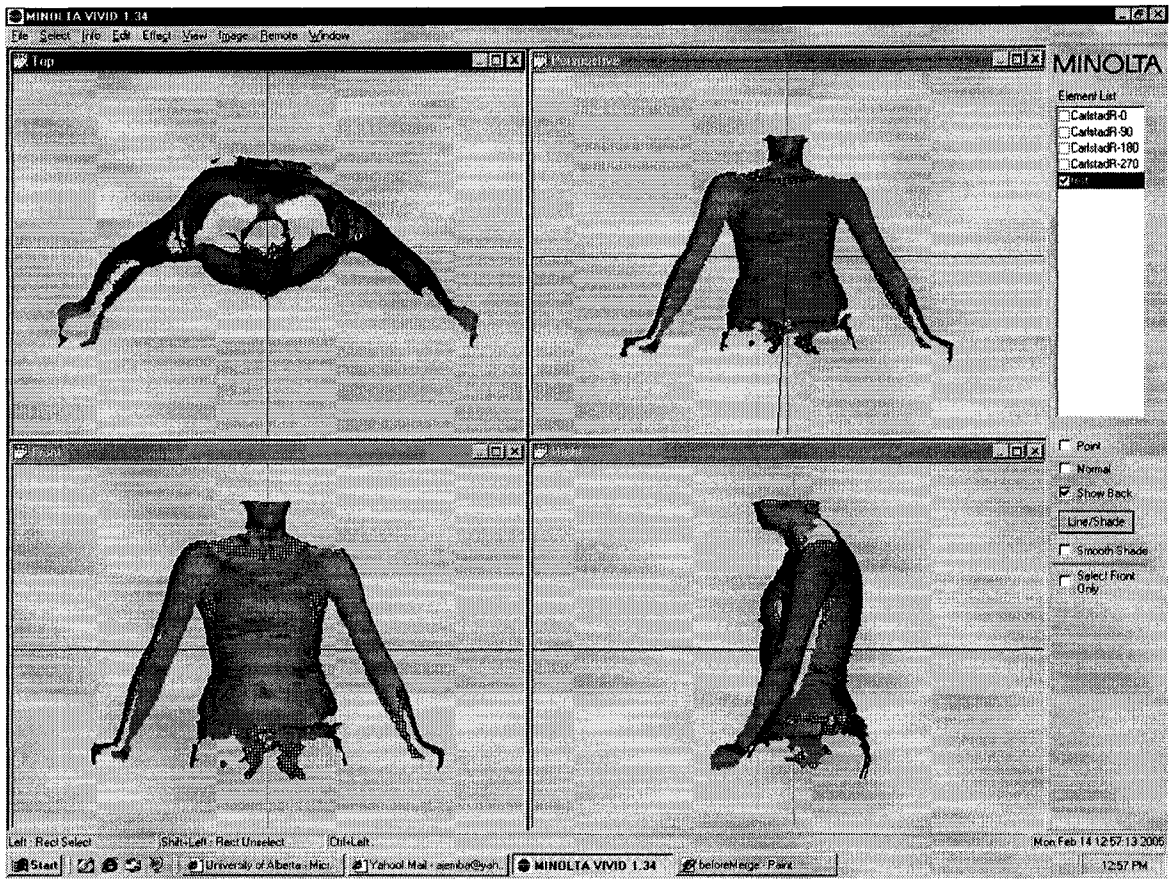

Fig. A2.3: Four views of a typical torso image

sections were computed starting from the bottom of the image. The coordinates $(\bar{x}, \bar{y})$ of the centroids of each cross-section were calculated from binary images of the sections by assigning to each pixel in the section an area of, say 1mm^2, and using the equations [11]:

$$\bar{x} = \frac{\sum x \cdot dA}{\sum dA}, \bar{y} = \frac{\sum y \cdot dA}{\sum dA}, \quad (1)$$

where dA represents the area of each pixel (x, y) (in this case, 1mm^2), and summing across the entire cross-section. A centroid line joining the centroids of the cross-sections was generated (Fig. A2.4).

The variability due to posture was assessed by computing the standard deviations and root-mean-square errors in the widths of each cross-section for each posture

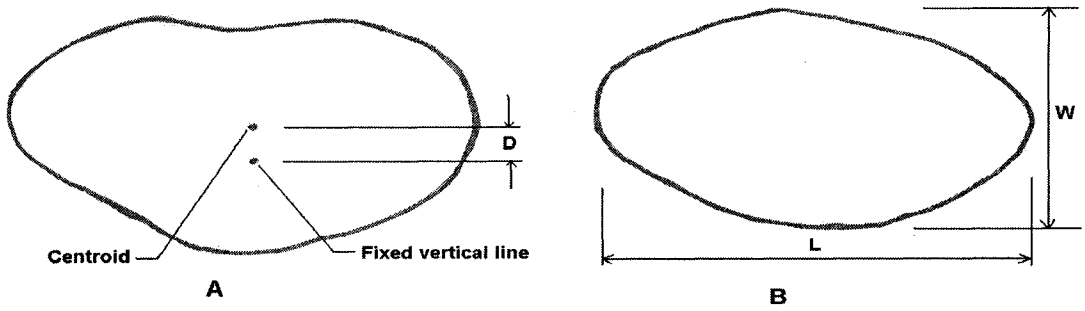

Fig. A2.4: A, Calculation of the variability due to sway. D is the offset of the centroid from the vertical axis. B, Calculation of the effect due to breathing. H and L are the height and width of the torso.

normalized for each volunteer. The distance D, between the centroid and a reference vertical line was computed at each cross-section. To assess the variability due to sway, standard deviations in D at each cross-section were calculated for each volunteer from the eight scans obtained per volunteer. The widths W, and lengths L, of each of the eight cross-sections obtained per volunteer were calculated. The variability due to breathing was assessed by computing the standard deviations in the values of W and L at each cross-section from the eight scans obtained per volunteer.

A2.3 RESULTS

Table A2.1 shows the analysis of the comments made by the six volunteers. It can be seen that most volunteers thought that holding two side supports (posture 2) was the best posture. All the volunteers thought that standing with their hands on their shoulders was the worst posture. One volunteer complained of a loss of balance during the rotation of the positioning frame while in postures 1 and 4 (free-standing and standing with hands on shoulders). Most of the volunteers were most comfortable with a rotational speed of about 10 seconds per revolution. All the volunteers thought that a rotational speed of about 8 seconds per revolution was too fast. Table A2.2 shows the average value of the standard deviations and root-mean-

Table A2.1: Summary of comments made by volunteers

Criteria	Best Posture[+]	Next Best Posture[+]	Best Speed	Next Best Speed
Volunteer 1	Posture 2	Posture 1	10 s/rev	12 s/rev
Volunteer 2	Posture 2	Posture 3	10 s/rev	12 s/rev
Volunteer 3	Posture 2	Posture 3	12 s/rev	10 s/rev
Volunteer 4	Posture 3	Posture 2	10 s/rev	12 s/rev
Volunteer 5	Posture 3	Posture 2	10 rev/s	12 s/rev

[+]Posture 1: Free Standing; Posture 2: Holding Side Supports; Posture 3: Holding Front Supports; Posture 4: Touching both hands on shoulders

Table A2.2: Average values of standard deviations and root-mean-square errors of the width of each section for each posture

	Posture 1[+]	Posture 2[+]	Posture 3[+]	Posture 4[+]
Standard Deviation	3.2	2.2	2.4	2.9
Root-mean-square error	3.6	2.3	2.6	3.3

[+]See Table A2.1

square errors in the widths of each cross-section for each posture normalized for each volunteer. Table A2.3 shows the standard deviations in the values of D obtained at cross-sections 1 to 20 for the volunteers (denoted by I, II, III, IV and V), while Tables A2.4 and A2.5 show the standard deviations in the values of L and W, respectively obtained for each volunteer. Table 3 gives an indication of the variability due to sway while Tables 4 and 5 give an indication of the variability due to breathing. The tables show that the variability in D is less than 4.5 mm for each section, for all the volunteers. The variability in L and W are less than 2.7 and 3.2 mm respectively at each cross section.

Table A2.6 shows the average values of the standard deviations in the values of D, L and W (shown in tables A2.3, A2.4 and A2.5) for the five volunteers.

A2.4 DISCUSSION

Results show that the maximum variability in sway or breathing was less than 4.5

Table A2.3: Standard deviations (in mm) in D for each cross-section for volunteers I-V

	Volunteer				
	I	II	III	IV	V
Section 1	1.2	1.4	1.3	1.5	1.0
Section 2	1.3	1.5	1.4	1.7	1.1
Section 3	1.4	1.5	1.5	1.8	1.1
Section 4	1.3	1.8	1.6	1.9	1.1
Section 5	1.2	2.0	1.6	1.9	1.0
Section 6	1.9	2.3	1.8	2.2	1.6
Section 7	2.6	2.5	2.0	2.4	2.1
Section 8	2.5	2.4	2.2	2.6	2.0
Section 9	2.4	2.3	2.4	2.8	1.9
Section 10	2.5	2.5	2.5	3.0	2.1
Section 11	2.5	2.6	2.6	3.2	2.2
Section 12	2.6	2.5	2.5	3.0	2.1
Section 13	2.6	2.3	2.4	2.8	1.9
Section 14	3.1	2.8	2.9	3.5	2.2
Section 15	3.6	3.3	3.4	4.1	2.4
Section 16	3.0	3.3	3.3	4.0	2.2
Section 17	2.4	3.3	3.2	3.8	1.9
Section 18	3.2	3.4	3.5	4.2	2.3
Section 19	3.9	3.5	3.7	4.5	2.6
Section 20	3.2	3.4	3.3	4.5	2.0

mm at each cross section for all the volunteers. From Table A2.6, it can be seen that the average variability due to sway (variability in D) was higher than the average variability due to breathing (W and L) at each cross section. Table A2.3 shows that larger values of variability in sway occur at the upper sections of the torso (sections 6 – 10, corresponding to the thoracic region). This is not surprising as sway motion is anchored at the waist, and displacement due to sway increases from the waist upwards. It can also be seen that the variability due to breathing followed no obvious pattern across the sections. Furthermore, there was no clear relationship between the values of L and W at each cross-section.

Table A2.4: Standard deviations (in mm) in L for each cross-section for volunteers I-V

	Volunteer				
	I	II	III	IV	V
Section 1	2.7	2.5	2.6	3.2	1.8
Section 2	1.8	1.6	1.8	2.2	1.3
Section 3	0.8	0.6	0.9	1.1	0.7
Section 4	0.9	0.6	1.0	1.2	0.8
Section 5	1.0	0.6	1.1	1.3	0.8
Section 6	1.4	1.0	1.3	1.5	1.0
Section 7	1.7	1.4	1.4	1.7	1.1
Section 8	1.8	1.6	1.5	2.0	1.3
Section 9	1.9	1.8	1.6	2.2	1.5
Section 10	1.8	2.1	1.8	2.5	1.4
Section 11	1.7	2.3	1.9	2.7	1.3
Section 12	2.1	1.8	2.2	2.8	1.5
Section 13	2.5	1.3	2.4	2.9	1.7
Section 14	1.8	1.0	1.8	2.1	1.3
Section 15	1.0	0.6	1.1	1.3	0.8
Section 16	0.9	1.0	1.1	1.3	0.8
Section 17	0.8	1.4	1.0	1.3	0.7
Section 18	1.3	1.6	1.1	1.5	1.1
Section 19	1.8	1.8	1.2	1.7	1.5
Section 20	1.7	1.5	1.6	1.2	1.8

The variability due to posture was smallest for scans taken while volunteers held on to side supports and from qualitative comments, that was also the most comfortable posture. A speed of 10 seconds per rotation was optimal. Variability due to re-positioning (sway and breathing) was less than 4 mm at each cross-section for both volunteers. Variability due to sway ranged from 0 – 3.5 mm while that due to breathing ranged from 0 – 3 mm. These results are contrary to published results on the best posture for taking back surface scans and radiographs.

Contrary to published results of the best posture for taking radiographs, the results obtained from this study showed that for obtaining a full torso image of male

Table A2.5: Standard deviations (in mm) in W for each cross-section for volunteers I-V

	Volunteer				
	I	II	III	IV	V
Section 1	0.6	1.0	0.8	1.0	1.2
Section 2	1.0	1.2	0.9	1.1	1.4
Section 3	1.3	1.3	1.0	1.2	1.5
Section 4	1.3	1.3	1.1	1.3	1.3
Section 5	1.2	1.2	1.2	1.4	1.0
Section 6	1.3	1.3	1.3	1.5	1.1
Section 7	1.4	1.3	1.3	1.6	1.1
Section 8	1.8	1.5	1.5	1.8	1.1
Section 9	2.2	1.7	1.6	1.9	1.0
Section 10	2.1	1.8	1.8	2.1	1.2
Section 11	2.0	1.8	1.9	2.3	1.3
Section 12	1.3	1.3	1.3	1.6	0.9
Section 13	0.6	0.7	0.7	0.8	0.5
Section 14	0.7	0.8	0.8	0.9	0.6
Section 15	0.7	0.8	0.8	0.9	0.6
Section 16	0.9	1.0	1.1	1.0	0.9
Section 17	1.0	1.1	1.3	1.0	1.2
Section 18	0.9	1.0	2.1	1.0	0.9
Section 19	0.7	0.8	2.8	0.9	0.6
Section 20	0.6	0.9	1.0	1.1	1.1

volunteers who have no scoliosis using a rotating positioning frame, holding side supports (posture 2) produced the least variability in stance and the best reconstruction accuracy. The results also show that images taken while the volunteers stood and touched their shoulders (posture 4) were least occluded by their arms, but were most affected by motion artefacts. Analysis of comments made by the volunteers showed that standing and holding side supports (posture 2) was the most comfortable posture. The system required four shots taken at 900 intervals within 8 to 12 seconds for optimum results. Analysis of the comments made by the volunteers showed that 10 seconds was the optimum time for taking the shots. As

Table A2.6: Average values of the standard deviations in D, L and W for each cross-section

	D	L	W
Section 1	1.3	0.9	2.5
Section 2	1.4	1.1	1.7
Section 3	1.5	1.2	0.8
Section 4	1.5	1.2	0.9
Section 5	1.5	1.2	0.9
Section 6	1.9	1.3	1.2
Section 7	2.3	1.3	1.5
Section 8	2.4	1.5	1.7
Section 9	2.4	1.7	1.8
Section 10	2.6	1.8	1.9
Section 11	2.7	1.8	2
Section 12	2.6	1.2	2.1
Section 13	2.4	0.6	2.2
Section 14	2.9	0.7	1.6
Section 15	3.4	0.7	0.9
Section 16	3.2	1.4	1.0
Section 17	2.9	2	1
Section 18	3.3	1.4	1.3
Section 19	3.6	0.7	1.6
Section 20	3.6	0.8	1.5

major torso features that are indicative of scoliosis are larger than 4 mm in diameter, the system assessed could be used to obtain complete torso images for clinically assessing and managing scoliosis. These results will be useful in the design of future complete torso imaging systems for assessing torso deformities such as scoliosis.

REFERENCES

1. V. J. Raso, E. Lou, D. L. Hill, J. K. Mahood, M. J. Moreau, and N. G. Durdle, "Trunk distortion in adolescent idiopathic scoliosis", *Journal Pediatr Orthoped*, vol. 18, no. 3, pp 222-226, 1998.

2. J.R. Cobb, "Outline for the study of scoliosis, instructional course lectures,"' *The American Academy of Orthopedic Surgeons*, vol. 5, pp. 261-275, 1948.
3. Dickson RA: Spinal Deformity - Adolescent Idiopathic Scoliosis: Nonoperative Treatment, Spine, vol. 24, no. 24, pp 2601-2606, 1999.
4. P. O. Ajemba, N. G. Durdle, D. L. Hill, and V. J. Raso, "A torso imaging system for quantifying the deformity associated with scoliosis," *Proc of 2005 IEEE Instrumentation and Measurement Technology Conference*, Ottawa, Ontario, Canada, May 15-17, 2005.
5. T. Thulborne, and R. Gillespie, "The Rib Hump in Idiopathic Scoliosis: Measurement analysis and response to treatment," *J Bone and Joint Surgery,* vol. 58B, pp 456-462, 1976.
6. S. Willner, "Spinal Pantograph - A Non-invasive Technique for Describing Kyphosis and Lordosis in the thoraco-lumbar Spine," *Acta Orthop Scand,* vol. 52, pp 525-529, 1981.
7. M. S. Moreland MS, M. H. Pope, D. G. Wilder, I. A. Stokes, and J. W. Frymoyer, "Moire fringe topography of the human body," *Medical Instrumentation*, vol. 15, pp 129-132, 1981.
8. I. Weisz, R. J. Jefferson, A. R. Turner-Smith, G. R. Houghton, J. D. Harris, "ISIS scanning: a useful assessment technique in the management of scoliosis," *Spine*, vol. 13, pp 405-408.
9. P. O. Ajemba, N. G. Durdle, D. L. Hill, and V. J. Raso, "Re-positioning Effects of a Full Torso Imaging System for the Assessment of Scoliosis," *Proceedings of the 2004 IEEE Canadian Conference on Electrical and Computer Engineering,* Niagra Falls, Ontario, Canada, May 2-5, 2004.
10. P. O. Ajemba, N. G. Durdle, D. L. Hill, and V. J. Raso, "Effect of Posture on a Full Torso Imaging System for the Assessment of Scoliosis." *2004 Symposium of the International Research Society on Spinal Deformities, IRSSD,* Vancouver, Canada, June 12-14, 2004.
11. F. P E. Beer and R. Johnston, *Moments of Areas. Mechanics of Materials*, London, McGraw-Hill, pp 690-699

APPENDIX 3

ADDITIONAL BACKGROUND MATERIALS

This appendix provides additional background materials on the Bezier curve approximation theory, the moving least squares approximation theory and the moving least squares projection theory.

A3.1 BEZIER CURVE APPROXIMATION THEORY

The classical BC is a recursive linear weighted subdivision of the edges of a generated curve based on a set of points that form its control polygon for a particular weight t. A set of $N+1$ control points determine the shape of a BC of degree N. For an ordered set of points $P=\{p_0,p_1,...,p_N\}$, the matrix form of the classical BC is

$$p(t)=Pow^N(t)*Bez^N*P^T,$$

where $p(t)$ is the BC point for a particular t, $Pow^N(t)$ represents the power basis $(1,t,t^2,...,t^N)$ and the ij^{th} term of matrix Bez^N is found from $m_{ij}=(-1)^{j-i}\binom{N}{i}\binom{i}{j}$. t is the parametric operator which defines the location of the curve points, the number of which depends on the number of t values [1]. Thus, from the ordered set of points P, let the rectangular coordinates of p_i be (p_{ix},p_{iy},p_{iz}) where $i=0,1,....,N$. Then the parametric equation of the BC is given by

$$p(t)=\sum_{i=0}^{N}\binom{N}{i}(1-t)^{N-i}t^i p_i,\ \ 0\le t\le 1, \qquad (1)$$

where $p(t) = (x(t), y(t), z(t))$ [1]. The number and location of the generated points in (A4.1) completely depend on the values of t. As t ranges from 0 to 1, the procedure might produce redundant or overlapping points or an insufficient number of points.

A3.2 MOVING LEAST SQUARES APPROXIMATION THEORY

The MLS approximation theory was proposed by Lancaster and Salkauskas [2] and has been used for smoothing and interpolating scattered data in $\Re^d$ [3], [4]. Its simplest form coincides with Shepard's interpolation method [5], thus it can be seen as its extension. The MLS approximation scheme is as follows. Suppose a compact set $\Omega \subseteq \Re^d$ is given and a continuous function $f \in C(\Omega)$ is to be reconstructed from values $f(x_1),...,f(x_N)$ on scattered pair-wise distinct centres $X = \{x_1,...,x_N\}$. For $x \in \Omega$ the approximate value of $f(x)$, $p^*(x)$ is given by

$$f(x) = \min\left\{\sum_{i=1}^{N}(f(x_i) - p(x_i))^2 w(x, x_i) : p \in \mathrm{P}\right\}. \qquad (2)$$

In (A4.2), $i = 0,1,....,N$, $\mathrm{P} \subseteq C(\Omega)$ is a finite dimensional subspace spanned by polynomials, and $w : \Omega \times \Omega \rightarrow [0,\infty]$ is a continuous function with a possible singularity at the diagonal $w(x,x)$. This singularity would force the resulting function to interpolate f at the centres $x_j : j = 0,1,....,N$.

A3.3 MOVING LEAST SQUARES PROJECTION THEORY

The MLS projection theory is based on the MLS approximation theory. It aims to make the point-based representation as concise as possible while conveying the shape, in the sense that the point set is neither noisy nor redundant [6]. This is done by locally approximating the surface with polynomials using MLS approximation and sub-sampling the points appropriately.

Let points $P=\{p_i\}$ define a smooth *MLS surface* S_P, and let a reduced set of P, $R=\{r_i\}$ define an *MLS surface* S_R, that approximates S_P. The typically smaller set R is called the *representation point set* [6]. Let points $p_i \in R^3, i \in \{1,...,N\}$, be sampled from a surface S_P. The goal is to project points $r_i \in R^3$ near S_P onto a two-dimensional surface S_R that approximates p_i. The first step involves computing a local reference plane H for r where

$$H=\{x|\langle n,x\rangle - D=0, x \in R^3\}, n \in R^3, \|n\|=1$$

minimizes the local weighted sums of square Euclidean distances of points p_i to H. Assume q is the projection of r onto H and let $q=r+tn$ for some $t \in R$, then H is found by minimizing $\sum_{i=1}^{N}\langle n, p_i - r - tn\rangle^2 \theta(\|p_i - r - tn\|)$ where θ is a smooth, radial, positive, monotonically decreasing function. The approximation of single points is dictated by the radial weight function θ which as suggested by Levin [4] is a Gaussian function such that

$$\theta(d)=e^{-\frac{d^2}{h^2}},$$

where h is a fixed parameter reflecting the anticipated spacing between neighbouring points.

The minimization function used to compute H usually has more than one local minimum. Since H should be close to r, the local minimum is chosen with the smallest t. Alexa *et al.* [6] employed a standard iterative solver to ensure that the minimization function converges to a local minimum with a small t. The initial value for n is computed by setting t in the minimization function to zero, and equating the gradient of this new quadratic function in n to zero. Thus, when $t=0$, the minimization function becomes

$$\sum_{i=1}^{N} \langle n, p_i - r \rangle^2 \theta(\|p_i - r\|)$$

and

$$\sum_{i=1}^{N} 2\langle n, p_i - r \rangle \theta(\|p_i - r\|)(p_i - r) = 0.$$

The computed initial value for n can be refined using Powell iteration [7]. In this case, n is substituted into the minimization function, and using an iterative procedure of increasing t from 0, is used to establish a local minimum after which the subsequent t is selected. The global minimum of the minimization function is reached for $t \to \infty$. To avoid this, the function can be normalized using the sum of weights θ.

Next, a local bivariate polynomial approximation g, to the surface S_p, in a neighbourhood of r from the computed local reference plane H and the radial weights $\theta(\|p_i - q\|)$ is computed. Let q_i be the projection of p_i onto H, and f_i be the height of p_i over H, that is,

$$f_i = n.(p_i - q).$$

Another minimization function is constructed based on MLS approximation theory to compute the coefficients of g thereby minimizing the weighted least squares error $\sum_{i=1}^{N} (g(x_i, y_i) - f_i)^2 \theta(\|p_i - q\|)$ where (x_i, y_i) is a representation of q_i in the local coordinate system in H.

Finally, the projection of r onto S_p which is the result of the MLS projection procedure is given by the polynomial value at the origin, that is $q + g(0,0)n$. This technique yields a *smooth manifold surface* that is C^∞ smooth. A drawback is that

interpolation often fails when the *hole* is greater than three times the average spacing between points as is often the case under the arms of torso scans.

REFERENCES

1. F. A. Sohel, L. S. Dooley, G. C. Karmakar, 'A Dynamic Bezier Curve Model,' *IEEE International Conference on Image Processing (ICIP)*, 2, pp 474-477, 11-14 September, 2005.
2. P. Lancaster , and K. Salkauskas, 'Surfaces generated by moving least squares methods,' *Math. Comput.*, 37, pp 141-159, 1981.
3. H. Wendland, 'Local polynomial reproduction and moving least squares approximation,' *IMA Journal of Numerical Analysis*, 21, pp 285-300, 2001.
4. D. Levin, 'The Approximation Power of Moving Least Squares,' *Mathematics of Computation*, vol. 67, no. 224, pp. 1517-1531, October 1998.
5. D. Shepard, 'A two-dimensional interpolation function for irregularly spaced points,' *Proceedings of the A.C.M. National Conference*, pp 316-325, 1968.
6. M. Alexa, J. Behr, D. Cohen-Or, S. Fleishman, D. Levin, C. T. Silva, 'Computing and Rendering Point Set Surfaces,' *IEEE Transactions on Visualization and Computer Graphics*, 9(1), pp 3-15, January-March, 2003.
7. M. J. D. Powell, 'Restart procedures for the conjugate gradient method,' *Mathematical Programming (Historical Archive)*, 12(1), pp 241-254, December, 1977.